OUKA
The University of Osaka
Institutional Knowledge Archive

Title	Ion acceleration by laser-driven collisionless shock in multi-ion species plasma
Author(s)	Kumar, Rajesh
Citation	大阪大学, 2019, 博士論文
Version Type	VoR
URL	https://doi.org/10.18910/73512
rights	
Note	

The University of Osaka Institutional Knowledge Archive : OUKA

https://ir.library.osaka-u.ac.jp/

The University of Osaka

Osaka University

Doctoral Thesis

Ion acceleration by laser-driven collisionless shock in multi-ion species plasma

Author:
Rajesh Kumar

Supervisor:
Youich Sakawa

A thesis submitted in fulfillment of the requirements for the degree of Doctor of Philosophy

in the

International Physics Course (IPC)
Graduate School of Science

August 29, 2019

OSAKA UNIVERSITY

Abstract

Faculty Name
Graduate School of Science

Doctor of Philosophy

Ion acceleration by laser-driven collisionless shock in multi-ion species plasma

by Rajesh KUMAR

The collisionless shocks are very common in the numerous astrophysical environments such as in supernova remnants, pulsar wind nebulae, etc. These shocks are considered to be responsible for the production of high-energy cosmic rays and acceleration of particles. The astonishing growth in the development of high-power and high-intensity lasers has made it feasible to recreate the relevant conditions to examine the formation and evolution of collisionless shocks in the laboratory. The numerical and experimental findings reveal that the laser-driven electrostatic collisionless shock can be utilized as a high-energy compact particle accelerator. These accelerated particles have several desirable applications such as accelerator physics, proton radiography, and cancer therapy, etc.

In this thesis, we report on the numerical investigation of electrostatic collisionless shock formation and influence of different materials on the shock accelerated ion beams. The different target materials used are the hydrogen, carbon, oxygen, and chlorine to give a range of average charge (<Z>) to mass (<A>) ratio, i.e., <Z/A> = 0.48 - 1.

The 2D EPOCH particle-in-cell simulations are employed to investigate the laser-driven electrostatic collisionless shock ion acceleration in different materials. The density profile and laser parameters are the same for all materials. Our result indicates that the electrostatic collisionless shock is excited, and protons are reflected and accelerated by the shock-associated electrostatic field. The laser to shock-accelerated protons conversion efficiency and the number of these protons are significantly increased in the multi-ion species plasmas, such as CH and C_2H_3Cl plasmas compared to a pure H plasma.

In the upstream region of the shock, ions expand with different velocities depending on their <Z/A> under the non-oscillating component of the sheath electrostatic field. In multi-ion species plasmas, the excitation of electrostatic ion two-stream instability (EITI) between the heavier and lighter ion populations occurs. This results in the deceleration of the expanding protons and appearance of a low-velocity component. An additional EITI between the reflected and expanding protons accelerates some of the expanding protons to the higher velocity, which results in more protons being accelerated by the shock. The analytic and exact solutions for the dispersion relation of EITI indicate that the unstable modes of the instability appear in multi-ion species plasmas.

It is shown that the interaction of high intensity ($a_0 \geq 10$) laser with multi-ion species plasma leads to the formation of two shock fronts in fully ionized carbon and proton, respectively. The shock front propagates slower in C-ions compared to protons. Therefore, both C-ions and protons are accelerated by different shocks via CSA mechanism. The shock velocity and Mach number of C-ions and protons can be scaled as the power-law dependence on a_0. In case of C-ions, the Mach number is a stronger function of a_0 compared to that of protons in the multi-ion species plasma with the lowest <Z/A>, i.e., C_2H_3Cl. The flux of shock accelerated protons and C-ions is more significant in multi-ion species plasma compared to the pure H and C plasmas.

The CSA experiment is carried out by using a combination of GEKKO-XII (pre-ionization beam) and LFEX (shock-driving beam) laser facilities at the Institute of Laser Engineering, Osaka University (Japan). The rear-surface of 0.7 μm CH foil is irradiated by a pre-ionization laser beam to produce a suitable density profile for CSA. After the target expansion, a shock-driving beam is irradiated from the front side of the target to drive a collisionless shock wave. The necessary density profile is optimized by varying the time delay, Δt = 0 - 1.5 ns within the two laser beams. The passive ion diagnostics, i.e., RCF stacks and CR39 detector plates confirm that the maximum energy of the accelerated protons is in the range of 7.03 MeV - 9.03 MeV for Δt = 1.2 ns.

Acknowledgements

At this moment, I would like to take the opportunity to thank all my collaborators and all my friends that supported me during my Ph.D. time and help me to complete this thesis successfully.

First of all, I would like to thank my supervisor Associate Prof. **Youichi Sakawa** for giving me the opportunity to be part of his group and guiding me into this exciting field of collisionless shock and laser-driven ion acceleration. I am indebted to him for countless hours of fruitful discussions and ideas. He always puts his things aside to help me out whenever I pester him with some new problem of mine. I also want to thank him for his encouragement and patience on me, giving me as much freedom as I wanted, and always supporting me in every possible way. He has been not only a great supervisor but also a great friend.

I would especially like to thank Assistant Prof. **Alessio Morace**, who showed me how to make proper simulations. Also, I learned from his example of how important it is to not only correctly set some simulation parameters but also to have a broad physical knowledge.

I owe my deepest gratitude to Ph.D. committee members Prof. **Shinsuke Fujioka**, Prof. **Mitsuo Nakai**, and Prof. **Tadashi Kondo** who give their precious time in reading this thesis and suggesting essential points.

I convey special acknowledgment to our collaborators **Leonard N. K. Dohl** for giving me advice especially the first times I made particle simulations and Prof. **Nigel Woolsey** *(York University, UK)* for giving his valuable time to read my manuscripts and giving me very useful comments.

Least but not last I would like to thank my family and friends. I should start with my mother, late Krishna Devi, in the first place is the person who showed high confidence in me and encouraged me to come away from home and pursue my Ph.D. work. Special thanks to my elder brother Rakesh Dhiman, who always supported me financially throughout my studies. The rest of the family members who I will not list here, your positive reinforcements were always appreciated. As for my friends, I apologize for any omissions, but I would like to thank Dr. Prashant Goyal, Brijesh Sharma, Ravi Yadav, and Leonard N. K. Dohl among many others, for their continuous support and friendship. Thank you all very much, it has been a privilege...

Contents

Abstract **1**

1 Introduction **11**
1.1 Motivation . . . 11
1.2 Introduction . . . 12
1.3 Laser-Based Particle Accelerators . . . 13
1.4 Applications . . . 14
1.4.1 Radiography . . . 14
1.4.2 Radiation Therapy . . . 15
1.4.3 Isotope Generation . . . 16
1.4.4 Fast Ignition . . . 16
1.5 Thesis Outline . . . 17

2 Theoretical Background **19**
2.1 Plasma . . . 19
2.1.1 Debye Length . . . 19
2.1.2 Plasma Frequency . . . 21
2.1.3 The Dispersion Relation . . . 22
2.2 Basics of laser field . . . 23
2.2.1 Relativistic Laser Intensity . . . 24
2.3 Relativistic Transparency . . . 25
2.4 Laser Absorption Mechanism . . . 26
2.4.1 Resonance Absorption . . . 26
2.4.2 Vacuum Heating . . . 26
2.4.3 J×B Heating . . . 27

3 Particle-in-cell Technique **29**
3.1 Introduction . . . 29
3.2 Particle-in-cell Approach . . . 30
3.2.1 Field Advancing . . . 30
3.2.2 Particle Velocity Progression . . . 32
3.2.3 Finite Difference Method Stability . . . 33
3.3 EPOCH Framework . . . 34

4 Laser-Driven Ion Acceleration **35**
4.1 Introduction . . . 35
4.2 Target Normal Sheath Acceleration (TNSA) . . . 36
4.2.1 Theoretical Model for TNSA . . . 37
4.2.2 Quasi-static Model . . . 39
4.3 Radiation-Pressure Acceleration . . . 40

4.3.1 Hole-Boring RPA: Thick Target . . . 41
4.3.2 Light-sail RPA: Thin Targets . . . 44
4.4 Collisionless Shock Ion Acceleration . . . 45

5 Theory of Collisionless Shock Ion Acceleration 49
5.1 Collisionless Shock . . . 49
5.1.1 Conservation Laws . . . 49
5.2 Ion Acoustic Wave in Plasma . . . 52
5.3 Ion Acoustic Solitons . . . 54
5.4 Particle Reflection . . . 57

6 Material Dependence of CSA 61
6.1 Introduction . . . 61
6.2 Simulations Parameters . . . 61
6.3 Electrostatic Collisionless Shock Formation . . . 63
6.3.1 Electron temperature and Shock Velocity . . . 66
6.3.2 TNSA Electrostatic Field Scaling . . . 70
6.3.3 Proton Acceleration via CSA . . . 72
6.4 Summary . . . 79

7 Electrostatic Ion Two-stream Instability 81
7.1 Introduction . . . 81
7.1.1 EITI in C_2H_3Cl Plasma . . . 83
7.1.2 Velocity Distribution of Expanding Ions . . . 83
7.2 EITI in multi-ion species plasma . . . 88
7.2.1 Analytical Solution . . . 88
7.2.2 Exact Solution . . . 91
7.3 Summary . . . 95

8 Heavy-Ion Acceleration 97
8.1 Introduction . . . 97
8.2 Simulation Result for $a_0 = 10$ . . . 99
8.3 Effect of Laser Intensity on CSA . . . 101
8.4 Summary . . . 106

9 CSA LFEX-GXII Experiment 107
9.1 Introduction . . . 107
9.2 Experimental Setup . . . 107
9.3 Experimental Results . . . 108
9.4 Simulation Results . . . 111
9.5 Summary . . . 114

10 Summary & Future Work 115
10.1 Summary . . . 115
10.2 Future Work . . . 116

Bibliography 119

List of Figures

1.1 Comparison of dose depth for different type of radiation treatment 15

2.1 Schematic demonstration of collisionless absorption mechanism. 27

3.1 Schematic of a typical timsetup for particle-in-cell code. 30

4.1 Schematic of ion acceleration in laser-solid interaction (TNSA). 37
4.2 Graphical illustration of ion density, n_i, electron density, n_e, and electrostatic field, E_x (RPA). 42

5.1 Schematic description of a soliton wave 54
5.2 Sagdeev potential as function of electrostatic potential 56
5.3 An oscillatory electrostatic collisionless shock transition 58

6.1 The laser and electron density profile used in PIC simulations . 62
6.2 The temporal evolution of N_H/N_{cr} in C_2H_3Cl plasma 64
6.3 The spatial profile of electrostatic potentials in (a) C_2H_3Cl and (b) Hydrogen plasma 65
6.4 The electron phase-space and temporal evolution of T_e in C_2H_3Cl plasma 67
6.5 The temporal evolution of shock positions and shock velocity in H and C_2H_3Cl plasmas 69
6.6 The temporal evolution V_{Cl} and E_{TNSA} field in C_2H_3Cl plasma . 71
6.7 Time evolution of proton phase-space and velocity spectrum in C_2H_3Cl 73
6.8 The proton phase-space and velocity spectrum in different materials plasma 74
6.9 The dN/dV_{ref} at $t = 4.0$ ps and dN/dV_{exp} at t_1 and t_2 taken at $\Delta x = 3$ μm in the upstream region. 75
6.10 <Z/A> dependence of $(dN/dE)E_0$, and the laser to reflected protons conversion efficiency (CE), ... 76
6.11 The variation of V_{sh}/c, V_L/c, and $V'_{df}/c = (V_{sh} - V_L)/c$ as function of dN/dV_x 78

7.1 2D electrostatic field (E_x) distribution averaged over two laser-cycles in the upstream region of C_2H_3Cl plasma 84
7.2 Velocity spectrum of the expanding ions taken at $\Delta x = 3$ μm in the upstream region of C_2H_3Cl 85
7.3 The time evolution of (a) peak number density, (b) velocities, and (c) ion temperature of the 1st (L), 2nd (M), and 3rd (H) fitted 1D shifted Maxwellian in C_2H_3Cl plasma at $t = 4.0$ ps. . 86

7.4 Time evolution of the expanding ion velocities in C_2H_3Cl 87
7.5 Derived power spectrum of electrostatic field, E_x at t = 4.0 ps taken in the region 89
7.6 Velocity spectrum of the expanding ions in CD and CCl_2 targets 90
7.7 Electrostatic ion two-stream instability by assuming $1/k_x\lambda_{De} = 0$ in C_2H_3Cl plasma 92
7.8 Electrostatic ion two-stream instability by assuming $1/k_x\lambda_{De} \neq 0$ in C_2H_3Cl plasma 93
7.9 The temporal evolution of wave number (k_x) growth rate (ω_i) for HI- and RP-EITI 94

8.1 Phase-space of C-ions at $t = 4.0$ ps in C_2H_3Cl and CH plasmas 98
8.2 The normalized electron density at $t = 3.0$ ps and $t = 4.0$ ps in C_2H_3Cl plasma for $a_0 = 10$ 100
8.3 The ion phase-space, the velocity spectrum in pure H, C_2H_3Cl, and pure C plasmas 101
8.4 The electron energy distribution for $a_0 = 3.35$ (×), 10 (+), 20 (|), and 33 (|) 102
8.5 a_0 dependence of V^i_{sh}, V^i_m, C^i_s, V_{df}, and Mach number 103
8.6 The temporal evolution of shock position and velocity for protons and C-ions in C_2H_3Cl plasma for $a_0 = 33$. 104
8.7 a_0 dependence of energy (E) and the number (dN/dE at E) of reflected protons for pure H and C plasmas, and protons and C-ions in C_2H_3Cl. 105

9.1 A schematic of the experimental setup (top view) 108
9.2 A sequence of the RCF films and CR39 plates exposed to the accelerated ions 109
9.3 The time delay, Δt dependance of accelerated proton energy and electron temperature 110
9.4 Time evolution of proton density profile. A proton phase space and electron temperature at t = 4.0 ps 112
9.5 The PIC results of the accelerated proton energy and electron temperature as a function of initial normalized electron density . 113

List of Tables

6.1 The different target materials used in PIC simulations. 63

Chapter 1

Introduction

1.1 Motivation

The collisionless shocks are very common in the various astrophysical environments such as in supernova remnants, pulsar wind nebulae, etc. These shocks are thought to be responsible for the generation of high-energy cosmic rays and acceleration of particles. Astonishing improvement in the development of high-power and high-intensity lasers has made it possible to recreate the relevant conditions to study the formation and evolution of collisionless shocks in the laboratory.

The interaction of high-intensity laser with plasma leads to the excitation of strong electric and magnetic fields in the plasmas, which accelerates the ions to high energy over short distances. The generation of a high-quality ion beam in the laser-plasma interaction could provide an alternative source for the conventional accelerator. In comparison with the conventional accelerator, the laser-driven accelerator offers a significant improvement in cost, compact size, affordability, and high repetition. However, despite all these advantages, several difficulties need to be addressed, such as particle energy, ion flux, laser-to-accelerated ion conversion efficiency, and energy-spread, etc. This has motivated a significant numerical and experimental effort devoted to understanding and optimizing physics behind the process of ion acceleration. Several mechanisms have been proposed in last decade to improve the quality of the laser-driven ion beams, such as target normal sheath acceleration (TNSA), radiation pressure Acceleration (RPA) and collisionless shock ion acceleration (CSA), etc. Among all these mechanisms, CSA has become an attractive candidate for high-quality ion beams. In contrast to the TNSA mechanism, CSA produces a high-energy ion beams with low energy spread. Unlike RPA, CSA does not impose any strict requirements on the laser contrast ratio and target thickness. Thus, ion beams with high-energy, high-flux, and low energy-spread can be produced via CSA mechanism. Several experiments have been carried out over the last few years to understand and characterize ion acceleration via CSA. One aspect of CSA that is currently not well understood for accelerating mono-energetic ions to high energies is the effect of the target material used. In this thesis, we used the EPOCH particle-in-cell (PIC) to study the generation of collisionless shocks and proton acceleration from shocks formed in plasmas of different material composition.

1.2 Introduction

Back in the 1960s, the invention of the first functioning laser by Maiman [1] confirmed to be one of the most significant sources to understand the behaviour of matter in the presence of an extreme external applied field. In the 1970s, the research on laser-plasma interaction has started, and it was principally directed on the laser-induced inertial confinement fusion [2]. The invention of pulse amplification of laser opened numerous exciting research possibilities in the field of the laser-plasma interaction. In the late 1970s, the continuous wave system has been overcome with novel techniques, such as Q-switching [3] and mode-locking [4, 5], which enhances the laser intensities up to $\sim 10^{15}$ Wcm^{-2}. This could provide to store the peak laser energy in the nanosecond or picosecond duration pulses.

The invention of chirped pulse amplification technique (CPA) in 1985 by Strickland and Mourou [6, 7], have led to a fundamental breakthrough in the field of solid-state laser sources. In the CPA technique, the laser pulse can be stretched temporally and spatially before being amplified and after which it re-compressed to a very short pulse of a few tens of femtosecond (fs). This pioneers to the development of terawatt to petawatt-class laser systems, which initiates a new era in the field of relativistic laser-plasma interaction [7, 8] with an extreme intensity of $\sim 10^{23}$ Wcm^{-2} in future [9]. The field strength at these laser intensities is the order of teravolt/cm (TVcm^{-1}) [10], which is much more significant than the field that binds the electrons to the nucleus. Here, the 'relativistic' refers to the fact that electrons can be accelerated close to the speed of light, c within the half of the laser cycle. This is corresponding to the laser intensity threshold of 1.37×10^{18} Wcm^{-2} for 1 μm laser wavelength. The interaction of such a high laser intensity with matter results in the complete ionization of medium during the first laser cycle. It results in relativistic and non-linear plasma interaction with the rest of the laser pulse. Several non-linear, unconventional phenomenons have been experimentally witnessed as a consequence of interaction processes, such as high-order harmonics [11, 12], electron, and ion acceleration, X-ray and particle sources, thermonuclear inertial confinement fusion, and ultrafast optical devices, etc. Among all these phenomenons particle acceleration (electrons and ions) and the generation of X-ray radiation have become the most exciting subject in laser-plasma interaction.

The interaction of ultrahigh-intensity laser with plasma has become available at various laboratories all around the world. There are several high-power laser facilities all around the world such as BELLA (BErkeley Lab Laser Accelerator) at the Lawrence Berkeley National Laboratory [13] and National Ignition Facility at the Lawrence Livermore National Laboratory in Livermore in the US, and Vulcan laser at the Central Laser Facility in the UK, LFEX and GEKKO-XII laser facility at the Institute of laser engineering at Osaka University, Japan etc. A wide verity of problems in laser, plasma, and nuclear physics can be analyzed by utilizing these laser facilities and also, it might be possible to examine the non-linear dynamics of QED-effects [14] in the future. These facilities have great importance for light-ion acceleration, and several other record-breaking investigations have been presented in laser-plasma interaction.

1.3 Laser-Based Particle Accelerators

In 1979, Tajima & Dawson proposed that, the interaction of laser pulse with plasma results in the acceleration of some particles within the plasma [15]. Based on this approach, a 44 MeV energetic accelerated electron beam has been demonstrated experimentally [16]. Astonishing improvement in the development of high-power and high-intensity laser has made it possible to accelerates the electrons up to > 1 GeV energies [17–23].

In the past few years, the acceleration of ions in laser-plasma interaction has attracted most of the attention. Unlike electrons, ions cannot be accelerated directly by the laser fields because of their heavy mass. The acceleration of ions primarily depends on the generation of hot-electrons in laser-plasma interaction. Based on the laser-plasma interactions, several mechanisms have been proposed to accelerate ions in the forward directions [24]. The acceleration of ions up to several 10s of MeV has already been achieved experimentally by the interaction of high-intensity laser with different targets [25–29]. Because of their low quality and higher divergence, these accelerated ion beams were not useful for applications. Consequently, further experimental investigations for laser-based ion accelerators reveals the production of good quality multi-MeV proton beams in laser-solid interaction [30–34]. The generation of high-quality multi-MeV proton beams in the forward direction has triggered the interest in the laser-based ion acceleration applications. Soon the questions start rising what mechanism is responsible for the generation multi-MeV proton beams and where these protons are accelerated exactly? In 2001, Wilks et al. [33] developed a theoretical model to support the experimental outcomes [30–32] for protons acceleration mechanism, which he described as **T**arget **N**ormal **S**heath **A**cceleration (TNSA) mechanism. In this mechanism, the ions are accelerated by a strong space-charge electrostatic field on the rear-side of the target. Further discussion on the TNSA mechanism will be given in Chapter 4. However, the proton beams produced via the TNSA mechanism have a broad energy spectrum with a low emittance, which is not suitable for most of the applications.

Other schemes for laser-driven ion accelerations that have been explored in previous years include the radiation pressure acceleration (RPA) [35–40] and electrostatic collisionless shock ion acceleration (CSA) [41–43]. In RPA scheme, the ions are accelerated by the laser radiation pressure. The detailed discussion for RPA will be shown in Chapter 4, where we will discuss the two cases for RPA; hole-boring RPA [36, 38] and light-sail RPA [39, 40]. On the other hand, in CSA mechanism, the interaction of laser pulse with plasma results in the uniform electron heating via J×B mechanism [44] and steepening of density profile occurs. Later on, the thermal expansion of density on the rear side of the target leads to the shock generation. To accelerates the ions via CSA mechanism, the electrostatic potential energy at the shock front must be larger than the kinetic energy of incoming ions [41]. A detailed theoretical background for shock formation and ion acceleration will be provided in Chapter 5. In the last few years, several numerical [42, 43, 45–48] and experimental [49–54] investigation have been carried out on CSA. In this thesis, we will discuss the numerical particle-in-cell simulations for the electrostatic collisionless shock ion

acceleration in different target materials by varying their average charge (<Z>) to mass (<A>) ratio, i.e., <Z/A> = 0.48-1.

1.4 Applications

The generation of high-quality ion beams in the laser-plasma interaction could provide an alternate source for conventional accelerators [55]. In comparison to conventional accelerators, the laser-driven accelerators offer a significant improvement on compact size, affordability, a high repetition, and high proton flux per shot. Some of the current and future applications will be described in the next section.

1.4.1 Radiography

Radiography is one of the compelling application of ion beams produced by the laser-driven accelerators. Exploration of field structures in plasmas is not an easy task. The density measurement of the plasmas is done by the optical diagnostics, in which the diffraction of light rays occurs when they propagate through a change in the refractive index. Radiography utilizes the idea of probing the matter/plasma by applying the ion beams. However, the exploration of matter by using ion beam approach is not a new concept [56, 57]. Ion beams accelerated in laser-plasma interaction have essential characteristics such as high flux, low energy spread, compact size, short time for acceleration, etc. These qualities make them an excellent source to study the field structures in plasmas [58].

In the multi-laser beams experiments, the ions are produced by utilizing one of the laser beams. These ions can be used to image the field structures plasma produced by the interaction of other laser beams [59]. The ion beams delivered by the interaction of the first laser get deflected by the electromagnetic field when they propagate through the generated plasma on the front or rear surface of the second target. The imaging of these ion beams designates that the ion beams are spatially separated depending on their deflection and distance between the ion source and target. Consequently, temporal information of the probed target can be extracted by measuring the velocity of these ion beams. These ion beams have a range of energies depending on their thermal energy.

Currently, radiography is one of the major diagnostics and successfully employed in numerous experiments to probe the targets. This technique has already been adopted to measure the temporal resolution of electrostatic sheath field expansion on the rear-side of the foil target [60]. Recently, proton radiography has been employed to resolve the electrostatic collisionless shock wave [61]. Several authors have been utilizing proton radiography to observe the formation of a magnetic field structure in laser-solid interaction [62–64] while some of them are using it for the observation of the channel formation in near-critical density plasma [65].

1.4.2 Radiation Therapy

Radiotherapy is one of the most crucial applications for laser-driven ion acceleration. In 1946 Wilson [66] delivered the concept concerning the advantage of fast protons for Radiology. In radiation therapy, we aim to treat the cancer tumor by ionizing radiation on it. Typically, x-rays or gamma rays (photons) are used to destroy the cancer tumor. These photons lose their energy exponentially with the increase in the thickness, as shown in Fig. 1.1(a). Therefore a reasonable amount of damage can be expected to the neighbouring tissue, which can not be avoided. Figure 1.1(a) designates that the use of high-energy electrons is limited to a certain range of penetration depth. On the other hand, most of the energy contained in the heavy ions or proton beams is deposited in the Bragg's peak, which is nearly at the end of the range with very narrow spread around the Bragg's peak. This characteristic of heavy ions or protons beams provides the precise treatment to cancer damaged tissue with very little harm to the neighbouring tissues, which is one of the advantages of these ions beams compared to the x-rays or gamma rays [67–69]. Regardless of it, many cancer treatment facilities based on the conventional accelerators have been established which are very costly and big in size, such as Heidelberg Ion-Beam Therapy Center (HIT).

An alternative to the conventional accelerators, the laser-driven accelerators have been proposed to deliver the high-quality ion beams for radiation therapy [70–73]. As it can be seen in Fig. 1.1(b) the laser beam can be delivered directly on the target, which is located in the patient treatment room. In comparison to conventional accelerators, the laser-driven accelerators offer a significant improvement on compact size which requires small gentry, high cost-effective, a high repetition, and high proton flux per shot, etc. The whole laser-driven accelerators are enthusiastic but optimistic, such as a proton beam with energy 200 MeV, with high flux and narrow energy spread required to reach a deep-seated over a depth >25 cm (in water). However, we still need to find a solution to this problem. The understanding of the underlying physics and the development of accelerator-patient-interface are equally important.

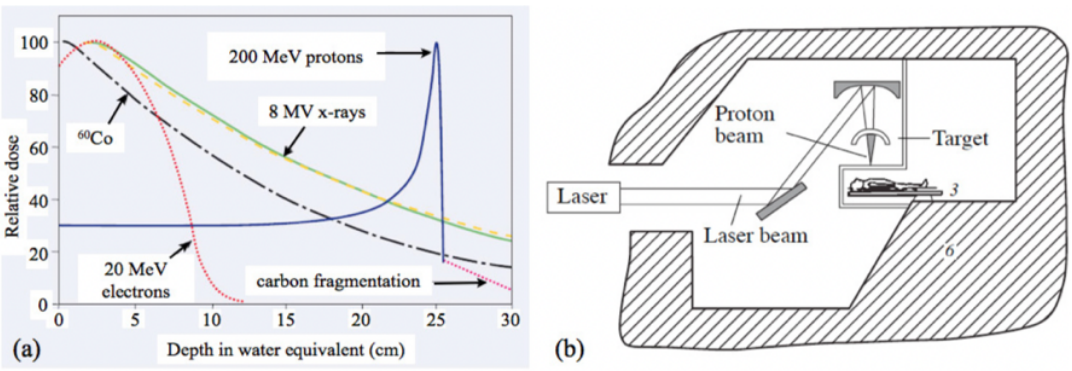


FIGURE 1.1: (a) Comparison of dose depth for different type of radiation treatment [67]. (b) Simple demonstration for laser-driven radiation therapy treatment [taken from [68]].

1.4.3 Isotope Generation

In low-Z materials, the nuclear reactions can be induced by the multi-MeV proton beams. Therefore, the positron emission tomography (PET) can be implemented by producing a short-lived positron by applying the laser-based ion accelerators. PET technology is very beneficial for medical imaging concerning cancer tumor tissue detection, blood flow, and amino acid transport, etc. Until now, large size and very costly cyclotron has been used to produce a 20 MeV proton beams for PET imaging technology. Consequently, in future proton beams provided by the tabletop laser systems can be utilized for the production of short-lived isotopes. A laser system with an energy 1 J, intensity, 10^{20} Wcm^{-2}, and pulse duration of 30 fs is required to reach the necessary activity 1 GBq for PET [74, 75].

1.4.4 Fast Ignition

One of the primary applications for laser-driven ion beam is the fusion. The fusion always aims to deliver the energies in a more cleaner way than nuclear power plants and coal. Currently, there are two primary schemes which are examined most, magnetic confinement fusion (MCF) [76, 77] and inertial confinement fusion (ICF) [78]. In both schemes, deuterium, and tritium fuel is required to be heated to a temperature ∼10 keV for some time to produce the efficient for high rate fusion.

In MCF, also known as Tokamak, a large toroidal magnetic field is applied for a few seconds to heat the low density ($\sim 10^{15}$ cm^{-3}) plasma. Currently, the **I**nternational **T**hermonuclear **E**xperimental **R**eactor (ITER) [79], is the largest and most advanced Tokamak for MCF [80–82].

In ICF [83, 84], also identified as the direct drive, where the multiple laser beams are focused on the surface of spherical pellet to compress it to a high density ($\geq 10^{25}$ cm^{-3}) and heat it to high temperature ($\sim$ 10 keV). Most of the investigations focused on the deuterium-tritium (DT) fusion because of the high fusion cross-section, with a plasma temperature of 10 keV that can be obtained in the laboratory. This temperature leads to the fusion by surpassing the coulomb barrier. A 17.6 MeV energy (alpha particle + neutron) is released in DT fusion reaction [85]

$$\mathrm{D}_1^2 + \mathrm{T}_1^3 \longrightarrow \mathrm{He}_2^4(3.5\mathrm{MeV}) + \mathrm{n}_0^1(14.1\mathrm{MeV}). \tag{1.1}$$

Although an explosion with a high degree of symmetry is needed to achieve the energy and reach the ignition. Also, the succession of the experiment is compromised by several plasma instabilities.

To overcome these difficulties, another approach has been proposed, which is identified as the fast ignition — this scheme is composed of two stages. In the first stage, the target is compressed via momentum conservation by irradiating the target with several laser beams. On the second, the burning and compression phase is separated by the fast ignition. After the fuel compression, a high-intensity laser beam is applied to generate the population of hot electrons. These

electrons heat up and ignite the fuel via collision at the core [86]. Although this approach also has some limitations which are required to be solved in the future.

An oil barrel ($\sim$ 150 kg) can produce an amount of energy equivalent to 6.1 GJ. Thus a rough estimate can be made to provide the same amount of energy by using DT fuel. This shows 18 mg of DT fuel is required to produce the equivalent energy. As seawater is the primary source for deuterium, both the deuterium and tritium are easily obtainable. By using low-Z material as the wall of the reactors, this process does not produce any harmful, long-lived radioactive waste.

1.5 Thesis Outline

In this doctoral thesis, we report on the numerical investigation of electrostatic collisionless shock formation and influence of different materials on the shock-accelerated proton beams. All work described in this thesis has been carried out in the Laser Astro Experiment (LAE) group led by Associate Professor Youichi Sakawa at Institute of Laser Engineering, Osaka University (Japan). The outlines of this thesis are as follows;

Chapter:-2 This section describes the fundamental characteristics and theoretical background of the plasmas. A theoretical foundation of laser-plasma interaction and various collisionless absorption mechanisms are discussed.

Chapter:-3 This section provides a summary of a particle-in-cell numerical code. Two-dimensional EPOCH particle-in-cell open source code is used throughout this thesis to study the formation of electrostatic collisionless shock and their subsequent acceleration in different target materials.

Chapter:-4 This section provides an overview discussion on various laser-driven ion acceleration mechanisms, such as Target Normal Sheath Acceleration (TNSA), Radiation Pressure Acceleration (RPA, hole-boring RPA & light-sail RPA), and previous work on Electrostatic Collisionless Shock Ion Acceleration (CSA).

Chapter:-5 A discussion on the formation of ion-acoustic waves, solitons, shock waves, and Rankine-Hugoniot relations is provided in this section. The existence of collisionless shocks and ion-acoustic solitons is explained by utilizing Sagdeev pseudo-potential method. This section also provides a discussion on particle reflection and particle trapping in collisionless shocks.

Chapter:-6 This section presents the EPOCH 2D particle-in-cell simulation results for the generation of electrostatic collisionless shock and proton accelerations from the shock formed in the plasmas of different materials. The density profile and laser parameters are the same for all materials. It is shown that the electrostatic collisionless shock is excited, and protons are reflected and accelerated by the shock-associated electrostatic field. The laser to shock-accelerated protons conversion efficiency and the number of these protons are significantly increased in the multi-ion species plasmas, such as CH and C_2H_3Cl plasmas compared to a pure H plasma.

Chapter:-7 This section presents a detailed discussion on Electrostatic Ion Two-stream Instability (EITI) observed in EPOCH PIC simulations. In the plasmas with multi-ion species, the ions with a lower <Z/A> compared to the

protons (with <Z/A> = 1) gain different velocities under the non-oscillating component of the sheath electrostatic field, which leads to the excitation of electrostatic ion two-stream instability (EITI) between the heavier and lighter ion populations occurs. This results in the deceleration of the expanding protons and appearance of a low-velocity component. An additional EITI between the reflected and expanding protons accelerates some of the protons to the higher velocity which results in more protons being accelerated by the shock. The analytic and exact solutions for the dispersion relation of EITI indicate that the unstable modes of the instability appear in multi-ion species plasmas.

Chapter:-8 The acceleration of heavy-ions (C^{6+}) via CSA mechanism in multi-ion species plasmas is presented in this section. It is shown that the interaction of laser intensities corresponding to $a_0 \geq 10$ with multi-ion species (C_2H_3Cl) plasma leads to the formation of two shock fronts in proton and carbon densities. The shock fronts propagate slower in C-ions compared to protons. Thus both C-ions and protons are accelerated by different shocks via CSA mechanism. The shock velocity and Mach number of C-ions and protons can be scaled as the power-law dependence on a_0. In case of C-ions, the Mach number is a stronger function of a_0 compared to that of protons in the multi-ion species plasma with the lowest <Z/A>, i.e. (C_2H_3Cl). The number of shocks-accelerated protons and C-ions is more significant in multi-ion species plasma compared to the pure H and C plasmas.

Chapter:-9 This section describes the experimental demonstration of collisionless shock and their subsequent proton acceleration. The CSA experiment is carried out by using a combination of GEKKO-XII (pre-ionization beam) and LFEX (shock-driving beam) laser facilities at the Institute of Laser Engineering, Osaka University. The rear-surface of 0.7 μm CH foil is irradiated by a pre-ionization laser beam to produce a suitable density profile for CSA. After the target expansion, a shock-driving beam is irradiated from the front side of the target to derive a collisionless shock wave. The necessary density profile is optimized by varying the time delay, Δt = 0 - 1.5 ns between the two laser beams. The passive ion diagnostics, i.e., RCF stacks and CR39 detector plates confirm that the maximum energy of the accelerated protons is in the range of 7.03 MeV - 9.03 MeV for Δt = 1.2 ns.

Chapter:-10 this section summaries the simulation and experimental results presented in this thesis and gives an outlook for the future experimental investigations.

Chapter 2

Theoretical Background

2.1 Plasma

The Plasma state is often referred to as the "fourth state of matter." It is defined as the quasi-neutral gas, consisting of positive and negative charged particles which exhibit the collective electromagnetic behaviour [87]. Collective behaviour means a change in the properties of plasma in a specified region will affect the whole plasma [88]. Consider a plasma which contains a group of charged particles displaced by electromagnetic forces. Here, the electromagnetic force from a given charged particle causes all nearby particles to move, thereby electrically polarizing the medium. As a consequence, the movement of charged particles (ions or electrons) leads to a charge imbalance; consequently, a net charge difference exists between the two regions, which results in an electrostatic field. The movement of charged particles also appears in the current flow and induces a magnetic field in the plasma. Therefore, the motion of charged particles in a plasma is affected by these electric and magnetic fields, and outside of the plasma these forces are screened, this characteristic length of the plasma identified as the Debye-length. It is a measure of the distance over which the neighbouring charged particles shield the electrostatic field of a charged particle in plasma. Consequently, the collective behaviour of the plasma depends on the whole system, not only on the local plasma conditions.

In a high-intensity laser-plasma interaction, the induced ionization of the material leads to the formation of the plasma. The plasma formation is caused either by the associated electric field with the laser pulse or through the collisional mechanism on the front surface of the material. Nevertheless, in the bulk of the materials, more complicated mechanisms are involved, which we will discuss later in this chapter. In plasmas, N_e and N_i represent the electron and ion number densities, respectively, where $N_e = ZN_i$ from the plasma quasi-neutral condition. Here Z is the charge state of the ions.

2.1.1 Debye Length

To understand the physics of plasma in a more advanced manner, we will begin our study by examining the characteristic scale-length known as the Debye-length, a concept emerging from the theory of liquids and electrolytes [89]. Debye-length illustrates the response of a plasma when an external charged particle is placed in it.

Classical non-relativistic plasma is characterized as the quasi-neutral, i.e., it is necessary to have an equal number of positive and negative charges in a volume element. To satisfy the requirement of charge neutrality inside a volume element, the microscopic charge field of each particle must cancel each other.

To hold on the charge neutrality of plasma, the Coulomb-potential field of each particle with charge, e is given by

$$\Phi_{\mathrm{CP}} = \frac{1}{4\pi\epsilon_0}\frac{e}{r}. \tag{2.1}$$

Here, r is the distance between the two charged particles, $\epsilon_0 = 8.85\times\ 10^{-12}$ $m^{-3}kg^{-1}s^4A^2$ is the permittivity of free space. Other charged particles in the plasma shield the Φ_{CP}. Now let's examine the Debye-potential, which is given by

$$\Phi_{\mathrm{DP}} = \left(\frac{1}{4\pi\epsilon_0}\frac{e}{r}\right)\exp\left(-\frac{r}{\lambda_D}\right), \tag{2.2}$$

for $r > \lambda_D$, the exponential function cut off the potential. Here, λ_D is the characteristic length, known as the Debye-length over which a significant charge separation can happen. In other words, Debye-length is the measure of shielding length or thickness of sheath, outside of which charges are screened. The Debye-length is given by [87]

$$\lambda_{Dj} = \sqrt{\frac{\epsilon_0 k_B \mathrm{T}_j}{\mathrm{Z}_j^2 e^2 \mathrm{N}_j}}, \tag{2.3}$$

where k_{B} is the Boltzmann constant, T_j and N_j stands for the temperature and number density of particle j. In order to satisfy the quasi-neutrality of the plasma, the physical dimension of the system, L, must be larger than the electron Debye-length λ_{De}

$$\lambda_{De} << \mathrm{L}. \tag{2.4}$$

Otherwise, there is not sufficient space for the collective shielding effect to occur, and we have simple ionized gas — this requirement, usually known as the first plasma criterion. A sphere with radius λ_{De} is known as the Debye sphere, and the Debye number, $\Lambda = \frac{4\pi}{3}\mathrm{N}_e\lambda_{De}^3$ gives the number of electrons inside the Debye sphere. The Λ known as the plasma parameter, with

$$\Lambda >> 1, \tag{2.5}$$

represents the plasma. As a result, a large number of particles are needed to provide effective shielding.

The classification of Debye shielding considers that initially, plasma was neutral, i.e., the electron and ion number densities are equal. In the case of the plasma consisting of only singly charged ions, this signifies $\mathrm{N}_e = \mathrm{N}_i$. In the presence of multiple charged ion species, we need to modify this relation. If Z_j is the charged state and N_j is the number density of the ions, the quasi-neutrality condition is given by

$$\mathrm{N}_e \approx \sum_j \mathrm{Z}_j \cdot \mathrm{N}_j. \tag{2.6}$$

For example, for fully ionized CH multiple ion species plasma, the quasi-neutrality condition is given by, $N_e = Z_H N_H + Z_C N_C$, where the subscripts, e, H, and C stands for electron, Hydrogen, and Carbon, respectively.

2.1.2 Plasma Frequency

The plasma frequency is the natural frequency of oscillations and most fundamental time scale in the plasma physics. Plasmas are known to be quasi-neutral [see Eq. (2.6)], but the problem arises when electrons are displaced from their equilibrium position by some external force. The displacement of electrons leads to the generation of a charge-imbalance electrostatic field which tries to restore the electrons in the equilibrium position. Due to the conservation of the momentum the electrons overshoot; and oscillates around the equilibrium position. The frequency of these oscillations is known as the electron plasma frequency (ω_{pe}).

$$\omega_{pe} = \sqrt{\frac{N_e e^2}{\epsilon_0 m_e}}, \tag{2.7}$$

where, e, m_e and N_e are the electron charge, mass and density, respectively. The above relation can be simplified as

$$\omega_{pe} = 5.64 \times 10^4 \sqrt{N_e}, \tag{2.8}$$

where, N_e is in cm^{-3}. Plasma prevents the propagation of an electromagnetic disturbance with a frequency lower than plasma frequency. Therefore, plasma is opaque to any electromagnetic perturbation with a frequency, $\omega < \omega_{pe}$. The threshold for electromagnetic radiation, $\omega = \omega_{pe}$ can be written in term of the density, known as the critical plasma density, N_{cr}. The rearrangement of Eq. (2.7) gives the critical plasma density as a function of the incident frequency, ω

$$N_{cr}(\omega) = \frac{\epsilon_0 m_e \omega^2}{e^2} \simeq 1.1 \times 10^{21} \left(\frac{\lambda}{\mu m}\right)^{-2} cm^{-3}. \tag{2.9}$$

This critical plasma density defines an essential limit for the incident electromagnetic radiation and matter interaction. A plasma which is opaque to the incident electromagnetic radiation of frequency ω, having a density, $N_e > N_{cr}(\omega)$ is known as the 'overdense' plasma density. A plasma with a density, $N_e < N_{cr}(\omega)$ is transparent to the incident radiation is referred to as the 'underdense' plasma density.

The plasma frequency can be used to describe the quasi-neutrality of the plasma, which is similar to the Debye-length. The plasma is quasi-neutral for a plasma frequency with a time scale, $\tau >> 1/\omega_{pe}$ and for Debye-length with a length scale, $L >> 1/\lambda_{De}$. The charge imbalance can occur for a length, $L << 1/\lambda_{De}$, and time scale $\tau << 1/\omega_{pe}$. As these two parameters indicate the length and time scales, a characteristic velocity scale can be obtained from these parameters. This velocity scale is described as the thermal velocity of the

electrons, V_{th},

$$V_{th} = \omega_{pe}\lambda_{De} = \sqrt{\frac{k_B T_e}{m_e}}. \tag{2.10}$$

2.1.3 The Dispersion Relation

All (*classical*) electromagnetic phenomenon in plasma physics can be described with the help of Maxwell's equations [90];

$$\nabla \cdot \mathbf{E} = \frac{\rho}{\epsilon_0}, \tag{2.11}$$

$$\nabla \cdot \mathbf{B} = 0, \tag{2.12}$$

$$\nabla \times \mathbf{E} = -\frac{\partial \mathbf{B}}{\partial t}, \tag{2.13}$$

$$\nabla \times \mathbf{B} = \mu_0 \mathbf{J} + \mu_0 \epsilon_0 \frac{\partial \mathbf{E}}{\partial t}. \tag{2.14}$$

Here, $\mathbf{E}$ and $\mathbf{B}$ indicate the electric and magnetic fields, respectively, $\mathbf{J}$ is the current density, μ_0 and ϵ_0 are the permeability and permittivity of free space, respectively. Equations (2.11) and (2.12) are the Gauss' law for the electric and magnetic fields. The time-varying electric and magnetic fields are given by Eqs. (2.13) and (2.14) known as the Faraday's law and the Ampere's law, respectively.

For an electromagnetic perturbation, we can assume that the ion motion is negligible compared to the motion of electrons because of their heavy mass (m_p = 1836 m_e). Thus for a collisionless plasma, the displacement current is stated as $\mathbf{J} = eN_e\mathbf{V}_e$, where $\mathbf{V}_e$ is the velocity of the electrons. By differentiating the fourth Maxwell's Eq. (2.14), and using the value of $\mathbf{J}$, we obtain

$$\nabla(\nabla \cdot \mathbf{E}) - \nabla^2 \mathbf{E} = -\frac{\omega^2}{c^2}\epsilon_0 \mathbf{E}. \tag{2.15}$$

For a quasi-neutral plasma, the Gauss' law, i.e. Eq. (2.11) reduced to $\nabla \cdot \mathbf{E}$ = 0, by using this value in the above equation, one can obtain the dispersion relation,

$$\omega^2 = \omega_{pe}^2 + k^2 c^2, \tag{2.16}$$

where, k is the wavenumber and the refractive index (η) can be obtained by rearranging the Eq. (2.16)

$$\eta = k\frac{c}{\omega} = \sqrt{1 - \frac{\omega_{pe}^2}{\omega^2}}. \tag{2.17}$$

This dispersion relation rules out the dispersion characteristic properties of the electromagnetic waves in $\omega - k$ space. The phase velocity of a wave is

$$V_{ph} = \frac{\omega}{k} = \frac{c}{\eta} = \frac{c}{\sqrt{1 - \frac{\omega_{pe}^2}{\omega^2}}}, \tag{2.18}$$

which gives the direction and speed of the propagation of the wavefront or phase. The group velocity of the wave, $V_g = \frac{d\omega}{dk}$, gives the direction of the flow of energy and the information contained in the wave, i.e.

$$V_g = \frac{c^2 k}{\omega} = c\sqrt{1 - \frac{\omega_{pe}^2}{\omega^2}}. \tag{2.19}$$

It is clear from the above equations, any electromagnetic wave with a frequency $\omega > \omega_{pe}$, the refractive index of the plasma is less than one ($\eta < 1$). Thus the wave can pass through the plasma, and the group velocity of the wave will be less than the speed of light ($V_g < c$). For $\omega = \omega_{pe}$, the group velocity of the wave become zero ($V_g = 0$) and the phase velocity goes to infinity ($V_{ph} \to \infty$), the wave will be reflected back.

For solid density plasma, i.e., $\omega < \omega_{pe}$ the wavenumber, k becomes imaginary, and the amplitude of the wave start decreasing exponentially over a characteristic distance, known as the skin depth, δ. This is the distance over which an electromagnetic wave can penetrate farther from the critical density surface. The skin depth is given by

$$\delta = \frac{c}{\omega_{pe}}. \tag{2.20}$$

Inside the skin depth region, the electric field of the electromagnetic wave accelerates the electrons, and the energy is dissipated via collisions with the ions. The skin effect is more effective when the mean-free-path of the electrons is lower than the skin depth.

2.2 Basics of laser field

Generally, a high coherent electromagnetic wave is known as the laser light. And Maxwell's Eqs. (2.11-2.14) can be used to describe laser fields. In Eqs. (2.11-2.14) symbols in bold letter indicate the vector quantities. The electric and magnetic fields can be represented by the vector potential, $\mathbf{A}$ and scale potential, Φ [90], i.e.

$$\begin{aligned} \mathbf{E} &= \frac{\partial \mathbf{A}}{\partial t} - \nabla\Phi, \\ \mathbf{B} &= \nabla \times \mathbf{A}. \end{aligned} \tag{2.21}$$

By applying the Lorentz gauge transformation $\nabla \cdot \mathbf{A} + \frac{1}{c^2}\frac{\partial \Phi}{\partial t} = 0$ to the Maxwell's equations, the symmetric wave equations are obtained

$$\begin{aligned} \frac{1}{c^2}\frac{\partial^2 \mathbf{A}}{\partial t^2} - \Delta\mathbf{A} &= \mu_0 \mathbf{J}, \\ \frac{1}{c^2}\frac{\partial^2 \Phi}{\partial t^2} - \Delta\Phi &= \frac{\rho}{\epsilon_0}. \end{aligned} \tag{2.22}$$

Here $c = 1/\sqrt{\epsilon_0 \mu_0}$ is the speed of light in vacuum.

The simplest solution of Eq. (2.22) in vacuum can be expressed as the sinusoidal plane wave of form

$$\mathbf{A} = \mathbf{A}_0 \sin(\mathbf{k}_0 \cdot \mathbf{r} - \omega_0 t + \varphi_0), \tag{2.23}$$

where $\mathbf{k}_0$ is the wave vector with amplitude $k_0 = \omega_0/c$, φ_0 is the initial phase, and ω_0 is the angular frequency of the wave. This is the solution for a linearly polarized wave. And also Eq. (2.22) can be used to find the solution for a elliptically polarized wave.

By using the value of vector potential from Eq. (2.21), the electric and magnetic fields are given by

$$\begin{aligned} \mathbf{E} &= \mathbf{E}_0 \cos(\mathbf{k}_0 \cdot \mathbf{r} - \omega_0 t + \varphi_0), \\ \mathbf{B} &= \mathbf{B}_0 \cos(\mathbf{k}_0 \cdot \mathbf{r} - \omega_0 t + \varphi_0), \end{aligned} \tag{2.24}$$

with the relationship between all the amplitude

$$\mathrm{E}_0 = \omega_0 \mathrm{A}_0 = c\mathrm{B}_0. \tag{2.25}$$

The laser intensity can be given by the time-average of magnitude of the Poynting vector, i.e. $\mathbf{S} = \frac{1}{\mu_0}\mathbf{E} \times \mathbf{B}$. By using Eq. (2.24)

$$\mathrm{I}_0 = <\mathrm{S}> = \frac{1}{2}\epsilon_0 c \mathrm{E}_0^2. \tag{2.26}$$

2.2.1 Relativistic Laser Intensity

The equation of motion of an electron in an electromagnetic field can be obtained from the Lorentz equation

$$\mathbf{F} = -e(\mathbf{E} + \mathbf{V}_e \times \mathbf{B}), \tag{2.27}$$

where, $\mathbf{F} = \frac{d\mathbf{P}}{dt}$ is the Lorentz force, $\mathbf{P} = \gamma_e \, \mathrm{m}_e \mathbf{V}_e$ is the relativistic momentum of the electrons with a velocity $\mathbf{V}_e$, and relativistic factor $\gamma_e = 1/\sqrt{1 - \mathrm{V}_e^2/c^2}$. It is clear from Eq. (2.27), the motion of the electrons is supervised by the electric and magnetic forces. The motion of the electrons under the action of the electric field is known as the quiver motion in the direction of an electric field, and the maximum velocity is known as the quiver velocity, $\mathrm{V}_m^{qv} = \frac{e\mathrm{E}_0}{\mathrm{m}_e\omega_0}$. The second component of the motion of the electrons is originated from the $\mathbf{V}_e \times \mathbf{B}$ component, which is in the direction of the laser propagation. It can be interpreted from Eq. (2.25) that the ratio between the electric and $\mathbf{V}_e \times \mathbf{B}$ forces is $\mathrm{V}_m^{qv}/\mathrm{c}$. This ratio can be used to characterize an important laser parameter, known as the dimensionless laser vector potential, a_0. This parameter is used more frequently in high-intensity laser physics rather then the amplitude of the electric and magnetic fields. The laser vector potential is given by,

$$\mathrm{a}_0 = \frac{\mathrm{V}_m^{qv}}{c} = \frac{e\mathrm{E}_0}{\mathrm{m}_e\omega_0}. \tag{2.28}$$

For $a_0 << 1$, non-relativistic laser intensity, $V_m^{qv} << c$, so the magnetic force component $\mathbf{V}_e \times \mathbf{B}$ can be neglected, and the electrons essentially oscillates in the plane of an electrostatic field. For $a_0 >> 1$, ultra-relativistic laser intensity, the two forces become nearly the same, and the maximum quiver velocity of the electrons becomes comparable to the speed of light. And the electrons are pushed in the direction of the laser propagation. Therefore, $a_0 = 1$ specify the relativistic threshold for the laser intensities. The corresponding electric and magnetic field amplitude are given by

$$\begin{aligned} E_0 &= \frac{3.2 \times 10^{12}[V/m]}{\lambda[\mu m]} a_0, \\ B_0 &= \frac{1.07 \times 10^{4}[T]}{\lambda[\mu m]} a_0. \end{aligned} \tag{2.29}$$

By coupling Eq. (2.26) and Eq. (2.28), the relation between the a_0 and laser intensity can be obtained

$$I_0 = \zeta \frac{1.37 \times 10^{18}[W cm^{-2}]}{\lambda^2[\mu m^2]} a_0^2, \tag{2.30}$$

where λ is the wavelength of the laser, and the value of the corrected coefficient, ζ is determined by the polarization of the laser. For linear polarization, $\zeta = 1$, and for circular polarization $\zeta = 2$.

For the numerical and experimental investigations, the laser pulse has a perfect Gaussian profile in space and time. So the peak laser intensity of the laser depends on pulse width and spot-size of the laser.

$$I_0[W cm^{-2}] = \frac{0.83 E_L[J]}{t_{FWHM}[s] \cdot d_{FWHM}^2[cm^2]}. \tag{2.31}$$

Here, subscript FWHM denotes the full-width at half-maximum, E_L is the laser energy, t and d are the time duration and diameter of the focal spot size, respectively.

2.3 Relativistic Transparency

When a high-intensity laser interacts with the plasma, the oscillation velocity of electrons nearly becomes equal to the speed of light, c. This results in the relativistic mass increase of electrons and a relativistic factor, γ must be included in the electron plasma frequency. For a fixed wavelength laser pulse this γ factor effectively increases the critical plasma density, $N_{eff} = N_e/\gamma$. The plasma can be transparent theoretically

$$N_{cr} < N_e < \gamma N_{cr}. \tag{2.32}$$

The relativistic factor γ depends on the polarization of the laser pulse, such that for linear polarization $\gamma = \sqrt{1 + a_0^2}$, and for circular polarization $\gamma = \sqrt{1 + \frac{a_0^2}{2}}$.

Thus, the relativistically corrected refractive index of the plasma is given by

$$\eta = \sqrt{1 - \frac{\mathrm{N}_{cr}}{\gamma \mathrm{N}_e}} = \sqrt{1 - \frac{\omega_{pe}^2}{\gamma \omega^2}}, \tag{2.33}$$

where N_{cr} is the non-relativistic critical plasma density. The refractive index becomes non-linear after including the relativistic effect.

2.4 Laser Absorption Mechanism

The energy transfer from a laser pulse to the plasma is very essential in laser-plasma interaction. To understand the physical mechanism responsible for laser absorption in plasmas, a wide range of materials are available [91–93]. Several mechanisms have been proposed through which the laser energy coupled with the plasma. In this section, we will summarise some of the fundamental laser absorption mechanisms in the collisionless plasmas.

2.4.1 Resonance Absorption

Resonance absorption is a collisionless absorption mechanism [94]. This mechanism is one of the relevant mechanism for laser absorption in plasmas, which occurs at the critical density surface. When a linearly p-polarized laser pulse is incident on a plasma density gradient, and it results in the excitation of a plasma wave. Here, the component of the laser electric field is normal to target. The electrostatic field of the laser decreases exponentially over a distance, known as plasma skin depth. In the presence of the electrostatic field component, the electrons oscillate in the direction normal to the target and lead to the charge density fluctuations, $\mathrm{E}_L \nabla \cdot \mathrm{N}_e \neq 0$. At critical density plasma, this density perturbation can become resonant with the plasma frequency, i.e., $\omega_{pe} = \omega_L$. This suggests that the penetrating laser electric field drives the oscillations of the electrons. A high laser intensity induces a plasma wave at the critical density, which can transfer the energy to the plasma through wave breaking [44]. This energy transfer leads to the hot-electron generation, and their temperature can be scaled as $\mathrm{T}_e \propto \mathrm{I}_0^{1/3} t_L^{1/6}$ [95]. This absorption mechanism is known as the Resonance absorption.

2.4.2 Vacuum Heating

Resonance absorption is useful for a plasma with a short density scale-length on the front side. This absorption mechanism breaks down for steep density gradient plasma, where the plasma density scale-length becomes smaller compared to the electron oscillations wavelength along the plasma density gradient. The vacuum heating or Brunel heating [96] becomes important for relativistic intensity laser ($\mathrm{a}_0 > 1$) obliquely incident on the steep density plasmas. Let's consider θ is the angle of incidence for p-polarized laser pulse on a solid density plasma, and laser cannot penetrate beyond the plasma skin depth (c/ω_{pe}). The electrons near the plasma-vacuum interface directly interact with the laser

field and undergo large oscillations. The electrostatic field-aligned normal to the plasma boundary pulled out these electrons in the vacuum region. As the component of the electrostatic field reverses its direction, these electrons are sent back into the plasma. These accelerated electrons pass through the plasma beyond the plasma skin depth and traverse through it until they get absorbed via collisions. The values of $I_0\lambda^2$ and scale-length of the plasma decide the transition between the resonance absorption and vacuum heating for finite density gradient plasmas. As the field of the high-intensity laser can penetrate only up to the skin depth of the plasma, the vacuum heating is much larger than resonance absorption. The Brunel first described this heating mechanism, therefore known as the Brunel or vacuum heating.

2.4.3 J×B Heating

Kruer [44] and Estabrook [93] have suggested another heating mechanism, known as the J×B heating mechanism. This heating mechanism comes into the picture when the intensity of the laser pulse becomes high enough ($a_0 > 1$), such that the magnetic field component of the laser field starts contributing to the oscillations of electrons. In other words, the contribution from the J×B component of Lorentz force becomes comparable to the electrostatic force. For linearly-polarized laser pulse, the electrons are accelerated in the laser direction, and their longitudinal oscillations become twice of the laser frequency, i.e., $\omega = 2\omega_L$. It is already confirmed via numerical simulations that the J×B absorption increases with the increase in laser intensity (or a_0) and decreases with an increase in plasma density [42, 44, 97]. The scaling for hot electron

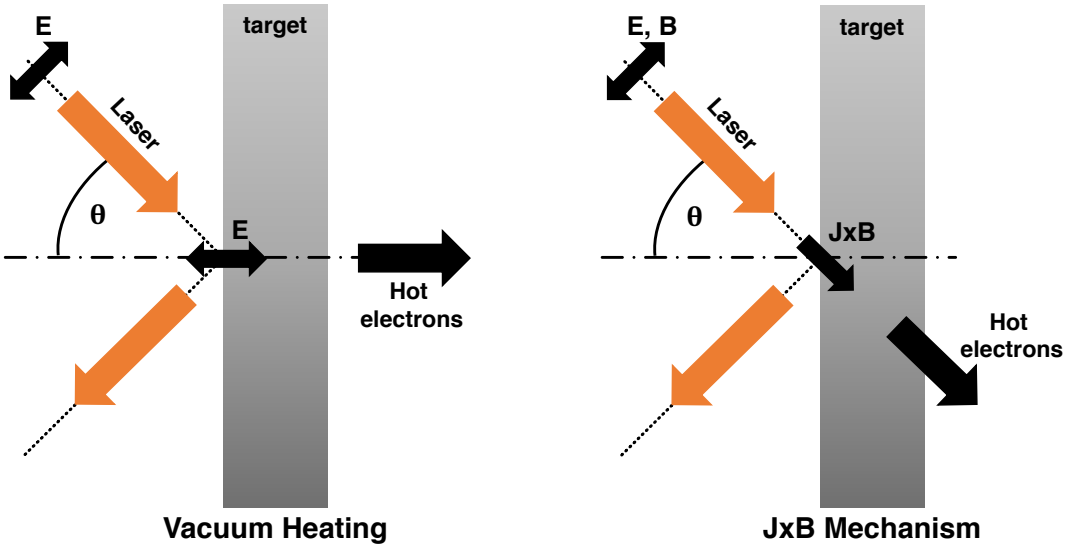


FIGURE 2.1: Schematic demonstration of collisionless absorption mechanism. *Left*; Vacuum heating or Brunel absorption. *Right*; J×B absorption mechanism.

temperature can be given by

$$\mathrm{T_{hot}} = (\gamma - 1)\mathrm{m}_e c^2 = \left(\sqrt{1 + \frac{\mathrm{a}_0^2}{2}} - 1\right)\mathrm{m}_e c^2. \tag{2.34}$$

As electrons gain energy from the transverse component of the laser electric field, energy gain of the electrons is of the order of the ponderomotive potential energy of the laser field. This is because the above relation is similar to the ponderomotive potential energy of the electrons. The J×B mechanism becomes more efficient, for a normally incident relativistic laser intensity $\mathrm{a}_0 > 1$, where the laser electric field is parallel to the plasma density. This mechanism has been confirmed experimentally by Malka [98]. Apart from circularly polarised, this mechanism works for any other polarizations of the laser pulse.

Chapter 3

Particle-in-cell Technique

3.1 Introduction

The development of high-performance supercomputers in last 60 years manifests a new way to study the complicated nature of plasma physics problems by adopting the computer simulations, which led to the development of plasma theory. In 1963, Buneman and his co-workers introduced fixed spatial grid method to describe the field, potentials, and charge densities. This grants a faster computational way to deal with the motion of a large number of particles. Depending on the interpolation technique applied, the charge of each particle is interpolated with its neighbour grid point in "particle-in-cell" approach. At every grid points, the progression in the field values can be determined by the differencing method. These values of the field are fundamental to quantify the particle acceleration. After knowing the acceleration of particles, a leapfrog or Runge-Kutta method can be utilized to update the position of the particle. The books by *Birdshell* & *Langdon* [99] and *Hockney* & *Eastwood* [100] provide the comprehensive inspections and background for the particle-in-cell approach. Within the same cell, the reduction of forces within the computational particles is significantly affected by the finite spatial grid, where the field values are determined. The force between the two particles is inversely proportional to the square of the distance, (r) between the two particles, i.e., Coulomb force, $F \propto 1/r^2$. This implies that the force between the two particles increases when they move closer if they become very close to each other, particles will experience strong and changing force. At the same moment, the collective behaviour of plasma comes into the picture by interaction over large distances induced by the slow tail of the Coulomb force. The separation within the two particles is smaller than the separation between the two grid points. The finite grid approach is used to calculate the force between the particles, which presents a reduction in the Coulomb force among two particles. As in simulations, Coulomb force between the particles increases on the short distances; this is the reason that the simulation particles can describe as many real particles. In a finite grid approach, the behaviour of the particles is characterized by finite-sized particles, not by the classical point particles. This is because the charge of computational particles is suppressed over their neighbouring grid points. The force between these finite-sized particles starts decreasing when they start overlapping each other. In the meantime, the collective behaviour of the plasma remains the same, as the Coulomb force between the particles is the same through the long distances.

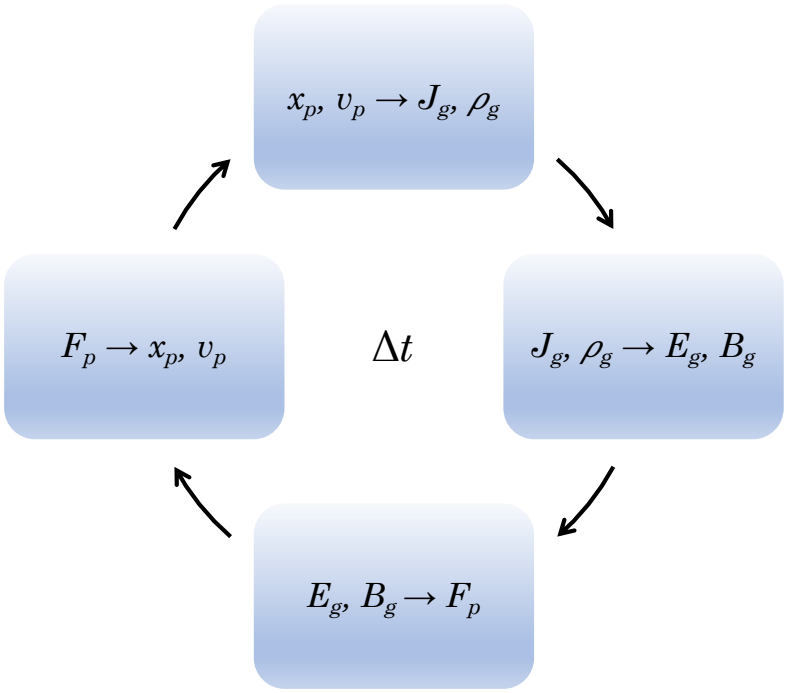


FIGURE 3.1: Schematic of a typical timsetup for particle-in-cell code.

Figure 3.1 describes the standard approach for the PIC code in a cyclic fashion. The charge and current densities on the grid positions can be determined by using the particle positions and velocities, i.e., x_p and $v_p \rightarrow \rho_g$ and J_g, where the subscripts p and g represent the particle properties and grid quantities, respectively. Now the value of the charge and current densities can be used to advance the field with time, which can be used to determine the force acting on the particles, i.e., ρ_g and $\mathrm{J}_g \rightarrow \mathrm{E}_g$ and $\mathrm{B}_g \rightarrow \mathrm{F}_p$. Now this force can be utilized to determine the new particle positions and velocities; thus, the particle moved a step forward in the time.

3.2 Particle-in-cell Approach

This section illustrates the fundamental equations for the simulation code to simulate the laser-plasma interaction. EPOCH particle-in-cell open source code in the two-dimensional geometry is employed to generate the simulation results discussed in this thesis. EPOCH environment is not much different from the one describes here, and EPOCH includes more terms in Maxwell's equations to define the further spatial dimension involved. The books *Birdshell & Langdon* [99] and *Hockney & Eastwood* [100] present a more detailed description of two-dimensional simulation code working principle.

3.2.1 Field Advancing

In order to promote the electromagnetic field with time, the Maxwell's equations [see Eqs. (2.11-2.14)] are solved by finite difference method in particle-in-cell code. This section gives an overview of equations used to update the fields.

The Maxwell-Ampere law given by Eq. (2.14), and Gauss's law [see Eq. (2.11)] are utilized to estimate the progression in the electric field, and Faraday's law given by Eq. (2.13) can be used to find the advancement in the magnetic field.

All field values are determined at the grid positions. And a centered differencing technique is employed to solve the derivative of the field quantities, which can be rewritten as differential equations. This method gives accuracy to the second-order in both space and time. For two-dimensional case, as the particles can travel in both x and y directions, but for the sake of simplicity, we will examine the movement of the particles along with the x-axis only. Therefore, Eq. (2.14) and Eq. (2.13) can be written as

$$\frac{\left(E_{y_g}^{s+1} - E_{y_g}^{s}\right)}{\Delta t} = -\left(\frac{J_{y_g}^{s+\frac{1}{2}}}{\epsilon_0}\right) - c^2 \frac{\left(B_{z_{g+\frac{1}{2}}}^{s+\frac{1}{2}} - B_{z_{g-\frac{1}{2}}}^{s+\frac{1}{2}}\right)}{\Delta x}, \tag{3.1}$$

$$\frac{\left(B_{z_{g+\frac{1}{2}}}^{s+\frac{1}{2}} - B_{z_{g+\frac{1}{2}}}^{s-\frac{1}{2}}\right)}{\Delta t} = -\frac{\left(E_{y_{g+1}}^{s} - E_{y_g}^{s}\right)}{\Delta x}. \tag{3.2}$$

Here, superscript 's' symbolizes the current time step and subscript 'g' signifies the grid positions.

The advancement in the electric and magnetic fields can be obtained by rearranging Eqs. (3.1) and (3.2). At first, a half time step advancement happens in the magnetic field, which can be given by

$$B_{z_{g+\frac{1}{2}}}^{s} = B_{z_{g+\frac{1}{2}}}^{s-\frac{1}{2}} - \frac{\Delta t}{2\Delta x}(E_{y_{g+1}}^{s} - E_{y_g}). \tag{3.3}$$

After knowing the value of the magnetic field along the halfway (halfway progression), the Maxwell-Ampere relation [see Eq. (2.14)] can be used to determine the advancement in the electric field, E_y as follows

$$E_{y_{g+1}}^{s} - E_{y_g} = \frac{c^2}{\Delta x}\left(B_{z_{g-\frac{1}{2}}}^{s+\frac{1}{2}} - B_{z_{g+\frac{1}{2}}}^{s+\frac{1}{2}}\right)\Delta t - \left(\frac{J_{y_g}^{s+\frac{1}{2}}}{\epsilon_0}\right)\Delta t. \tag{3.4}$$

Similarly, Gauss' law gives the advancement in electric field along the x-axis, E_x

$$E_{x_{g+1}}^{s} = E_{x_g}^{s} + \left(\frac{\rho_{g+\frac{1}{2}}^{s}}{\epsilon_0}\right)\Delta x. \tag{3.5}$$

The above Eqs. (3.3), (3.4), and (3.5) designate the advancement in the magnetic (B_z), and electric (E_y and E_x) fields in Δt time, respectively. Once the magnetic field has been advanced through the halfway, then the electric field will be advanced further. Similarly, after advancing the electric field, the advancement of the magnetic field happens again through the halfway and so on. This is a cyclic process, as shown in Fig. 3.1.

3.2.2 Particle Velocity Progression

When both the electric and magnetic fields are known at the same time, the centred difference method can be applied to the equation of motion to obtain the progression in the particle velocity. The relativistic Lorentz force is given by

$$\mathbf{F} = m\frac{d\mathbf{v}}{dt} = q\left(\mathbf{E} + \frac{1}{\gamma}\mathbf{v} \times \mathbf{B}\right), \tag{3.6}$$

where $\mathbf{v} = \gamma\mathbf{u}$ is the relativistic velocity, and γ is the relativistic Lorentz factor. By applying the centred difference method, the above equation can be rewritten as

$$\frac{\mathbf{v}^{s+\frac{1}{2}} - \mathbf{v}^{s-\frac{1}{2}}}{\Delta t} = \frac{q}{m}\left(\mathbf{E}^s + \frac{\mathbf{v}^{s+\frac{1}{2}} + \mathbf{v}^{s-\frac{1}{2}}}{2\gamma^s} \times \mathbf{B}^n_{avg}\right). \tag{3.7}$$

Here $\mathbf{B}_{avg}$ signifies the averaged magnetic field. As on every time step, the magnetic field is forwarded only in the halfway. Thus an averaged magnetic field needs to be used where the electric field value is known. A method design by Boris [101] is used to solve Eq. (3.7) and by defining $\mathbf{v}^+$ and $\mathbf{v}^-$ as follows

$$\mathbf{v}^+ = \mathbf{v}^{s+\frac{1}{2}} - \frac{q\mathbf{E}^s}{2m}\Delta t, \tag{3.8}$$

$$\mathbf{v}^- = \mathbf{v}^{s-\frac{1}{2}} + \frac{q\mathbf{E}^s}{2m}\Delta t. \tag{3.9}$$

By putting these values in Eq. (3.7), we obtain

$$\frac{\mathbf{v}^+ - \mathbf{v}^-}{\Delta t} = \frac{1}{2\gamma^s m}(\mathbf{v}^+ + \mathbf{v}^-) \times \mathbf{B}^s_{avg}. \tag{3.10}$$

Equation (3.10) results in a rotation of $\mathbf{v}$ about an axis parallel to $\mathbf{B}$ by an angle θ = -2tan$^{-1}\left(\frac{\mathrm{qB}\Delta t}{2\gamma^s \mathrm{m}}\right)$. Here $\gamma^s = 1/\sqrt{1 + (\frac{\mathbf{v}^-}{c})^2}$. Since, γ^s has the time reversal symmetry, it can be used to find the time centred kinetic energy.

In a physical system of problems, v_z, E_z, B_x and B_y are not that much significant. The equation of motions reveals that, if these quantities are defined as zero, they will remain zero. The Buneman's algorithms [99] can be used to describe the plane rotation by Eq. (3.10)

$$\mathbf{v}' = \mathbf{v}^- + \mathbf{v}^- \times \mathbf{t}, \tag{3.11}$$

$$\mathbf{v}^+ = \mathbf{v}^- + \mathbf{v}' \times \mathbf{n}. \tag{3.12}$$

Here $\mathbf{t} = q\mathbf{B}\Delta t/2\gamma m$ and $\mathbf{n} = 2\mathbf{t}/(1 + \mathbf{t}^2)$. By putting these values in Eq. (3.7), the updated particle positions can be obtained.

The particle position can be updated by using the updated particle velocity as follows

$$\mathbf{x}^{s+1} = \mathbf{x}^{s} + \mathbf{v}^{s+\frac{1}{2}}\Delta t = \mathbf{x}^{s} + \left(\frac{\mathbf{v}^{s+\frac{1}{2}}}{\gamma^{s+\frac{1}{2}}}\right)\Delta t. \tag{3.13}$$

3.2.3 Finite Difference Method Stability

The stability and accuracy of the scheme [102] can be interpreted by analyzing the behaviour of Maxwell's equation [Eqs. (2.11-2.14)] for the electromagnetic waves in vacuum. By assuming the electromagnetic wave is propagating in the x-direction, the electric and magnetic field can be given by

$$\begin{aligned} \mathbf{E} &= \mathbf{E}_0 \exp\{i(kx - \omega t)\}, \\ \mathbf{B} &= \mathbf{B}_0 \exp\{i(kx - \omega t)\}. \end{aligned} \tag{3.14}$$

By utilizing these values in differenced Maxwell's equations, we get

$$\mathbf{\Omega} = c^2\mathbf{K}, \tag{3.15}$$

where

$$\begin{aligned} \mathbf{\Omega} &= \left(\frac{2}{\Delta t}\right)\sin\left(\frac{\omega\Delta t}{2}\right), \\ \mathbf{K} &= \left(\frac{2}{\Delta x}\right)\sin\left(\frac{k\Delta x}{2}\right). \end{aligned} \tag{3.16}$$

For a continuous system, $\mathbf{\Omega} \to \omega$ and $\mathbf{K} \to k$, consequently result into simple solution $\omega = ck$. Courant-Friedrichs-Lewy (CFL) conditions set a limit on the timestep, which is used to determine the progression in the fields. The CFL conditions state that the one grid spacing must be larger than the distance traveled by the wave in one timestep. For one dimensional simulation, the stability of the system can be determined as

$$\Delta x^2 \geq \Delta t^2 c^2. \tag{3.17}$$

Although for two- and three-dimensions, some additional terms must be added to the CFL conditions. Thus for three-dimension CFL condition can be given by

$$\frac{1}{\Delta x^2} + \frac{1}{\Delta y^2} + \frac{1}{\Delta z^2} > \frac{1}{\Delta t^2 c^2}. \tag{3.18}$$

The dissatisfaction of the above condition leads to the unwanted unphysical growth in the system, which arises due to the complex part of ω.
The basics of a PIC code can be summarised through the following steps:
Let's start with the initial values of the particles, E^s, B^s, x^s and $v^{s-\frac{1}{2}}$.

1. E^s and B^s denote the average electric and magnetic fields to the particle grid.

2. Calculate the new particle velocities and positions;
   $v^{s-\frac{1}{2}} \to v^{s-\frac{1}{2}}$ and $x^s \to x^{s+1}$.

3. Advance the J and ρ at the grid positions;
   $J^{s-\frac{1}{2}} \rightarrow J^{s+\frac{1}{2}}$, and $\rho^{s} \rightarrow \rho^{s+1}$.

4. By using E^{s}, advance magnetic field, B^{s} by a half timestep;
   $B^{s} \rightarrow B^{s+\frac{1}{2}}$.

5. By using $J^{s+\frac{1}{2}}$ and $B^{s+\frac{1}{2}}$ advance the electric field;
   $E^{s} \rightarrow E^{s+1}$.

6. By using E^{s+1} advance the magnetic field by the remaining half;
   $B^{s+\frac{1}{2}} \rightarrow B^{s+2}$.

3.3 EPOCH Framework

EPOCH stands for; **E**xtendable **P**IC **O**pen **C**ollaboration **H** [103]. This is an open-source code developed by the collaboration between the Imperial College, Warwick University, and Oxford University. All results displayed in this thesis use the two-dimensional (2D) version of the EPOCH 4.7.3 model. Nevertheless, this code is also accessible in 1D, 2D, and 3D versions. The algorithm used for field updating and particle movers in this code is pretty much related to the PSC code by Hartmut Ruhl. EPOCH is explicit, fully relativistic, and fully parallelized code with MPI-IO, which allow restart on an arbitrary number of processors. To overcome the numerical heating, it uses the 2nd order particle weighting as a standard model. This code produces an output file which can be directly readable by the programs such as ITT IDL, VisIT, LLNL, Mathworks MATLAB. Throughout this thesis, all the plots and figures are produced by utilizing the MATLAB code. The EPOCH code applies a modified leapfrog scheme to update the electromagnetic fields. In this scheme, fields are updated on the half in a full-time step. To examine the interaction of laser with plasmas, EPOCH is an excellent choice. We use the standard particle weighting, which is the 2nd order particle weighting, to reduce the numerical heating. The desirable particle weighting can illustrate the link between the particle properties and grid quantities with one fundamental property, which can be stated as grid always see a particle with a 'finite-size' as they move around. Thus in simulations, particles are always examined as the finite-size particles, not the point particles. Easy expansion of the EPOCH code can be made possible by adding structure and modern features to the code in the future.

Chapter 4

Laser-Driven Ion Acceleration

4.1 Introduction

The study of the acceleration of charged particles persists one of the most relevant topics of research in space, astrophysical and laboratory plasma. In the last few years, the active growth in laser technology, the acceleration of charged particle has received an enormous amount of concentration in laser-matter interaction. Theoretical and simulation work done by Tajima & Dawson in 1979 [15], have shown that the non-linear pondermotive force generated in the intense electromagnetic pulses leads to the weak plasma oscillation, and a relativistic plasma can be suitable for the development of compact accelerators. In the proposed scheme, the externally injected relativistic electrons were accelerated through a very high (GVm^{-1}) electrostatic field maintained by the laser-driven relativistic plasma waves. Two schemes of acceleration have been proposed by Tajima & Dawson, known as 'laser beat' and 'laser wakefield.' Based on these schemes, the electron bunches are accelerated over a very short distances $\sim$ 3.3 cm to quasi-monoenergetic energy $\sim$ 1 GeV [19].

A direct interaction of electrons in an electric field produced by a currently accessible laser system can drive them to the relativistic oscillations. The relativistic threshold for the electrons is reached at an intensity 1.37×10^{18} Wcm^{-2} for common wavelengths of 1 μm, which accelerate the electron with a kinetic energy larger than their rest mass, the energy equivalent of 0.511 MeV. With the development in laser technology, the experiments on laser-driven ion acceleration have received significant attention in the field of laser-plasma interaction. In spite of that, it is difficult to accelerate the ions to a relativistic limit by the current laser system. Very high energy with the laser pulse amplitude $a_0 = 1836$ is needed to achieve the relativistic velocity for protons in one laser cycle, and the acceleration will enter in the Piston Regime [40]. Thus, the acceleration of the ions currently depends on the secondary effects such as the generation of hot-electron populations with the current laser system. The hot-electron population mediates the forces of the laser fields on the ions by generating the strong charge-imbalance electrostatic fields. Depending on the laser parameters (intensity, temporal contrast) and target properties (shape and size), the laser energy can be transferred to the electrons by various mechanisms as discussed in Chapter 2. In this chapter, we will examine the different ion acceleration scenario, in which the strong electrostatic field accelerates the charged particles for a sufficiently long time. In the primary ion-acceleration scenarios, the fast hot-electrons generated in the laser-plasma interaction pass through the targets

and escape to the vacuum by leaving behind the massive ions, as a consequence a space-charge field is generated on the rear side of the target. This field accelerates the ions from normal the rear surface of the target. This mechanism is known as the target normal sheath acceleration (TNSA) [31, 33]. The another acceleration scenario is known as the radiation pressure acceleration (RPA) [32, 40], in which the ions are accelerated from the front surface of the target by laser radiation pressure. Based on the laser parameters and target thickness, this mechanism can be further categorised into the two schemes, which will be discussed in this chapter. Recently, another scheme of ion acceleration known as the electrostatic collisionless shock ion acceleration (CSA) [42, 43] has attracted most of the attention.

4.2 Target Normal Sheath Acceleration (TNSA)

Wilks et al. [33] first introduced the TNSA mechanism to understand the ion acceleration from the rear-side of a thin-foil target in laser-solid interaction. According to the TNSA model, the interaction of high-intensity laser ($a_0 > 1$) with a thin-foil solid target results in the generation of high-energy "hot electron" population on the front side of the target. These hot electrons progress through the bulk of the target and reach the back surface without any considerable energy loss. The fastest electron escapes into the vacuum, while the positively charged ions remain at rest due to their heavy mass. When N_e^h, and T_e^h are the hot electron density and temperature, respectively, and L_{sh} is the spatial sheath extension of the electrons, a sheath electrostatic field, $E_{\text{sheath}} \sim T_e^h/eL_{sh}$ appears on the rear-side of the surface. L_{sh} is approximately determined by the Debye length (λ_{De}^h) of the hot electrons

$$L_{sh} \approx \lambda_{De}^h = \sqrt{\frac{\epsilon_0 k_B T_e^h}{e^2 N_e^h}}. \tag{4.1}$$

Thus, λ_{De}^h defined the range over which significant charge separation occurs. Aforementioned this charge-separation electrostatic field can be scaled as

$$E_{\text{sheath}} = \frac{k_B T_e^h}{e\lambda_{De}^h}, \tag{4.2}$$

giving rise to the longitudinal electric field of an order of TVm^{-1}. This sheath field depends on the number density and temperature of hot electrons, and the rear-surface density profile. The electrostatic field on the rear-side of the target accelerates the ions to very high energy. The strength of this electrostatic field is much higher than the laser electric field; it ionizes the rear-surface of the target and starts accelerating the ions to high energy. Due to the low charge-to-mass ratio, the response of the protons to the electrostatic field is faster compared to the other ions. This is the reason why the acceleration of the only proton is observed in the early experiments [105]. The energy of accelerated ions strongly depends on the profile of the sheath electrostatic field created by the hot electrons. These fields emerge from the front, and backside of the target,

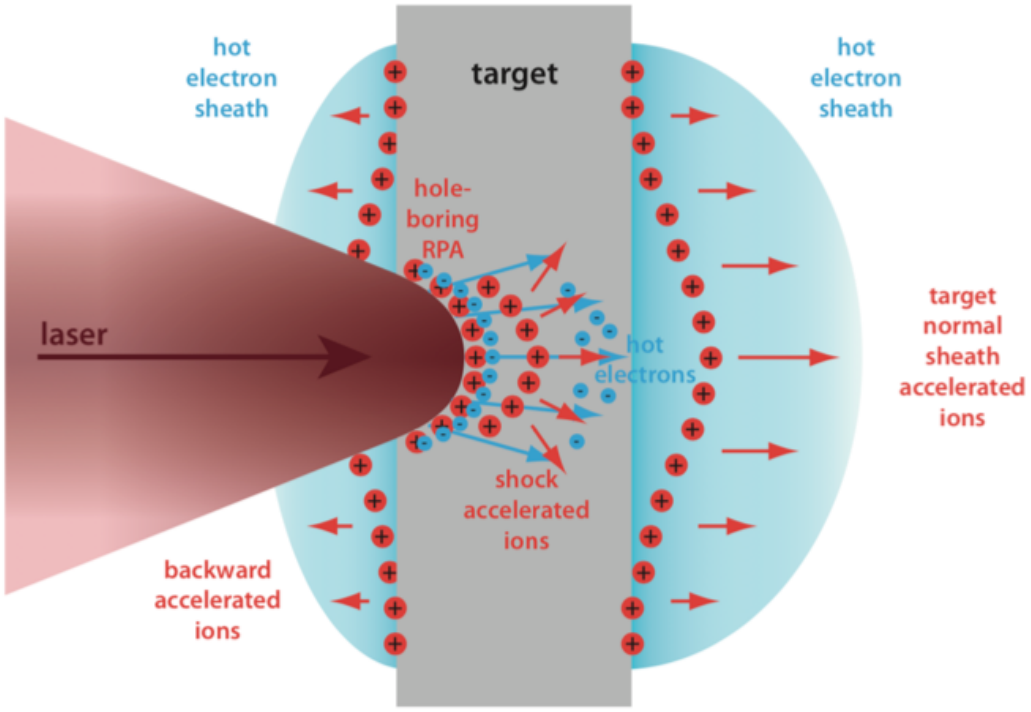


FIGURE 4.1: Schematic of ion acceleration in laser-solid interaction. The interaction of laser pulse with solid produces the hot electrons on front- and rear-sides of the target. These electrons develop the sheath field, which accelerates the ions in the target normal direction [taken from [104]].

which accelerates ions in the backward and forward directions. Correlations can roughly determine the energy of the accelerated ions

$$\varepsilon_i \sim \mathrm{ZE_{sheath}}\lambda_{De}^{h} = \mathrm{ZT}_e^{h}. \tag{4.3}$$

Consequently, the longitudinal electrostatic fields are directed along the normal to the target, allowing the ions to be accelerated perpendicular to the target surface. Therefore, this mechanism is known as the Target Normal Sheath Acceleration, TNSA. The spatial and angular distributions of the accelerated ion beams are given by the physical properties of the target and the electric field lines driven by the spatial distribution of the hot-electron density on the rear surface of the target.

4.2.1 Theoretical Model for TNSA

Many experiments have confirmed the generation of multi-MeV accelerated proton beams produced by the TNSA mechanism in the last preceding 10-15 years. The electrostatic potential approximation leads to a simple set of equations. The electric field is $\mathrm{E_{sheath}} = -\nabla\Phi$, where Φ is the potential. So, the Poisson's equation is given by

$$\nabla^2\Phi = \frac{e}{\epsilon_0}(\mathrm{N}_e - \sum_i \mathrm{Z}_i\mathrm{N}_i). \tag{4.4}$$

Where the summation is over each ion having charge Z_i and density N_i. Here N_e is the electron density, which can be defined by the cold (N_e^c) and hot (N_e^h) electron populations in laser-solid interaction, i.e.

$$N_e = N_e^c + N_e^h. \tag{4.5}$$

The charge-separation electrostatic field traps the main part of the hot-electron population, and a small population of hot electrons escapes in the target vicinity. This constitutes to an exponential sheath on the rear target surface. Therefore, the N_e^h can be described by the one-dimensional Boltzmann distribution

$$N_e^h = N_0^h \exp\left(\frac{e\Phi}{k_B T_e^h}\right). \tag{4.6}$$

Here, N_0^h is the density of hot electrons when $\Phi = 0$. As long as the laser pulse drives the hot-electron population within the target, the above correlations provide a good approximation to the self-consistent electrostatic sheath field, and many authors [106–108] have used the above described model. Most of the targets can be characterized by the light and heavy ion populations. Depending on these ion populations, the theoretical model of TNSA can be divided into the two categories, "static" and "dynamic" models, which provide the fundamental description and interpretation to the experimental data.

In the static model approximation, it is assumed that, in the early stage of sheath field formation, only the light ions are accelerated. Heavy ions can be considered as stationary/immobile. In this case, depending on the assumption of hot electron distribution to grant more accurate information about sheath field, the effect of the light ions on the electrostatic potential, Φ is usually neglected.

In the dynamic mode of TNSA, the system is characterized as neutral plasma, and the evolution of the sheath field acts as a source of kinetic energy for the ions. In most cases, this approach is quite similar to the expansion of plasma in vacuum [109, 110].

In cold fluid plasma approximation, the ions can be given by the simple correlations

$$\begin{aligned} \frac{\partial \mathbf{u}_i}{\partial t} + \mathbf{u}_i \cdot \nabla \mathbf{u}_i &= \frac{Z_i e \nabla \Phi}{m_i}, \\ \frac{\partial \mathbf{u}_i}{\partial t} + \nabla \cdot (N_i \mathbf{u}_i) &= 0, \end{aligned} \tag{4.7}$$

where 'i' symbolizes the light and heavy ions. In the dynamic model of the TNSA, the kinetic description of the plasma can be employed to characterize the kinetic phase-space of the ions. Thus, the Vlasov equation is

$$\frac{\partial f_i}{\partial t} + u\frac{\partial f_i}{\partial x} - \left(\frac{Z_i e \nabla_x \Phi}{m_i}\right)\frac{\partial f_i}{\partial u} = 0. \tag{4.8}$$

A suitable simplification of the above the equations can be used to describe the

specific models of TNSA although these models require some particular physical quantities, which are not principally known as their input parameters. The model which presents renovation for future applications and gives best relationships with the experimental data for the least number of laser parameters and targets can be acknowledged as the best model for TNSA mechanism.

4.2.2 Quasi-static Model

The static-model approximation considered that the heavy ions are fixed and the light ions can be viewed as a test particle, and their effect on the growth of the potential Φ can be overlooked with an isothermal electron population for a time scale of a sub-ps laser pulse. In quasi-static approximation, the electrostatic potential is calculated by using the hot-electron population given by Eq. (4.6), and neglecte the thermal effects on the cold electrons

$$\frac{\partial^2 \Phi}{\partial x^2} = \frac{e}{\epsilon_0}\left\{ \mathrm{N}_0^h \exp\left(\frac{e\Phi}{\mathrm{T}_e^h}\right) - (\mathrm{Z}_p \mathrm{N}_{0p} - \mathrm{N}_0^c)\right\}, \tag{4.9}$$

where subscript p stands for the protons. For region $x > 0$, the solution of Eq. (4.9) can be calculated as [111]

$$\Phi(x) = -\frac{2\mathrm{T}_e^h}{e}\left\{ ln\left(1 + \frac{x}{\sqrt{2e}\lambda_{De}^h}\right)\right\}, \tag{4.10}$$

where, λ_{De}^h is the Debye length of hot electrons [see Eq. (4.1)]. This potential, $\Phi(x)$ can drive a test proton with initially zero energy at $x = 0$ to an infinite acceleration. Thus, from Eq. (4.6) at larger x, the self-consistent electrostatic potential $\Phi(x)$ must diverge, i.e. as $\Phi \longrightarrow -\infty$ for $x \longrightarrow +\infty$. This is not a consequence of one-dimensional approximation. However, this is directly related to the Boltzmann relation [112], which indicates that the particle with infinite energy can exist, which is impossible in the physical world. This behaviour can be overcome by assuming the electrostatic field becomes zero at $x \longrightarrow +\infty$, and there exists a cut-off energy, $\Phi \longrightarrow -E_{\mathrm{cut}}$ at $x \longrightarrow +\infty$, and the electric field turns to zero at finite distances [113].

TNSA is now the well-understood mechanism for acceleration of ion beams. This acceleration mechanism can produce high-energy ion beams with a high-repetition rate. This mechanism produces the ion beam with an exponential energy spectrum. Most of the application requires not only the good ion beam reproducibility but also the monoenergetic ion beams, which is most challenging and most of the authors try to solve by manipulating the target and laser parameters. The process to produce the monoenergetic beam requires the addition of artificial contamination on the rear surface of the target. This reduces the laser conversion efficiency but allows to produce the low energy-spread ion beams [114–116]. Another problem with this mechanism is limited maximum energy of ions, which is currently achieved. The maximum energy achieved up to date is $\sim 85{-}90$ MeV via TNSA mechanism [117]. On the other hand, radiation therapy requires proton energy up to ~ 300 MeV. Thus substantial progress is needed to achieve the required energy. Another significant challenge is the

energy scaling for the relativistic laser intensities, i.e., $T_e \propto (I\lambda)^2$. Thus, the requirement for laser intensity increases sharply for the production of high-energy ion beams. Thus, to produce the higher-energy beam by TNSA mechanism, one can use either the higher-intensity laser beams with high-repetition rate or use different ion-acceleration scheme which can produce the desired characteristic beams.

4.3 Radiation-Pressure Acceleration

Other system of ion acceleration that has gained attention in the past few years is the radiation-pressure ion acceleration (RPA) [38, 39, 118, 119]. In this mechanism, the ions are accelerated by the laser radiation pressure. In 1966, Marx proposed the principle idea to accelerate any object to the speed of light [120]. Nowadays, this idea is implemented by using the ultra-high-intensity laser interaction with the thin-foil targets, where the entire target is accelerated to very high velocity via laser radiation pressure. In 2004, the theoretical model for RPA had been proposed [40]. In this mechanism, the radiation pressure of the laser accelerates the electrons relativistically and pushes them inside the target. Because of the heavy mass ($m_p = 1836m_e$), the ions cannot keep up the electrons, which points to the development of a strong charge-separation electrostatic field. When the laser intensity is exceptionally high ($I > 10^{23}$ Wcm^{-2}), these electrostatic fields are strong enough to accelerate the ions to relativistic energies within one laser cycle. When the solid target becomes opaque to the laser propagation, i.e., electron density become larger than critical plasma density ($N_e > N_{cr}$), the radiation pressure (P_{Rad}) imposed by the laser pulse on the electron density layer can be given by

$$P_{Rad} = \frac{1}{2}\epsilon_0 E_s^2 = \frac{I}{c}(1 + R - T) = \frac{I}{c}(2R + A), \tag{4.11}$$

where A, R, and T are the absorption, reflection, and transmission coefficients of the target, respectively. These are the function of the wave frequency and refractive index and obtained by using Fresnel's relations [90]. For radiation pressure acceleration to be dominant for linearly polarized laser, it was predicted that a very high intensity $\sim 10^{23}$ Wcm^{-2} is needed, which is not obtainable with the current laser systems. It has been found numerically and experimentally for a linearly polarised laser with an intensity $I > 10^{19}$ Wcm^{-2}, the TNSA mechanism on the rear-side of the surface becomes dominant. This causes more ions to be accelerated from the rear-side of the surface compared to the front side acceleration. Therefore, the acceleration of ions via RPA requires the suppression of hot electrons produced on the front side of the target [121, 122]. The suppression of hot electrons can be achieved by using the normally incident circularly polarised laser. For a normal-incident circularly polarised laser, the requirement for the ultra-high laser intensity is reduced significantly to $\sim 10^{18}$ Wcm^{-2} [38]. Because of the normal incidence, the Brunel and Resonance absorption mechanisms are out of the picture, and the laser pulse is solely absorbed by J×B mechanism [see Chapter 2] which suppresses the hot electrons

and reduces the effect of TNSA mechanism on the rear-side of the target. The experimental work by Palmer et al. [123] have shown that for a mid-IR ($\lambda \simeq 10.4$ μm) CO_2 laser beam, the requirement on the laser intensity could be reduced even further.

Generally, RPA can be classified into two schemes;

1. Hole-boring radiation pressure acceleration scheme (HB-RPA).

2. Light-sail radiation pressure acceleration scheme (LS-RPA).

The thickness of the target can distinguish these two schemes. In the hole-boring RPA, the acceleration of ions happens from unbelievably thick targets. In the beginning, the electrons are piled up, and ions are immobile because of their heavy mass. This results in the charge-separation electrostatic field, which begins to accelerate the ions layer by layer. In HB-RPA, the rear side of the target remains stationary throughout the acceleration process. On the other hand, the LS-RPA scheme deals with the acceleration of the entire thin plasma slab. The electrostatic field is created by the compression and displacement of the electron, which accelerates the ions ballistically with the whole plasma slab. In the next section, we will discuss these two schemes in more details. Both schemes of accelerations are crucial because of their peak-energy scaling with the laser intensity. We will focus more on the hole-boring scheme and try to link it with another acceleration mechanism which occurs via electrostatic collisionless shock.

4.3.1 Hole-Boring RPA: Thick Target

In the first time experimental investigations, it was found that a bunch of ions is accelerated from the front surface of the target [30]. Later on, several experiments have assured that a significant number of ions are accelerated from the front side of the target, and their energy is comparable or even larger than the energy of the ions accelerated from the rear-side of the target [124, 125]. Thus, it becomes essential to examine such a kind of acceleration in more detail.

To determine the velocity of the accelerated ions in the non-relativistic limit, i.e., the velocity of accelerated ions less than the speed of light, the equation of momentum balance need to be solved first. We first consider a high-intensity (I) laser beam is incident on an overdense plasma surface. On the front side of the plasma, the radiation pressure of the laser beam pushes the electrons inside the plasma and piles up the density. Initially, the ponderomotive force pushes the electrons inside the plasma and stacks up to the density, $N_e = N_{p0}$, by leaving behind the immobile ions, as shown in Fig. 4.2(a). This points to the development of the charge-separation electrostatic field, E_x. Because of their heavy mass, the ions are well separated from electrons temporally, and at any time the pondermotive force and the electrostatic field, E_x balance each other. Figure 4.2 designates the simplified electron and ion density profiles, where the electrons are pushed into the plasma and piled up by leaving behind the massive ions. All parameters, N_{p0}, E_x, and x_d are related to each other through charge conservation, Poisson's equation, and pressure balance condition, such as [42]

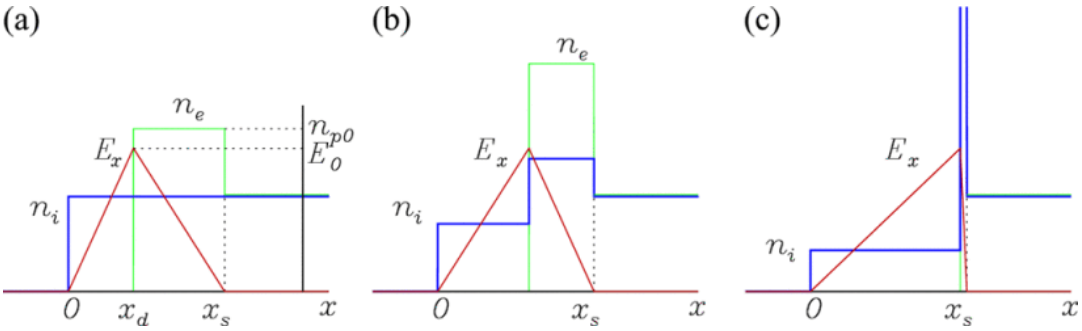


FIGURE 4.2: Graphical illustration of ion density, n_i, electron density, n_e, and electrostatic field, E_x for three different stages of ion acceleration [taken from [126]].

$$\mathrm{P_{Rad}} = \frac{2\mathrm{I}}{\mathrm{c}} = \mathrm{P}_{es} = \int e\mathrm{N}_e\mathbf{E}_x dx. \tag{4.12}$$

The penetration length of the ponderomotive force within the plasma is given by, $\mathrm{l} = \mathrm{c}/2\omega_{pe} = x_s - x_d$. Figure 4.2(c) expresses that the electrostatic force diminishes with the distance, and all ions with initial positions in the range of $x_d < x < x_s$ move to the position $x = x_s$ at the same time, t. These ions transit within the plasma until they face another stationary layer of the ions, and because of the low inertia, the piled up electron layer try to reach an equilibrium with the ions. This process keeps repeating itself until the ions don't reach the rear surface of the target.

In non-relativistic limit, the high-intensity laser interacts with the front-side of the overdense target with mass density, $\mathrm{N}_i\mathrm{m}_i = \frac{\mathrm{A}}{\mathrm{Z}}\mathrm{N}_e\mathrm{m}_p$. The loss rate of the momentum to ions is $\sim 2\mathrm{N}_i\mathrm{m}_i\mathrm{V_{HB}}$. Where $\mathrm{V_{HB}}$ is the velocity of the front surface, which can be approximated by comparing the mass momentum and electromagnetic flow rate given by

$$\mathrm{P_{Rad}} = \frac{2\mathrm{I}}{\mathrm{c}} \sim \frac{2\mathrm{A}}{\mathrm{Z}}\mathrm{N}_e\mathrm{m}_p\mathrm{V}_{\mathrm{HB}}^2. \tag{4.13}$$

At this moment, let's define a dimensionless quantity, Ξ,

$$\Xi = \frac{\mathrm{I}}{\mathrm{N}_i\mathrm{m}_i c^3} = \frac{\mathrm{I}}{\rho c^3} = \frac{\mathrm{Z}}{\mathrm{A}}\frac{\mathrm{N}_{cr}}{\mathrm{N}_e}\frac{\mathrm{m}_e}{\mathrm{m}_p}\mathrm{a}_0^2, \tag{4.14}$$

where ρ is the mass density of the target. And the hole-boring velocity (V_{HB}) can be determined by using Eqs. (4.13) and (4.14)

$$\mathrm{V_{HB}} \sim \left(\frac{\mathrm{I}}{\rho c}\right)^{\frac{1}{2}} = \left(\frac{\mathrm{I}}{\mathrm{N}_i\mathrm{m}_i c}\right)^{\frac{1}{2}} = (\Xi c^2)^{\frac{1}{2}} = c\left(\frac{\mathrm{Z}}{\mathrm{A}}\frac{\mathrm{N}_{cr}}{\mathrm{N}_e}\frac{\mathrm{m}_e}{\mathrm{m}_p}\right)^{\frac{1}{2}} a_0. \tag{4.15}$$

The radiation pressure of the laser accelerates the ions on the front surface layer; these ions penetrate within the overdense plasma and gain a maximum velocity, $\mathrm{V_{max}} = 2\mathrm{V_{HB}}$ [38]. The energy of these accelerated ions per nucleon is given by

$$\mathrm{E_{max}} = 2\mathrm{m}_i\mathrm{V}_{\mathrm{HB}}^2 = 2\mathrm{m}_i c^2\Xi. \tag{4.16}$$

The scaling of the maximum energy with laser intensity is more reliable than $\sqrt{\mathrm{I}}$ scaling for TNSA, which supports that the RPA mechanism is more significant than the TNSA. The dependence of $\mathrm{V_{max}}$ on the laser intensity can be established from Eq. (6.7) and given by

$$\mathrm{V_{max}} = 2\mathrm{V_{HB}} = 2c\sqrt{\Xi}. \tag{4.17}$$

The equation indicates that $\mathrm{V_{max}}$ depends on the target density and the intensity of the laser pulse.

When the hole-boring velocity ($\mathrm{V_{HB}}$) starts approaching the speed of light, c, we have to consider the relativistic factor for the estimation of the $\mathrm{V_{HB}}$. In the lab frame, the Lorentz transformation of laser radiation pressure ($\mathrm{P_{Rad}}$) can be written as

$$\mathrm{P_{Rad}} = \left(\frac{1-\mathrm{V_{HB}}/c}{1+\mathrm{V_{HB}}/c}\right)\frac{2\mathrm{I}}{\mathrm{c}}. \tag{4.18}$$

Similarly, the radiation pressure must be balanced with the loss rate of momentum to the ions given by $(2\gamma_{HB}\mathrm{m}_i\mathrm{V}_{HB})\mathrm{N}_i$, and the relativistic correction to Eq. (4.13) is given by

$$\left(\frac{1-\mathrm{V_{HB}}/c}{1+\mathrm{V_{HB}}/c}\right)\frac{2\mathrm{I}}{\mathrm{c}} \sim (2\gamma_{\mathrm{HB}}\mathrm{m}_i\mathrm{V_{HB}})\mathrm{N}_i, \tag{4.19}$$

where the Lorentz factor, $\gamma_{\mathrm{HB}} = 1/\sqrt{1-\mathrm{V_{HB}^2}/c^2}$. The relativistically corrected $\mathrm{V_{HB}}$ is given by [36, 127]

$$\mathrm{V_{HB}} = \left(\frac{\sqrt{\Xi}}{1+\sqrt{\Xi}}\right)c, \tag{4.20}$$

and the relativistically corrected maximum energy per nucleon of the front-side accelerated ions is given by

$$\mathrm{E_{max}} = 2\mathrm{m}_i c^2\left(\frac{\Xi}{1+2\sqrt{\Xi}}\right). \tag{4.21}$$

Equation (4.20) reveals that for ultra-high laser intensity, the scaling of accelerated ion velocity ($\mathrm{V_{max}}$) turns down to $\sqrt{\mathrm{I}}$. Equations (4.16) and (4.21) indicate the correlation between the energy of the front-side accelerated ions and the intensity of the laser. These results can be utilized for the thick targets, where front-side ions are accelerated. These ions can be accelerated to the $\mathrm{E_{max}}$ as long as the laser and target parameters are constant. Now the question comes into the picture, what happenes if the target is not thick enough? Does the above-described model still work? What happenes if the target will be an order of skin depth of the plasma? To present a summary of all these questions, we further move our studies to another scheme of RPA, known as the **Light-sail RPA**.

4.3.2 Light-sail RPA: Thin Targets

Marx [120] has suggested the idea of light-sail RPA (LS-RPA) based on his predictions of the plane, absolute mirror boosted by a plane wave. The fundamental model of LS-RPA delivers the analytic solution and scaling laws, which emphasize that high efficiency can be achieved in relativistic limit with the present-day laser system and thin target technology. LS-RPA scheme, is induced by laser radiation pressure in a thin target, where the laser radiation pressure can accelerate the whole target. In this regime, the ions are merely accelerated by laser radiation pressure, which is different from HB-RPA.

LS-RPA was first introduced by Esirkepov et al. [40] via three-dimensional numerical simulations. He confirmed that it is possible to accelerate the ions beams to an energy $\sim$ 100 GeV/u by using a laser with intensities, I>10^{23} Wcm^{-2}. Following on, Robinson et al. [118] have extended this work by building a full one-dimensional model for the light-sail regime of RPA.

Let's examine a plasma slab with thickness l_s, ion density N_i, and ion mass m_i. For non-relativistic laser parameters, the gain in the energy can be determined by using the rate of momentum change. The force exerted by the laser pulse on the plasma can be written as

$$\frac{dp}{dt} = A(1+R)\frac{I}{c} = m_i N_i l_s \frac{dV}{dt}. \tag{4.22}$$

The light-sail velocity can be determined by integrating Eq. (4.22),

$$V_{LS} = (1+R)\frac{I}{c}\left(\frac{\tau}{m_i N_i l_s}\right). \tag{4.23}$$

In this regime, the laser pulse pushes both electrons and ions simultaneously. These results are further extended to the relativistic limit by Robinson et al. [118].

The target has to be very thin for this regime. Thus, it is necessary to find the optimum thickness of the target for LS-RPA. The optimum thickness can be obtained by assuming that, the ions are accelerated to the maximum velocity when the electrostatic/thermal pressure of the plasma completely balanced by the laser radiation pressure. This can be accomplished by examining the force between the two plates, $F_C = \frac{\sigma E}{2}$ is comparable to the laser radiation pressure. Here, $\sigma = eN_iL$ is the charge on the plate and $E = \frac{\sigma}{\epsilon_0}$ (*Gauss's law*) is the electric field. Therefore, $F_C = \frac{\sigma^2}{2\epsilon_0} = \frac{e^2 N_i^2 L^2}{2\epsilon_0}$, and by comparing these forces, one can determine the optimum thickness of the target, L

$$L = \left(\frac{2(1+R)\epsilon_0 I}{c e^2 N_i^2}\right)^{\frac{1}{2}}. \tag{4.24}$$

This demands a cold electron population with an assumption that the electron and ions are coupled and move together as a whole target. Another assumption is that there is no transverse component of pondermotive laser acceleration, and pondermotive force scales as $F_p \propto \nabla E$. These assumptions suggest that a

circularly polarized laser is the optimal laser for LS-RPA to accelerates the ion efficiently.

The above outcomes designate that, if the target does not meet the optimum requirement, there will be an increase in the mass. This means a balance between the charge-separation field and laser radiation pressure cannot be reached, which results in the decoupling of electrons and ions. This causes a decrease in the efficiency of the accelerating ions.

The above-described model is based on the one-dimensional assumption, where a supergaussian laser profile is used. Nevertheless, this model gives the possibility of producing monoenergetic ion beams with favourable peak energy scaling. LS-RPA relies on the suppression of hot electrons, although in reality, it is challenging to obtain such a laser pulse. Consequently, the target deformation and spatially varying laser intensity begin to suppress ion acceleration. This model additionally faces the difficulty with Rayleigh-Taylor [128] and Weibel-like [129] instabilities.

4.4 Collisionless Shock Ion Acceleration

The collisionless shocks are universal in the diverse astrophysical environment such as pulsar wind nebulae, supernova remnants, the Earth's bow shock, etc. These shocks are thought to be accountable for particle acceleration and the generation of cosmic rays [130, 131]. The astonishing growth in the development of high-power and high-intensity lasers has made it feasible to recreate the appropriate conditions to study the formation and evolution of collisionless shocks in the laboratory. These laser-driven electrostatic collisionless shock can be utilized as a high-energy compact particle accelerator [42, 43, 125, 132, 133]. To accelerated ions by collisionless shock acceleration (CSA) mechanism, the potential energy at the shock front must be larger than kinetic energy of the upstream expanding ions in the shock rest frame [41]. Thus, the ions, which is initially at rest and located ahead of the shock front, get accelerated to the twice of the shock velocity, i.e., $V_r = 2V_{sh}$. Here, V_{sh} and V_r represent the shock velocity and the velocity of shock-reflected ions, respectively. The interaction of strong laser pulse with the overdense [61] and underdense plasmas produced by the long prepulse in solid targets [125], in gas-jets [132] leads to the formation of collisionless shock in the laboratory. At the beginning of the 1970s, a low Mach-number collisionless shock has been demonstrated in the laboratory [134]. Earlier, the theoretical and numerical investigation concludes the generation of a high Mach-number collisionless shock in laser-plasma interactions [135].

Currently, laser-driven collisionless shock ion accelerations mechanism has become the most attractive contender and starts receiving most of the attractions. This is because of the production of high-quality ion beams; in other words, the energy spectrum of the reflected ions is theoretically monoenergetic, which is very beneficial for most of the practical applications. In the laboratory, the ion acceleration via CSA mechanism has been reported by the interaction of laser pulse with gas-jet targets [49], underdense [132] and overdense plasmas [61].

Initially, the particle-in-cell simulations performed by Denavit [42] confers the ion acceleration via CSA mechanism. Later on, Silva [43] has showed the formation of an electrostatic collisionless shock with Mach numbers, M = 2−3. In these investigations, an ultra-high intensity laser (I $\geq 10^{21}$ Wcm^{-2}) is needed to heat the electrons in the solid target efficiently. The shock is formed on the front surface of the target and propagates with a velocity nearly equivalent to the hole-boring velocity, i.e., $V_{sh} \simeq V_{HB}$. In these simulations, the acceleration of ions from the front side of the target is smeared out by the strong charge-separation electrostatic field at the plasma-vacuum interface on the rear-side of the target. Laser-solid interaction in the laboratory renders the evidence of front-side ion acceleration contribution with respect to TNSA acceleration on the rear-side of the target observed in the experiment [124]. The numerical simulations have been done by d'Humieres [133], and Chen [136] has represented the interplay between the ion acceleration via CSA and TNSA mechanisms. A comprehensive theoretical and numerical investigation on CSA was complemented by Fiuza [46]. These studies imply that a specially tailored near-critical density profile is essential to constrain the sheath TNSA electrostatic field at the plasma-vacuum interface. An exponential density gradient on the rear-side of the target provides the optimal condition for CSA [45]. An exponential density gradient diminishes the strong TNSA field to a small and constant amplitude; this sheath field leads to a continuous power-law ion spectrum. Suppression of TNSA sheath field results in quasi-monoenergetic ion beams [137]. The influence of the density gradient on the rear-side of the target has been optimized numerically [138]. Recently, CSA has been demonstrated in the laboratory using 10 μm wavelength CO_2 laser with an intensity 6.5×10^{16} Wcm^{-2} and a near-critical density gas target [49]. This produces a 20 MeV quasi-monoenergetic proton beam with a flux 10^7 protons/MeV/Sr. CSA has been extended to the under-critical density targets; acknowledged as the low-density CSA (LDCSA) [139]. A 45 MeV proton beam with a broad energy spectrum has been obtained in the laboratory via LDCSA [50]. Very recently, the acceleration of protons and C^{6+} ions via CSA mechanism has been achieved by utilizing the interaction of a laser pulse (10^{20} Wcm^{-2}) with a laser ablated near-critical density plasma [51]. Several experiments and numerical simulations have been carried out over the last few years to understand and characterize ion acceleration via CSA mechanism. One aspect, i.e., the influence of different target materials on CSA remains the open question for studies. In this thesis, we report on the numerical investigation of electrostatic collisionless shock formation and influence of different materials on the shock-accelerated proton beams.

Among all these ion acceleration mechanisms, CSA has become an attractive candidate for the acceleration of high-quality ion beams. Ions accelerated via CSA mechanism have the advantage of low-divergence and monoenergetic beams. The energy of the accelerated ions via CSA mechanism is more desirable than the TNSA mechanism. The accelerated ion energy for CSA mechanism is scaled linearly with laser intensity [45], while it scales as the square-root for TNSA [140]. Alternative acceleration schemes, such as radiation-pressure acceleration that can achieve monoenergetic and higher energy which is suitable for applications, impose strict and challenging conditions in experiments, such as

the target thickness and laser contrast [141, 142]. The interaction of laser with solids in the TNSA and RPA regimes produces the debris in the target chamber. The use of gas-jet targets for CSA would make the operation significantly easier for high-repetition rate laser facilities [49]. In addition, the requirement for near-critical density plasmas reduces the debris in the chamber. Numerical simulations indicate that the high-energy ion beam with a narrow energy spread can be produced through CSA mechanism [45]. However, despite all these advantages, there are still some limitations that need to be solved such as ion flux, energy, energy spread, laser to ion conversion efficiency, the stability of acceleration parameters, etc.

In this thesis, we report on the numerical investigation of electrostatic collisionless shock formation and influence of different material on the shock-accelerated ion beams.

Chapter 5

Theory of Collisionless Shock Ion Acceleration

5.1 Collisionless Shock

A shock wave can be characterized as a discontinuous transition layer that exists within the unshocked (upstream) and the shocked (downstream) regions, which is also known as a ramp. The shock waves are universal in the astrophysical environment. Shock waves exist in both media, i.e., collisionless medium such as interstellar, and collisional medium such as the atmosphere. The flow velocity across this shock undergo discontinuous change, which follows a variation in the bulk kinetic energy through the ramp. This change in the flow velocity thought to be the source of free energy, which requires to be dissipated to maintain the conservation of energy. It is well understood that for a collisional shock wave, the origin of dissipation is the binary collisions. The average kinetic energy of the system is increased by these binary collisions, which results in heating. Moreover, these binary collisions point to an increase in the entropy of the system. Consequently, the shock transition is an irreversible process. However, dissipation in a shock wave in the astrophysical environment cannot depend on the binary collisions [143], it depends on the wave-particle interactions [144]. The source of the collisionless shock wave in the astrophysical environment is attached to some energetic and most powerful systems; such as supernova remnants (SNRs), Gamma-Ray Bursts (GRBs), etc. These collisionless shocks are believed to be the origin of non-thermal particles (cosmic rays) and high energy radiations (GRBs). [145]. In the next section, we will describe the conservation laws (Rankine-Hugoniot relation) for a collisionless shock.

5.1.1 Conservation Laws

In fluid dynamics, it is necessary that any discontinuous transition within the two plasma states (upstream and downstream) must follow the conservation laws, such as conservation of mass, energy, and momentum. The integration of mass continuity equation over some shock transition volume results in the conservation of mass. Equation of continuity is a solution to the Boltzmann equation of the form

$$\frac{\partial f}{\partial t} + \mathbf{u} \cdot \nabla f + \frac{\mathbf{F}}{\mathrm{m}} . \nabla_u f = \frac{\delta_c f}{\delta t}, \tag{5.1}$$

where $\mathbf{F}$ is the external force, ∇_u is the gradient in the velocity space, $f = f(\mathbf{x}, \mathbf{u}, t)$ is the distribution function, and $\delta_c/\delta t$ is the collisional operator. For a collisionless plasma, $\delta_c/\delta t \to 0$, and Eq. (5.1) changes into the Vlasov equation. In a space volume element $d^3x d^3u$, the number of particles, dN can be given by

$$d\mathrm{N} = f(\mathbf{x}, \mathbf{u}, t) d^3x d^3u. \tag{5.2}$$

Let's consider that the distribution function $f = f(\mathbf{x}, \mathbf{u}, t)$ is continuous function of space $\mathbf{x}$ and velocity $\mathbf{u}$. In other words, the volume element $d^3x d^3u$ contains a sufficiently large number of particles, so that the discrete particles can not describe the system. As a result, integration of $f = f(\mathbf{x},\mathbf{u},t)$ all over the phase space will give the total number of particles in the system. For simplicity, let's define some quantities, which we will use later in this section

$$\mathrm{N}_r = \int_{vel} f_r(\mathbf{x}, \mathbf{u}, t) d^3u, \tag{5.3}$$

$$\mathbf{V}_r = \frac{1}{\mathrm{N}_r} \int_{vel} \mathbf{u} f_r(\mathbf{x}, \mathbf{u}, t) d^3u, \tag{5.4}$$

$$\mathrm{KE}_r = \frac{\mathrm{m}_r}{2} \int_{vel} u^2 f_r(\mathbf{x}, \mathbf{u}, t) d^3u, \tag{5.5}$$

$$\overleftrightarrow{\mathbf{P}}_r = \mathrm{m}_r \int_{vel} (\mathbf{u} - \mathbf{V}_r)(\mathbf{u} - \mathbf{V}_r) f_r(\mathbf{x}, \mathbf{u}, t) d^3u, \tag{5.6}$$

where N_r, m_r, $\mathbf{V}_r$, and KE_r are the number density, mass, average velocity, and the kinetic energy density of species r, respectively. Here, $\overleftrightarrow{\mathbf{P}}_r$ is the pressure tensor term [146]. The integration of the Vlasov equation multiplied by velocity across the velocity space results in an equation of moment. As we explained earlier, the solution of moment equation gives the continuity equation,

$$\frac{\partial \rho_m}{\partial t} + \nabla \cdot (\rho_m \mathbf{V}_r) = 0. \tag{5.7}$$

Here, ρ_m is the mass density, which is characterized by the multiplication of number density, Eq. (5.3) with particle mass, and $\mathbf{V}_r$ is the bulk flow velocity, Eq. (5.4). The conservation of mass, i.e., mass cannot be created or destroyed in the discontinuity, gives Eq. (5.7). The equation of momentum conservation can be accomplished by applying some assumptions to the Vlasov equation. The momentum conservation can be given by

$$\mathrm{m}_r \mathrm{N}_r \left\{ \frac{\partial \mathbf{V}_r}{\partial t} + (\mathbf{V}_r \cdot \nabla)\mathbf{V}_r \right\} = \mathrm{N}_r \mathbf{F} - \Delta \cdot \overleftrightarrow{\mathbf{P}}_r, \tag{5.8}$$

where, $\mathbf{F}$ is the Lorentz force, given by $\mathbf{F} = \mathrm{e}_r[\mathbf{E} + \mathbf{u} \times \mathbf{B}]$.

In magnetohydrodynamic fluid, the component of the electric and magnetic fields has to be involved in the conservation relations. Thus, the conservation of momentum and energy can be given by

$$\frac{\partial(\rho_m \mathbf{V}_r)}{\partial t} + \nabla \cdot \left\{ \rho_m (\mathbf{V}_r \mathbf{V}_r) + \left(\mathrm{P} + \frac{\mathrm{B}^2}{2\mu_0} \right) \overleftrightarrow{\mathbf{I}} - \frac{\mathbf{BB}}{\mu_0} \right\} = 0, \tag{5.9}$$

$$\frac{\partial}{\partial t}\left(\frac{1}{2}\rho_m \mathrm{V}_r^2 + \frac{\mathrm{P}_r}{\gamma-1} + \frac{\mathrm{B}^2}{2\mu_0}\right) + \nabla\cdot\left\{\frac{1}{2}\rho_m \mathrm{V}_r^2\mathbf{V}_r + \left(\frac{\gamma \mathrm{P}_r}{\gamma-1}\right)\mathbf{V}_r + \frac{\mathbf{E}\times\mathbf{B}}{\mu_0}\right\} = 0. \tag{5.10}$$

Here, P stands for the scaler pressure term, and $\gamma = 1 + 2/d_f$ is the statistical parameter, d_f is the degree of freedom. For one, two and three dimensional gases, i.e., $d_f = 1$, 2, and 3 result in $\gamma = 3$, 2, and 5/3, respectively. For an isothermal gas, $\gamma = 1$ and for incompressible gas $\gamma = \infty$ [146].

In the following, the brackets [ ] define the difference between the downstream and upstream quantities across the shock, then the relations establish the conservation laws, known as the Rankine-Hugoniot relations [146], which is given by as follow

$$[\rho_m \mathrm{V}_n] = 0, \tag{5.11}$$

$$\left[(\rho_m \mathrm{V}_n)\mathbf{V}_t - \frac{\mathrm{B}_n\mathbf{B}_t}{\mu_0}\right] = 0, \tag{5.12}$$

$$\left[\rho_m \mathrm{V}_n^2 + \mathrm{P} + \frac{\mathrm{B}_t^2}{2\mu_0}\right] = 0, \tag{5.13}$$

$$\left[\left(\frac{1}{2}\rho_m \mathrm{V}^2 + \frac{\gamma \mathrm{P}}{\gamma-1} + \frac{\mathrm{B}^2}{\mu_0}\right)\mathrm{V}_n - (\mathbf{V}\cdot\mathbf{B})\frac{\mathrm{B}_n}{\mu_0}\right] = 0, \tag{5.14}$$

$$[\mathrm{V}_n(\hat{\mathbf{n}}\times\mathbf{B}_t) + (\mathbf{V}_t\times\hat{\mathbf{n}})\mathrm{B}_n] = 0, \tag{5.15}$$

$$[\hat{\mathbf{n}}\cdot\mathbf{B}] = 0. \tag{5.16}$$

Here, t and n indicate the tangential and normal momentum directions, respectively and $\hat{\mathbf{n}}$ is the shock normal vector. Equation (5.11), signifies the continuity of mass, Eqs. (5.12) and (5.13) outline the tangential and normal momentum, respectively. Equation (5.14) is the energy conservation law and the last two Eqs. (5.15) and (5.16) indicate Maxwell's relations. One can define the relevant shock parameters by using Eqs. (5.11-5.16) [147]. It would be wrong to use only adiabatic equations to describe the shock transition. This is because an abrupt change in the quantities occurs through the shock transition, which results in the irreversible nature of the shock. The Rankine-Hugoniot relations explain these values far away from the shock, not in the dissipative regions. Consequently, some of the kinetic energy get transformed in some other form through the shock transitions, and it will not be conserved. The transformations of kinetic energy in some other states causes shock irreversibility and increases entropy.

The collisionless shock is thought to be one of the fundamental mechanism to accelerates or heat the charged particles. As the name suggests, there are no binary collisions present in the system. Therefore, it is interesting to determine the dissipation mechanism for a collisionless shock. Some of the possible dissipation mechanisms are the wave dispersion [148], anomalous resistivity due to wave-particle interactions [144], and particle reflections [149], etc. In this thesis, we will concentrate on the dissipation of collisionless shock through particle reflection. To understand the particle acceleration in collisionless shock, first we will go through the some of the essential characteristics, that would be helpful to understand the particle acceleration by collisionless shock.

5.2 Ion Acoustic Wave in Plasma

The ion-acoustic waves are excited in the electron-ion plasmas, when the motion of the ions cannot be neglected compared to the thermal movement of the electrons. The frequency of these ion-acoustic waves is much smaller than the electron plasma frequency. Thus, all ions are bound to the electrons by electrostatic forces, which leads to charge neutrality in the plasma. For Z = 1, when the charge neutrality of the plasma satisfied, i.e., $N_e \simeq N_i = N$, no need to apply the Poisson's equations for these oscillations. For warm, homogeneous, collisionless, unmagnetized plasmas, we will use ion momentum and continuity equations to explore these oscillations. By using all these conditions, the equation of ion momentum is presented by [87]

$$m_i N_i \left[\frac{\partial \mathbf{u}_i}{\partial t} + (\mathbf{u}_i \cdot \nabla)\mathbf{u}_i\right] = Ze N_i \mathbf{E} - \nabla p_i. \tag{5.17}$$

The simple plane wave can be described in a form, exp$i$($\mathbf{k}$·$\mathbf{r}$ - ωt). Here the electrostatic field ($\mathbf{E}$) can be written in form potential (Φ), i.e. $\mathbf{E}$ = -$\nabla\Phi$ = -$i\mathbf{k}\Phi$. Similarly from the fluid description of the plasma, the ion pressure term can be written in term of the ion density

$$-\nabla p_i = -\gamma_i k_B T_i \nabla N_i = -\gamma_i k_B T_i i\mathbf{k} N_i, \tag{5.18}$$

where $\gamma_i = c_p/c_v$ is the ratio of specific gravity at constant pressure and volume. Afterward applying the linearization and imposing the oscillatory solution, the equation of ion momentum can be written as

$$-i\omega N_0 m_i \mathbf{u}_1 = -eN_0 i\mathbf{k}\Phi_1 - \gamma_i k_B T_i i\mathbf{k} N_1. \tag{5.19}$$

The density of electrons (N_e) with a temperature T_e quickly respond to potential Φ_1, try to maintain the equilibrium, and will follow the Boltzmann distribution

$$N_e = N_0 \exp\left(\frac{e\Phi}{k_B T_e}\right) \simeq N_0\left(1 + \frac{e\Phi_1}{k_B T_e} + ...\right). \tag{5.20}$$

Since $N_e = N_i$, from the above equations one can conclude that first order density perturbation can be written as

$$N_1 = N_0\left(\frac{e\Phi_1}{k_B T_e}\right). \tag{5.21}$$

Similarly, the linearization of the continuity equation for ion fluid gives

$$\frac{\partial N_i}{\partial t} + \nabla \cdot (N_i \mathbf{u}_i) = 0 \Longrightarrow -i\omega N_1 = -N_0 i\mathbf{k} \cdot \mathbf{u}_i. \tag{5.22}$$

The above Eqs. (5.18), (5.21), and (5.22) indicate the homogeneous system of the three variables N_1, $\mathbf{u}_1$, and Φ_1. The dispersion relation for the ion acoustic

wave can be obtained by solving these three equations,

$$\omega^2 = \left(\frac{k_B \mathrm{T}_e + \gamma_i k_B \mathrm{T}_i}{\mathrm{m}_i}\right) k^2. \tag{5.23}$$

Because of the light mass of the electrons compared to the ion mass, $\mathrm{m}_e << \mathrm{m}_i$, the electrons can propagate through many wavelengths in a single period of a plane wave. Thus, the distribution of electrons can be considered isothermal. For a 1-dimensional case, the compression of ions in the plane wave results in the specific heat ratio for ions $\gamma_i = 3$. By applying these conditions to the above equation, we obtain

$$\mathrm{C}_s = \frac{\omega}{k} = \left(\frac{k_B \mathrm{T}_e + 3 k_B \mathrm{T}_i}{\mathrm{m}_i}\right)^{\frac{1}{2}}. \tag{5.24}$$

Here C_s is the ion sound speed in the plasma. It is clear from Eq. (5.24), for an ion-acoustic wave, both the phase velocity (V_{ph}) and the group velocity (V_g) will be equal to the C_s.

To characterize the dispersion relation of ion-acoustic wave in a more sophisticated way, one must include the description of Poisson's equations to couple the local plasma density (electrons N_{e1} and ions N_{i1}, and the potential Φ). The linearised set of continuity, momentum, and Poisson's equations can be written as

$$-i\omega \mathrm{N}_{i1} = -\mathrm{N}_0 i\mathbf{k} \cdot \mathbf{u}_i, \tag{5.25}$$

$$-i\omega \mathrm{N}_0 \mathrm{m}_i \mathbf{u}_i = -e n_0 i\mathbf{k}\Phi_1 - \gamma_i k_B \mathrm{T}_i i\mathbf{k}\mathrm{N}_{i1}, \tag{5.26}$$

$$\frac{\partial^2 \Phi_1}{\partial x^2} = \frac{\mathrm{q}}{\epsilon_0}(\mathrm{N}_{i1} - \mathrm{N}_{e1}). \tag{5.27}$$

The density of electrons can be given by linearized Boltzmann relation, i.e. Eq. (5.20) and the ion density can calculated from the continuity equations. So,

$$\mathrm{N}_{e1} = \mathrm{N}_0 \left(\frac{e\Phi_1}{k_B \mathrm{T}_e}\right), \tag{5.28}$$

$$\mathrm{N}_{i1} = \left(\frac{k}{\omega}\right) \mathrm{N}_0 \mathrm{u}_i. \tag{5.29}$$

The values in the above equations provide a more accurate solution for the ion acoustic wave dispersion relations

$$\frac{\omega}{k} = \sqrt{\left(\frac{k_B \mathrm{T}_e}{\mathrm{m}_i} \frac{1}{1 + k^2 \lambda_{De}^2} + 3\frac{k_B \mathrm{T}_i}{\mathrm{m}_i}\right)}. \tag{5.30}$$

For $\mathrm{T}_i << \mathrm{T}_e$, the ion pressure term, T_i can be ignored, and the electron pressure term only provides the restoring force to the wave. When the wavelength of the wave becomes the order of the Debye-length, i.e., $k\lambda_{De} \sim 1$, the character of the ion acoustic wave is modified. By using all these conditions, the above

equations can be rewritten as

$$\mathrm{C}_s = \frac{\omega}{k} = \sqrt{\left(\frac{k_B \mathrm{T}_e}{\mathrm{m}_i} \frac{1}{1 + k^2 \lambda_{De}^2}\right)}. \tag{5.31}$$

This implies for $k^2\lambda_{De}^2 >> 1$, the frequency of the ion-acoustic wave becomes comparable to the ion plasma frequency, i.e. $\omega_{pi} \simeq \omega_{pe}\sqrt{\mathrm{m}_e/\mathrm{m}_i} \equiv \sqrt{\mathrm{N}_i q^2/\epsilon_0 \mathrm{m}_i}$, where ω_{pe} is electron plasma frequency. It can be seen from Eqs. (5.30) and (5.31), for high frequencies or a short wavelength, the ion acoustic wave becomes a constant frequency wave. Therefore, there is a complementary operation between Langmuir waves and ion acoustic waves: the former are basically constant frequency but become constant velocity at large k, while the latter are basically constant velocity but become constant frequency at large k.

5.3 Ion Acoustic Solitons

The theoretical analysis of the ion-acoustic solitons can be applied to the ion-acoustic shock waves. The Sagdeev formalism [150] is employed to conclude the theory of electrostatic collisionless shock waves in plasma [41, 87].

Consider a soliton wave is traveling with a velocity, V_i with respect to the unperturbed plasma as shown in Fig. 5.1. Plasma composed of cold ions and hot electrons. The velocity of this wave, V_i, is much smaller than the thermal velocity of electrons, $\mathrm{V}_{th} = \sqrt{k_B \mathrm{T}_e/\mathrm{m}_e}$, i.e. $\mathrm{V}_i << \mathrm{V}_{th}$. The equation of

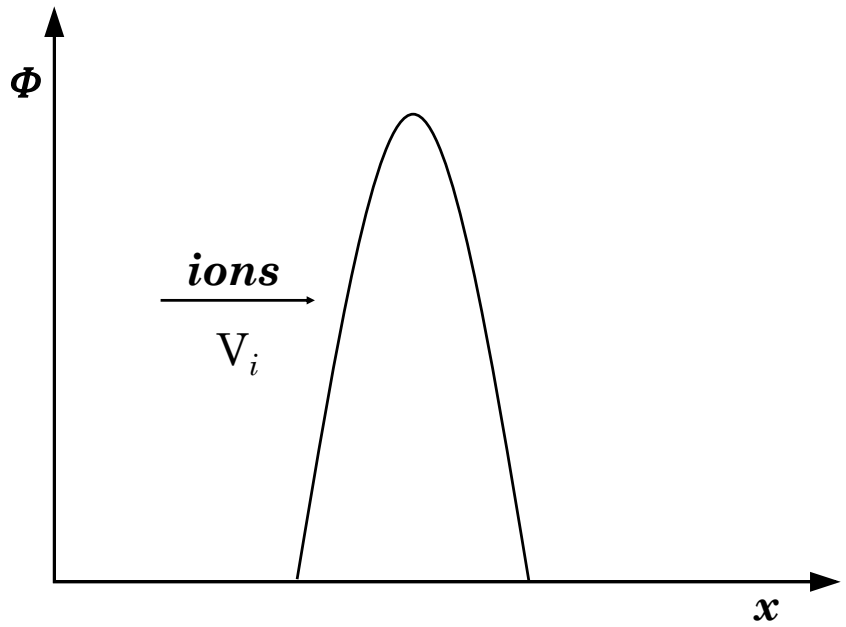


FIGURE 5.1: Schematic description of a soliton wave. Electrons are always considered in equilibrium and cold ions are moving to the right in the soliton rest frame [taken from [87]].

continuity and momentum for ion fluid is presented by

$$\frac{\partial \mathrm{N}_i}{\partial t} + \frac{\partial(\mathrm{N}_i \mathrm{V}_i)}{\partial x} = 0, \tag{5.32}$$

$$\frac{\partial \mathrm{V}_i}{\partial t} + \mathrm{V}_i \frac{\partial \mathrm{V}_i}{\partial x} = -\frac{e}{\mathrm{m}_i} \frac{\partial \Phi}{\partial x}. \tag{5.33}$$

If we view ourself in the frame of reference with this wave, the potential, $\Phi(x)$ will be constant in time, and we will witness that a bunch of ions will be approaching the wave with the same velocity V_i. Consequently, all quantities are fixed in time, and by applying $\partial/\partial t = 0$ in the above equations, and utilizing the laws of conservation, we obtain $1/2\mathrm{m}_i\mathrm{V}_i^2 + \mathrm{e}\Phi = 1/2\mathrm{m}_i\mathrm{V}_{i0}^2$, and $\mathrm{N}_i\mathrm{V}_i = \mathrm{N}_0\mathrm{V}_{i0}$, where $\mathrm{N}_i(-\infty) = \mathrm{N}_0$ and $\mathrm{V}_i(-\infty) = \mathrm{V}_{i0}$. So, the velocity these ions, V_i, and density N_i in the term of the electrostatic potential, Φ can be written as

$$\mathrm{V}_i = \left(\mathrm{V}_{i0}^2 - \frac{2e\Phi}{\mathrm{m}_i}\right)^{\frac{1}{2}}, \tag{5.34}$$

$$\mathrm{N}_i = \mathrm{N}_0 \left(1 - \frac{2e\Phi}{\mathrm{m}_i \mathrm{V}_{i0}^2}\right)^{-\frac{1}{2}}. \tag{5.35}$$

Here, N_0 is the unperturbed ion plasma density. Electrons are assumed to be Maxwellian distribution, and electron density can be given by the Boltzmann relation (Eq. (5.20)). Therefore, Poisson's equation can be written as

$$\frac{\mathrm{d}^2\Phi}{\mathrm{d}x^2} = \frac{e}{\epsilon_0}(\mathrm{N}_e - \mathrm{N}_i) = \frac{e}{\epsilon_0}\mathrm{N}_0 \left\{ \exp\left(\frac{e\Phi}{k_B \mathrm{T}_e}\right) - \left(1 - \frac{2e\Phi}{\mathrm{m}_i \mathrm{V}_{i0}^2}\right)^{-\frac{1}{2}} \right\}. \tag{5.36}$$

To simplify the above equation, we introduce some quantities, such as

$$\lambda_{De} = \left(\frac{\epsilon_0 k_B \mathrm{T}_e}{\mathrm{N}_e e^2}\right)^{\frac{1}{2}}, \tag{5.37}$$

$$\mathrm{C}_s = \left(\frac{k_B \mathrm{T}_e}{\mathrm{m}_i}\right)^{\frac{1}{2}}, \tag{5.38}$$

$$\phi = \frac{e\Phi}{k_B \mathrm{T}_e}, \tag{5.39}$$

$$\mathrm{X} = \frac{x}{\lambda_{De}}, \tag{5.40}$$

$$\mathrm{M} = \frac{\mathrm{V}_{i0}}{\mathrm{C}_s}. \tag{5.41}$$

Here, C_s is the ion-acoustic velocity, and M is the Mach number for the shock. By using all these values in Eq. (5.36), the Poisson's equation can be written as

$$\frac{\mathrm{d}^2\phi}{\mathrm{dX}^2} = -\frac{\mathrm{d}\Psi}{\mathrm{d}\phi}, \tag{5.42}$$

with the right-hand side described as

$$\frac{\mathrm{d}\Psi}{\mathrm{d}\phi} = \exp(\phi) - \left(1 - \frac{2e\phi}{\mathrm{M}^2}\right)^{-\frac{1}{2}}. \tag{5.43}$$

Here, Ψ is known as the Sagdeev potential. Sagdeev used an oscillator in a potential well analogy with an equation of motion for the harmonic oscillator

$$\mathrm{M}\frac{\mathrm{d}^2\mathrm{X}}{\mathrm{d}t^2} + \frac{\mathrm{dV}}{\mathrm{dX}} = 0. \tag{5.44}$$

The above Eq. (5.42) is similar to Eq. (5.44), where the kinetic energy term $\frac{\mathrm{d}^2\phi}{\mathrm{dX}^2}$ is balanced by the potential energy Ψ. By integrating Eq. (5.42) in term of the energy integral, we can get

$$\frac{1}{2}\left(\frac{\mathrm{d}\phi}{\mathrm{dX}}\right)^2 + \Psi(\phi, \mathrm{M}) = 0. \tag{5.45}$$

Here, the function $\Psi(\phi, \mathrm{M})$ describes the pseudo-potential energy, which can be given by

$$\Psi(\phi, \mathrm{M}) = 1 - \exp(\phi) + \mathrm{M}^2\left(1 - \sqrt{1 - \frac{2\phi}{\mathrm{M}^2}}\right). \tag{5.46}$$

The pseudo-potential $\Psi(\phi, \mathrm{M})$ can be plotted for a given value of Mach number, as shown in Fig. 5.2. Assuming no dissipation, consider a particle will move from $\phi = 0$ to some positive values of ϕ before returning to its initial position. This behaviour is know as 'Soliton', a potential or density disturbance travelling with velocity, V_i as shown in Fig. 5.1. The initial state of the medium is restored after the passing of the soliton. The soliton-like solution exists for a specific

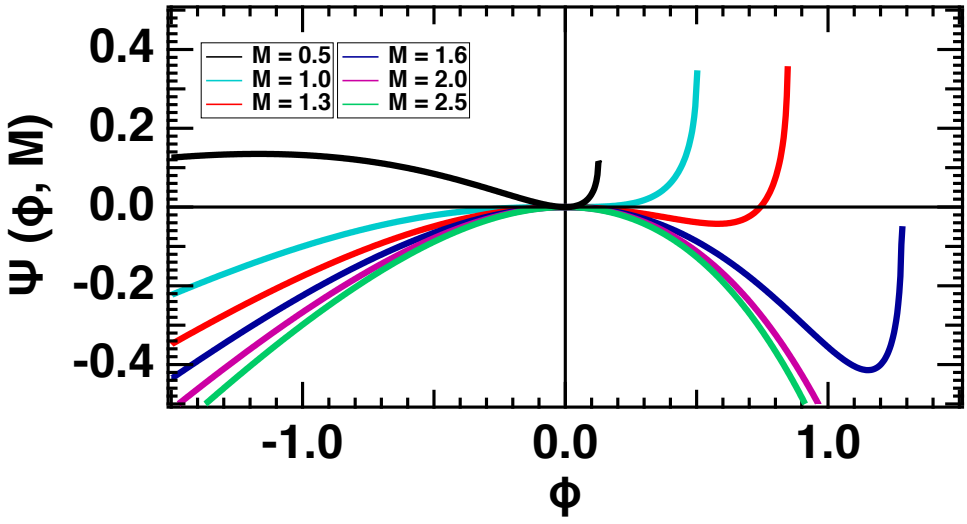


FIGURE 5.2: Sagdeev potential as function of electrostatic potential, ϕ. Solitary structure for a couple of Mach numbers.

range of Mach number as shown in Fig. 5.2. The lower limit of Mach number arises due to the condition of potential well, which is determined by Eq. (5.46) as $\Psi(\phi, \mathrm{M}) < 0$ for $\phi << 1$

$$\Psi(\phi, \mathrm{M}) \simeq -\frac{\phi^2}{2} + \frac{\phi^2}{2\mathrm{M}^2} < 0. \tag{5.47}$$

This gives the lower limit

$$\mathrm{M} > 1. \tag{5.48}$$

The M>1 is required for the existence of the soliton, i.e., a soliton has to be supersonic. Additional considerations for these solutions have shown that neither the double layer nor the negative potential exists, although the ion densities have to be determined by Eq. (5.35) for the physical requirements. As $\mathrm{N}_i \longrightarrow \infty$ for potential $\phi = \mathrm{M}^2/2$, the only possible values of M are those for which a finite root of ϕ_m is obtained before reaching the infinite compression of density, N_i. So, the condition on potential, $\phi = \mathrm{M}^2/2$ gives the maximum possible value of Mach number, M_{cr}. By using these values in Eq. (5.46)

$$\Psi(\phi = \mathrm{M}^2/2) = 1 + \mathrm{M}^2 - \exp\left(\frac{\mathrm{M}^2}{2}\right) > 0. \tag{5.49}$$

By using the numerical calculations, the maximum possible Mach number comes out to be

$$\mathrm{M}_{cr} < 1.585. \tag{5.50}$$

Figure 5.2(a) shows a range of the electrostatic potential for which a large amplitude solitary wave can exist for various Mach numbers. As the Mach number and potential increase, the depth of the potential-well becomes deeper and deeper. The $\phi_m = \mathrm{M}^2/2 \approx 1.3$ gives the critical amplitude of the solitary wave. Thus, in a cold ion plasma for potential, $0 < \phi < 1.3$ and Mach number, $1 < \mathrm{M} < 1.585$ roughly an ion-acoustic solitary waves can exist. For value, M>1.6, the potential well is not formed, which means the solitary wave solution changes into a shock wave solution. All particles with kinetic energy less than the potential energy at the soliton/shock front, i.e., $\frac{1}{2}\mathrm{m}_i\mathrm{V}_i^2 < e\phi$, will be reflected. On the other hand, if the kinetic energy is larger than the potential energy, all these particles will be transmitted through the soliton. Although the ion reflection condition changes when kinetic effects are included. Then the low energy particles in the distribution function may become reflected in a continuous form from the soliton potential, and asymmetry arises more naturally.

5.4 Particle Reflection

The processes of forming electrostatic collisionless shock and their succeeding ion acceleration play important roles in plasma physics. The perturbed state of density represents the solitary wave in the plasma, and the ion reflection thought to be one of the dissipation mechanisms for the solitary wave. To our knowledge, the particle reflection is one of the requirements for supercritical

(M>1) collisionless shock. To brief the compensation of momentum and energy flowing into the shock front, the ion reflection is only possible dissipative mechanism inside the shock ramp. We further extend our study to provide the existence of shock front in the ion-acoustic case. By rewriting Eq. (5.36) in term of pseudo-potential, $\Psi(\phi)$, it turns into [41, 151]

$$\frac{\mathrm{d}^2\phi}{\mathrm{d}x^2} = -\frac{\mathrm{d}\Psi(\phi)}{\mathrm{dX}} = \frac{e\mathrm{N}_0}{\epsilon_0}\left\{\exp\left(\frac{e\phi}{k_B\mathrm{T}_e}\right) - \mathrm{V}_{i0}\left(\mathrm{V}_{i0}^2 - \frac{2e\phi}{\mathrm{m}_i}\right)^{-\frac{1}{2}}\right\}. \tag{5.51}$$

If the ion reflection is negligible, the above equation determines the potential profile, ϕ for ion-acoustic wave. The pseudo-potential can be calculated by integrating Eq. (5.51) in term of the propagation velocity, V_{i0} and unperturbed density, N_0

$$\Psi(\phi) = -\frac{\mathrm{N}_0}{\epsilon_0}\left\{k_B\mathrm{T}_e\exp\left(\frac{e\phi}{k_B\mathrm{T}_e}\right) + \mathrm{m}_i\mathrm{V}_{i0}\left(\mathrm{V}_{i0}^2 - \frac{2e\phi}{\mathrm{m}_i}\right)^{\frac{1}{2}}\right\} + \mathrm{C}. \tag{5.52}$$

Depending on the nature of the integration constant, C, various solutions for the periodic wave can be obtained. For a particular case, when $\phi = 0$ results in all quantities, $\frac{\mathrm{d}\Psi}{\mathrm{d}\phi}$, $\frac{\mathrm{d}\phi}{\mathrm{dX}}$, and $\Psi(\phi)$ to be zero, which gives a positive value of

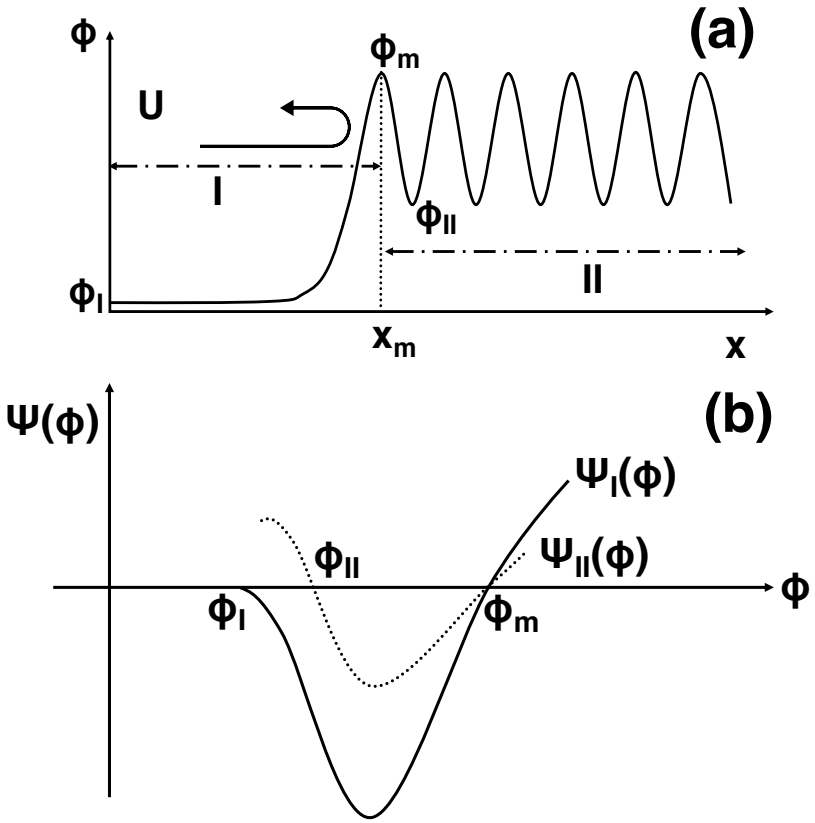


FIGURE 5.3: (a) An oscillatory electrostatic collisionless shock transition with some reflected ions from the front edge. (b) Potential Ψ_{I} and Ψ_{II} for regions I and II for an electrostatic shock [taken from [41]].

C. By using all these values in Eq. (5.52)

$$\mathrm{C} = -\frac{\mathrm{N}_0}{\epsilon_0}(k_B \mathrm{T}_e + \mathrm{m}_i \mathrm{V}_{i0}^2). \tag{5.53}$$

The above equation gives no shock solution, only the existence of solitons [see Fig. 5.1].

Moiseev and Sagdeev [151] have shown that the reflection of ions from the shock front results in the formation of oscillatory structure in the collisionless shock as shown in Fig. 5.3(a). The labels I and II indicate the region left and right of x_m, i.e., $x < x_m$ and $x > x_m$, respectively, as shown in Fig. 5.3(a). The shock front connects the two different states of plasma, i.e., ordered oscillations and the unperturbed state. Although, the thermal energy and energy distribution between the oscillations depend on the collisionless dissipation mechanism. If the number of reflected ions is small, and in the absence of shock dissipation $\phi_{\mathrm{I}} = \phi_{\mathrm{II}}$, $\lambda = \infty$, this results in the symmetric solitary wave solution. In case when more reflected ions are taken in the account, the dissipation of the shock plays an important role and results in a potential which varies from Eq. (5.51) with two additional terms on the right side

$$\frac{e\mathrm{N}_0}{\epsilon_0} f(\phi) \quad \text{and} \quad -\frac{e\mathrm{N}_0 \mathrm{V}_{i0}}{\epsilon_0}\left(\mathrm{V}_{i0}^2 - \frac{2e\phi}{\mathrm{m}_i}\right)^{-\frac{1}{2}} f(\phi_1). \tag{5.54}$$

The first term indicates the contribution of the reflected ions, and the second term gives the total ions minus the number of reflected ions. Here $\mathrm{N}_0 f(\phi)$ gives the density of reflected ions, which is described by ϕ. The potential, ϕ_{I}, is associated with the backward reflected ions from the potential at the shock front and goes to infinity. Here, we have assumed that a minimal number of ions are reflected ($f << 1$), and the potential, ϕ_{I} at the shock is proportional to f, i.e., $\phi_{\mathrm{I}} \propto f$. The potential, ϕ_{II} is associated with ions which are reflected behind the shock front, and proportional to the square root of the number of reflected ions, for instance, $\phi_{\mathrm{II}} >> \phi_{\mathrm{I}}$. In region II, ϕ_m and ϕ_{II} represent the plasma states and provide the oscillation amplitude and their wavelength, λ. In region II, by considering the equality of electron and ion densities at $x = -\infty$, $\mathrm{V}_{th} >> \mathrm{V}_{i0}$, and neglecting reflection effect for electrons, the convenient equations for regions I and II become

$$\begin{aligned}
(\mathbf{I}) \Rightarrow \frac{\partial^2\phi}{\partial x^2} = -\frac{\partial \Psi_{\mathrm{I}}}{\partial \phi} = -\frac{e\mathrm{N}_0}{\epsilon_0}\Bigg\{&[1+f(\phi_{\mathrm{I}})]\exp\left(\frac{e\phi}{k_B \mathrm{T}_e}\right) \\
&-[1-f(\phi_{\mathrm{I}})]\mathrm{V}_{i0}\left(\mathrm{V}_{i0}^2 - \frac{2e\phi}{\mathrm{m}_i}\right)^{-\frac{1}{2}} - 2f(\phi)\Bigg\}, \\
(\mathbf{II}) \Rightarrow \frac{\partial^2\phi}{\partial x^2} = -\frac{\partial \Psi_{\mathrm{II}}}{\partial \phi} = -\frac{e\mathrm{N}_0}{\epsilon_0}\Bigg\{&[1+f(\phi_{\mathrm{I}})]\exp\left(\frac{e\phi}{k_B \mathrm{T}_e}\right) \\
&-[1-f(\phi_{\mathrm{I}})]\mathrm{V}_{i0}\left(\mathrm{V}_{i0}^2 - \frac{2e\phi}{\mathrm{m}_i}\right)^{-\frac{1}{2}}\Bigg\}.
\end{aligned} \tag{5.55}$$

By solving these equations for ϕ and $\mathrm{d}\phi/\mathrm{dx}$ at x_m for continuity boundary

conditions in regions I and II, they give the potential profiles as shown in Fig. 5.3(b). As $f(\phi_m) = 0$, the integration constant for the above equations can be found by defining $\Psi_{\rm I}(\phi_m) = \Psi_{\rm II}(\phi_m)$. This results in $\frac{1}{2}(\frac{{\rm d}\phi}{{\rm dx}})^2 + \Psi_{\rm I,II} = 0$ and at $\phi = \phi_m$, $\partial\phi/\partial x$ is continuos. The potential, $\Psi_{\rm I}$ makes its first round along the soliton structure at $\phi_{\rm I} \rightarrow \phi_m$ and when it enters the region II, it oscillates indefinitely in between potential ϕ_m and $\phi_{\rm II}$ in the potential of $\Psi_{\rm II}$.

At this moment, if we consider the motion of the particle in a potential well, $\Psi(\phi)$, it can be concluded that the action of the reflected particles makes the total energy, $\rm E_\phi$ negative, and results in a periodic structure behind the shock front. The change in the energy $\rm E_\phi$ depends on the number of the reflected ions

$$-\,{\rm E}_\phi = \int_0^{\phi_m} f(\phi){\rm d}\phi. \tag{5.56}$$

At small ϕ the potential energy changes quadratically and $\phi_{\rm II}$ depends on the square root of energy

$$\phi_{\rm II} = \sqrt{-{\rm E}_\phi}, \tag{5.57}$$

and the oscillations increase logarithmically with the decrease in the energy, i.e. $\lambda \sim \ln(\text{-}\frac{1}{{\rm E}_\phi})$ and the minimum value of $\phi_{\rm II}$ is given by

$$\phi_{\rm II} = \frac{2{\rm M}}{\sqrt{{\rm M}^2-1}}\sqrt{\frac{{\rm T}_e}{e}\int_0^{\phi_m} f(\phi){\rm d}\phi}. \tag{5.58}$$

The value of M is very close to the corresponding value in a solitary wave with the same Mach number. Presently the ion reflection has another significant impact on the solitary/shock wave, as the momentum transfer from shock wave front to the reflected ions retards the shock in the region of reflection. The wavelength of oscillations behind shock front is given by [151]

$$\lambda \simeq \sqrt{\frac{{\rm T}_e}{({\rm M}^2-1)\pi e^2 {\rm N}_0^2}}\,\ln\left(\frac{\phi_m}{\phi}\right). \tag{5.59}$$

The previous analysis helps to explain the difference between shocks and solitons. Ion reflection from the shock front has unique importance in the formation of collisionless shock, and numerical simulations can be utilized to understand the dynamics of shock formations and ion reflection.

Chapter 6

Material Dependence of CSA

6.1 Introduction

The density discontinuity or the relative drift between the two plasmas is needed to generate the strong electrostatic shocks in collisionless plasmas, which is capable of accelerating the ions. These shocks can be demonstrated in the laboratory by the interaction of high-intensity laser with plasmas. However, to generate the high-quality ion beams via CSA mechanism, a specially tailored density profile is required [46].

In this chapter, we used the EPOCH particle-in-cell open source code for better understanding of the generation of electrostatic collisionless shock and proton acceleration from the shock formed in plasmas of different target material composition. The influence of different material depending on their <Z/A> on the shock-accelerated proton beams have been investigated. The different targets use hydrogen, carbon, oxygen, and chlorine to give a range of <Z/A> of 1 to 0.48 [See Table 6.1]. Here we intend to find the most suitable target material to achieve the high flux with narrow energy-spread proton beams through CSA mechanism.

6.2 Simulations Parameters

The formation of electrostatic collisionless shocks and their corresponding proton reflection in different target materials have been investigated using particle-in-cell (PIC) code EPOCH, run in 2D geometry [103]. The simulation box is 300 μm $\times$ 6 μm in size and composed of 9000 $\times$ 180 grid points corresponding to spatial step-size $\Delta x = \Delta y = 0.033$ μm along x- and y-axis, respectively. Depending on the target material composition, 24 - 30 particles per cell were used in the simulations. The boundary conditions are open in x and periodic in y for both fields and particles.

The laser pulse is modelled as the electromagnetic plane wave with linear p-polarization along y-axis and propagates in x-direction. The normally incident laser pulse with infinite spot-size has Gaussian temporal profile with 1.5 ps full-width at half-maximum. The peak intensity is 1.4×10^{19} Wcm^{-2} ($a_0 = 3.35$) as shown in Fig. 6.1(a). The laser pulse interacts with a fully ionized plasma density at $x = 40$ μm. The simulated targets are composed of a special density profile with an exponentially increasing 5 μm scale-length front region extending for 30 μm ($L_f = 5$ μm), 5 μm uniform region and an exponentially decreasing

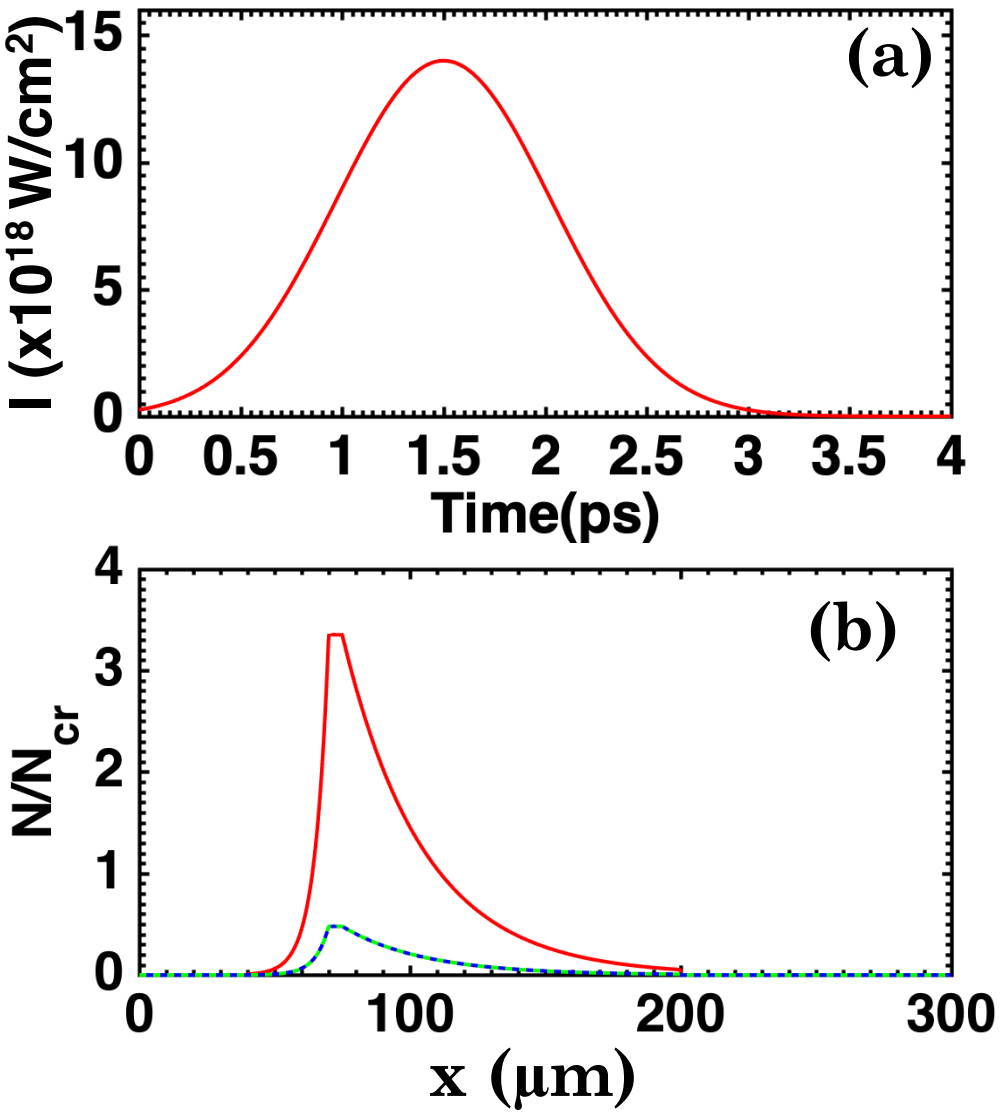


FIGURE 6.1: (a) The laser profile used in PIC simulations, the laser peaks at 1.5 ps, with a maximum intensity 1.4×10^{19} $\mathrm{Wcm^{-2}}$. The full-width at half-maximum of the laser is 1.5 ps. (b) The normalized initial density profile used in PIC simulations for fully ionized CH target material. The the Hydrogen ($\mathrm{N_H}$) and Carbon ($\mathrm{N_C}$) number densities are same. The laser start interacting with plasma from the left side of the simulations box. A 40 μm front- and 100 μm rear-side vacuum regions is used to avoid the boundary effects in our simulations.

profile with 30 μm scale-length for 125 μm (L_b = 30 μm) on the rear-side of the target. The maximum electron density is fixed at the relativistic critical density $\mathrm{a_0 N}_{cr}$, where $\mathrm{N}_{cr} = 1.12\times10^{21}$ $\mathrm{cm^{-3}}$ is the critical plasma density for 1 μm wavelength laser used in these simulations. The longitudinal electron

TABLE 6.1: The different target materials, their average charge-to-mass ratio (<Z/A>), average charge (<Z>), average mass (<A>), and corresponding ion densities calculated using quasi-neutral plasma condition used in PIC simulations. All ion densities are represented in term of electrons density (N_e) = $a_0 N_{cr}$. Note, all ions are fully ionised except chlorine which has Z_{Cl}=15.

Material	**<Z/A>**	**<Z>**	**<A>**	$\mathbf{N}_H$	$\mathbf{N}_C$	$\mathbf{N}_{Cl}$ or $\mathbf{N}_O$
C_2H_3Cl	0.4839	30	62	$3\times N_e/30$	$2\times N_e/30$	$N_e/30$
$C_8H_6Cl_2$	0.4884	84	172	$6\times N_e/84$	$8\times N_e/84$	$2\times N_e/84$
C_8H_7Cl	0.5072	70	138	$7\times N_e/70$	$8\times N_e/70$	$N_e/70$
$C_8H_6O_2$	0.5224	70	134	$6\times N_e/70$	$8\times N_e/70$	$2\times N_e/70$
$C_8H_8O_2$	0.5294	72	136	$8\times N_e/72$	$8\times N_e/72$	$2\times N_e/72$
CH	0.5385	7	13	$N_e/7$	$N_e/7$	-
CH_2	0.5714	8	14	$2\times N_e/8$	$N_e/8$	-
He^3H	0.8	4	5	$N_e/4$	$N_e/4$	-
Hydrogen	1	1	1	N_e	-	-

density profile can be given by

$$N_e = \begin{cases} a_0 N_{cr} \exp\left(\frac{x - 70\mu m}{L_f}\right) & \text{for } 40\ \mu m \le x \le 70\ \mu m, \\ a_0 N_{cr} & \text{for } 70\ \mu m \le x \le 75\ \mu m, \\ a_0 N_{cr} \exp\left(\frac{75\mu m - x}{L_b}\right) & \text{for } 75\ \mu m \le x \le 200\ \mu m. \end{cases} \tag{6.1}$$

The corresponding ion densities for each material are calculated from the quasi-neutral plasma condition. The normalized initial density profiles for the CH plasma are shown in Fig. 6.1(b). For fully ionized CH plasma, the quasi-neutral plasma condition is given by $N_e = Z_H N_H + Z_C N_C$, where N and Z represent the number density and charge state, respectively. The subscripts e, H and C, stands for electron, Hydrogen, and Carbon, respectively. This results in $N_H = N_C = N_e/7$. Table 6.1 signifies the different target materials used in PIC simulations, with their respective average charge-to-mass ratio (<Z/A>), and their corresponding ion densities determined using quasi-neutral plasma conditions.

6.3 Electrostatic Collisionless Shock Formation

Numerical simulations are used in order to understand the laser-driven collisionless shock wave ion acceleration in different target material plasmas. The laser pulse starts interacting with the portion of the target with a density smaller than the critical density. Evidence of the interaction of a high-intensity laser with relativistic critical plasma density is seen in Fig. 6.2(a). This shows the normalized proton density N_H/N_{cr} in C_2H_3Cl plasma for a number of time after the peak of the laser, which enter the simulation setup at $t = 1.5$ ps. During the time from $t = 0$ to $t = 1.75$ ps the interaction of laser with plasma results in the uniform electron heating via J×B mechanism [44]. The radiation pressure

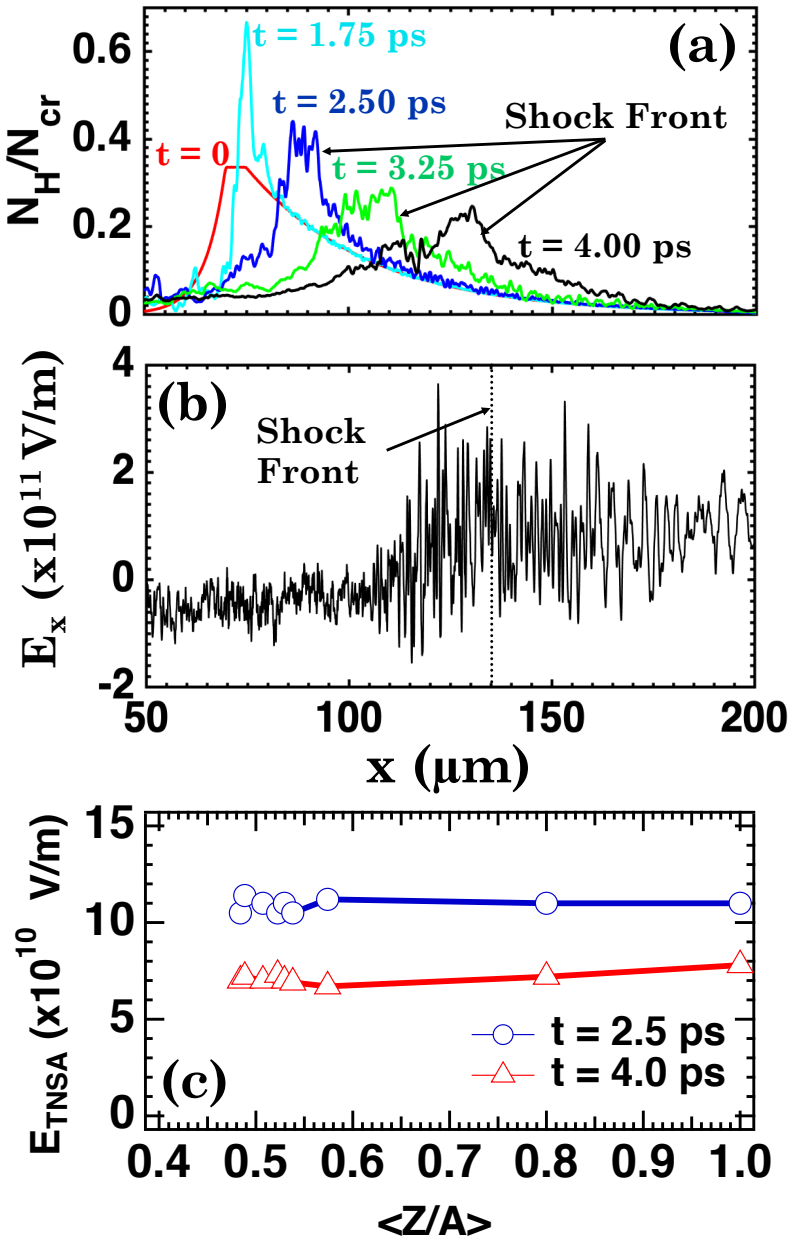


FIGURE 6.2: (a) The temporal evolution of N_H/N_{cr} in C_2H_3Cl plasma at t = 0, 1.75, 2.50, 3.25, and 4.0 ps. (b) The laser-cycle averaged 1D profile of electrostatic field (E_x) at t = 4.0 ps in C_2H_3Cl plasma. (c) <Z/A> dependence of non-oscillating component of the TNSA electrostatic field in the upstream region at t = 2.50 ps and t = 4.0 ps.

of the laser pulse compresses the plasma in front of the exponentially decreasing density on the rear-side of the target, as shown in Fig. 6.2(a). As time evolves, the density profile on the rear-side of the target starts expanding thermally, resulting in the formation of electrostatic collisionless shock. This shock front propagates in the forward direction with time.

After interaction with the laser, the electrons move relativistically within the plasma. The massive protons/ions cannot keep up with the electrons thus setting up a charge imbalance or ambipolar electrostatic field (E_x). Figure

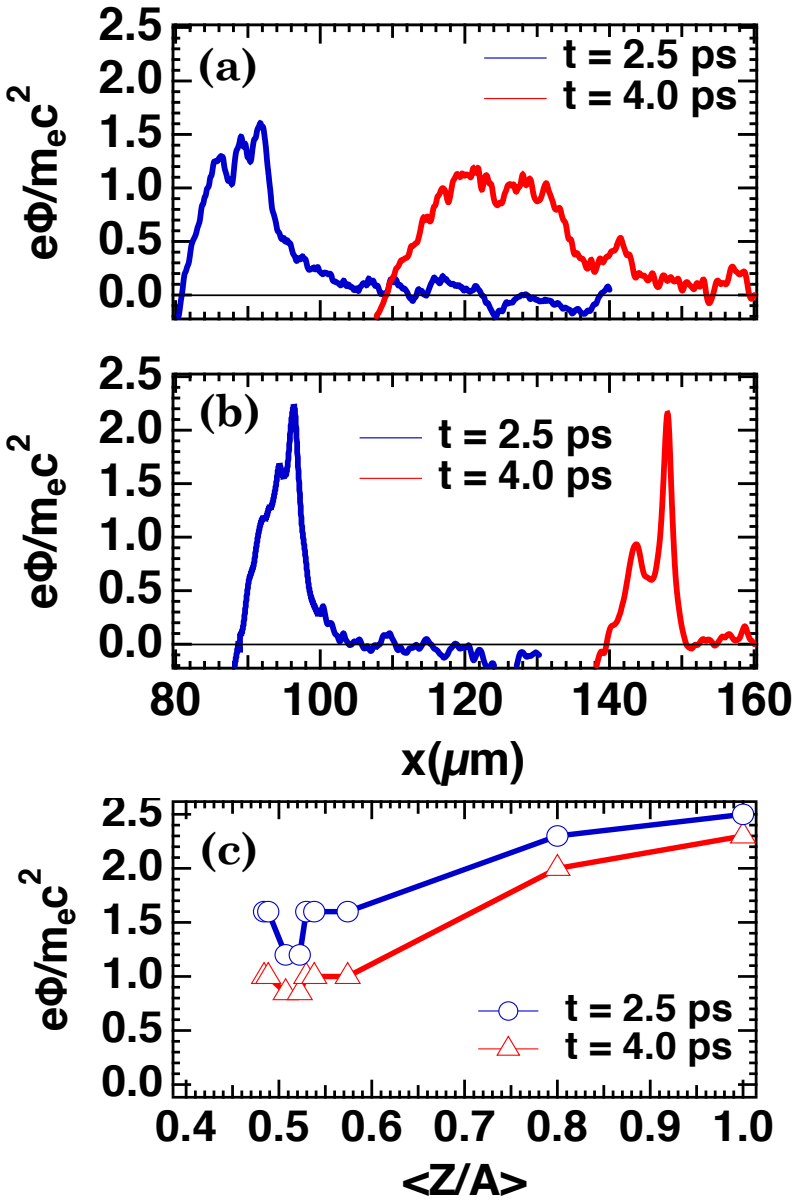


FIGURE 6.3: The spatial profile of electrostatic potentials in (a) C_2H_3Cl and (b) Hydrogen plasma at $t = 2.5$ and 4.0 ps. (c) The <Z/A> dependence of the electrostatic potential at the shock front calculated by integrating $E_x - E_{\mathrm{TNSA}}$ along x-direction at $t = 2.5$ ps and $t = 4.0$ ps.

6.2(b) represents the electrostatic field in the C_2H_3Cl plasma at $t = 4.0$ ps. At a sharp plasma-vacuum interface, some of these relativistic electrons blast into the vacuum and results in a strong charge-separation electrostatic field ($\mathrm{E_{TNSA}}$). This sheath field can be controlled by using an exponentially decreasing profile with a scale-length, L_b on the rear-side of the target. The amplitude of this sheath field is

$$\mathrm{E_{TNSA}} = \frac{k_B \mathrm{T}_e}{\mathrm{L}_b}. \tag{6.2}$$

The E_{TNSA} field depends on the rear-side plasma scale-length. Thus, an exponentially decreasing density profile in the rear-side of the target results in the uniform E_{TNSA} in the upstream region [137]. This will help to preserve the mono-energetic feature of shock-accelerated ions. Figure 6.2(c) shows that the E_{TNSA} field is very similar for all target materials and decreases with the increase in time. The non-oscillating component of E_{TNSA} accelerates the upstream expanding ions to a uniform velocity (V_0^i) in x-direction.

In order to determine the electrostatic potential (ϕ) jump associated with the electrostatic collisionless shock front. The simple correlation between the electric field and potential is applied, i.e. (E_x = - dϕ/dt) [90]. As the exponentially decreasing density on the rear-side of the target results in a small amplitude TNSA field [see Eq. (6.2)]. Therefore, the non-oscillating component of E_{TNSA} is subtracted from the overall electrostatic field (E_x) and integrated along the x-axis. Consequently, the spatial profile for the electrostatic potential can be established by using the relation

$$\phi = \int_{\infty}^{x} (E_x - E_{TNSA}) dx. \tag{6.3}$$

Figures 6.3(a) and 6.3(b) indicate the spatial distribution of electrostatic potential at t = 2.50 and 4.0 ps for the C_2H_3Cl and H plasmas, respectively. The shock structure has a large electrostatic potential at the shock front for both plasmas. At t = 2.50 ps, the electrostatic potential at the shock front becomes high enough and to start reflecting the upstream expanding ions. As time grows further, the potential jump at the shock front is gradually dissipated by ion reflection. This results in a smaller potential jump at the shock front in lower <Z/A> materials, as shown in Fig. 6.3(c). As we mention in Chapter 5, the particle reflection in collisionless shock can be considered as the major source for the shock dissipation. Thus, it might be possible that a large number of protons are accelerated in lower <Z/A> plasmas compared to the pure H. Moreover, the ion reflection is compensated by the change in the electrostatic potential amplitude at the shock front.

6.3.1 Electron temperature and Shock Velocity

In the early stage of high-intensity laser-plasma interaction, a fraction of high-energy (several MeV), relativistic electrons are accelerated by laser-pulse. These electrons go within the plasma and later recirculate across it, and heat up the bulk electrons. As a result of recirculation, the whole plasma is strongly and uniformly heated via J×B mechanism [44], as illustrated by electron phase-space in C_2H_3Cl plasma at t = 4.0 ps in Fig. 6.4(a). An electron energy spectrum is taken at t = 4.0 ps when the recirculation of the electrons has been stopped, and the whole plasma seems to be in the thermal equilibrium, as shown in Fig. 6.4(b). This electron energy spectrum is taken at $\Delta x'$ = 20 μm in the upstream region ahead of the shock front, this is shown by a vertical box in Fig 6.4(a). The electron energy distribution has been fitted to a 2D-relativistic Maxwellian of form

$$f(E) \propto E\exp(-E/T_e), \tag{6.4}$$

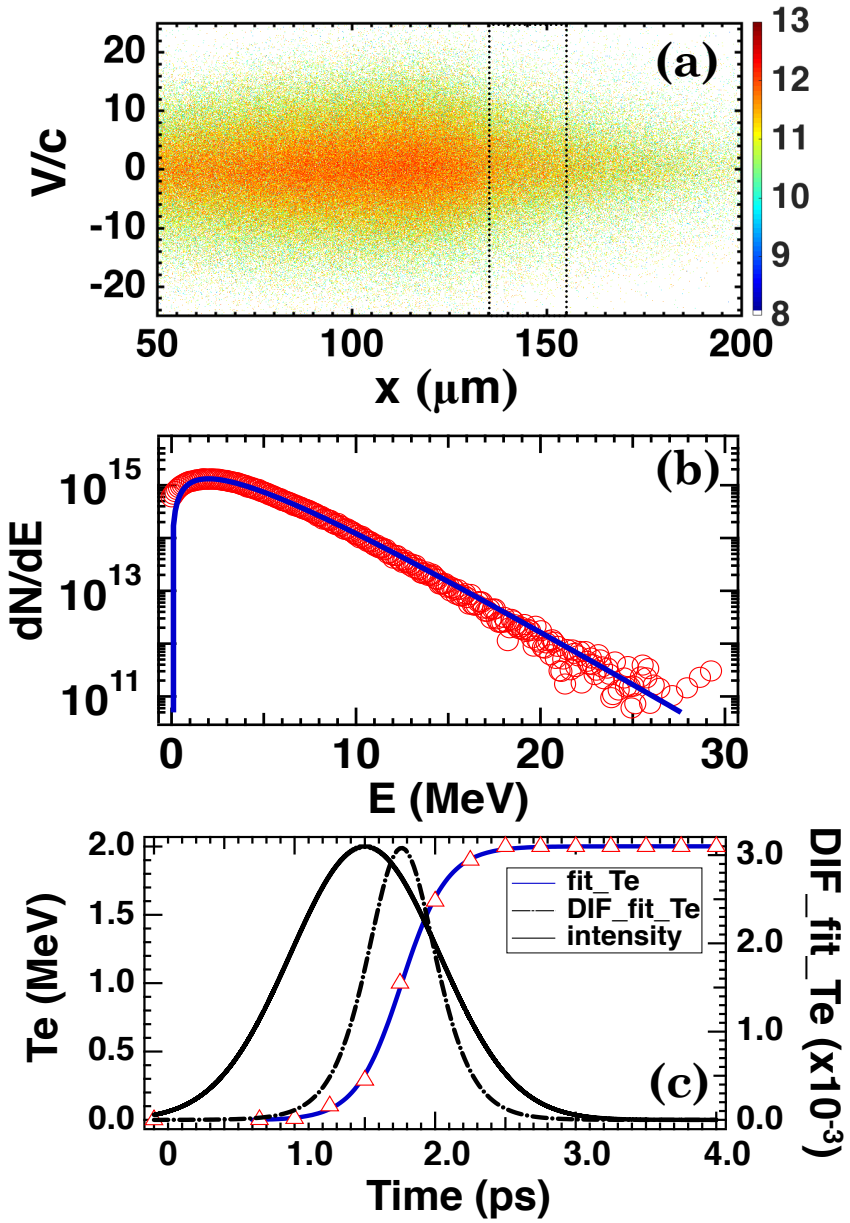


FIGURE 6.4: (a) The electron phase-space in C_2H_3Cl plasma at $t = 4.0$ ps. (b) The electron energy spectrum taken at $\Delta x' = 20$ μm in the upstream region of shock front (rectangle Fig. 4(a)) in C_2H_3Cl (circles) plasma at $t = 4.0$ ps. The electron energy spectrum is fitted with a 2D-relativistic Maxwellian $f(E) = aEexp(-E/T_e)$ (solid line), where a is constant, E is the energy of electrons in x-direction, T_e gives electron temperature in the upstream region. (c) The temporal evolution of T_e calculated by fitting a 2D-relativistic Maxwellian at each time. The T_e is very well fitted with sigmoid function (solid line) and the derivative (DIF) of sigmoid function (dot-dashed line) peaks at $t = 1.75$ ps.

where E is the relativistic energy of electrons, as shown in Fig. 6.4(b). The extracted electron temperature $T_e \sim 2.0$ MeV. The temporal progression of T_e is represented in Fig. 6.4(c). We study the time progression of electron temperature to study the electron heating in laser-plasma interaction. The

electron temperature, T_e is obtained by fitting the 2D Maxwellian defined by Eq. (6.4) at each time. Early in time, at $t = 1.0$ ps, T_e is approximately equivalent to the initial temperature set in the simulations. After the interaction of the laser peak, T_e rises sharply and reached ~ 2.0 MeV at $t = 2.50$ ps and remain same throughout the simulations. This implies that the electron energy distribution reached the thermal equilibrium by $t = 2.50$ ps. A Sigmoid function of the form

$$S(t) = \frac{1}{1 + \exp(-at)}, \tag{6.5}$$

is used to fit the time evolution of T_e. Here, t is the time and a is the constant. The derivative of Eq. (6.5) peaked at $t = 1.75$ ps as shown in Fig. 6.4(c). The obtained $T_e \sim 2.0$ MeV is the same for all target materials. This is because the ponderomotive electron temperature depends on the laser vector potential, i.e. $\propto a_0$ and the electron density of the plasma, N_e which is same for all target materials.

In multi-ion species plasmas, we determine the ion-acoustic velocity (C_s^i) by using

$$C_s^i = \sqrt{\frac{Z_i}{A_i}\frac{T_e}{m_p}}. \tag{6.6}$$

Here, the superscript/subscript, i signifies the different ions species. Since the shock is propagating within the protons density, therefore, $i = p$, and $Z = A = 1$. Therefore, the ion-acoustic velocity, $C_s = \sqrt{T_e/m_p} = 0.0462c$ is fixed for all material plasmas. This is because the electron temperature is the same for all plasmas. In the PRAB article [152], we have assumed that the ion-acoustic velocity in the multi-ion species plasmas depends on the average <Z/A>, which is different from the assumption made in another article and this thesis. The density steepening and thermal expansion of the exponentially decreasing density on the rear-side of the plasma leads to the shock formation. The shock front propagates in the forward direction with an exponential dependence on time. The temporal variation of shock positions (X_{sh}) in H and C_2H_3Cl plasmas are shown in Fig. 6.5(a). A derivative of X_{sh} with time gives the shock velocity V_{sh}. As there is an exponential decrease in rear surface density; as a result, V_{sh} increases exponentially as a function of time for all the target materials. The change in V_{sh} in different target materials can be explained with the help of hole-boring velocity, which can be given by

$$V_{HB} = c\sqrt{\frac{Z}{2A}\frac{m_e}{m_p}\frac{N_{cr}}{N_e}a_0^2}, \tag{6.7}$$

for low a_0 [36]. As a_0 and N_e are the same for all the materials, V_{HB} is only dependent on the square root of <Z/A>. As <Z/A> increases, the corresponding V_{sh} increases. As a result, material with the largest <Z/A> corresponds to the largest V_{HB} and V_{sh}, as shown in Fig. 6.5(b).

In multi-ion species plasmas, the velocity distribution of the expanding protons is broad due to the presence of heavy-ions or low <Z/A> ions. [*In Chapter*

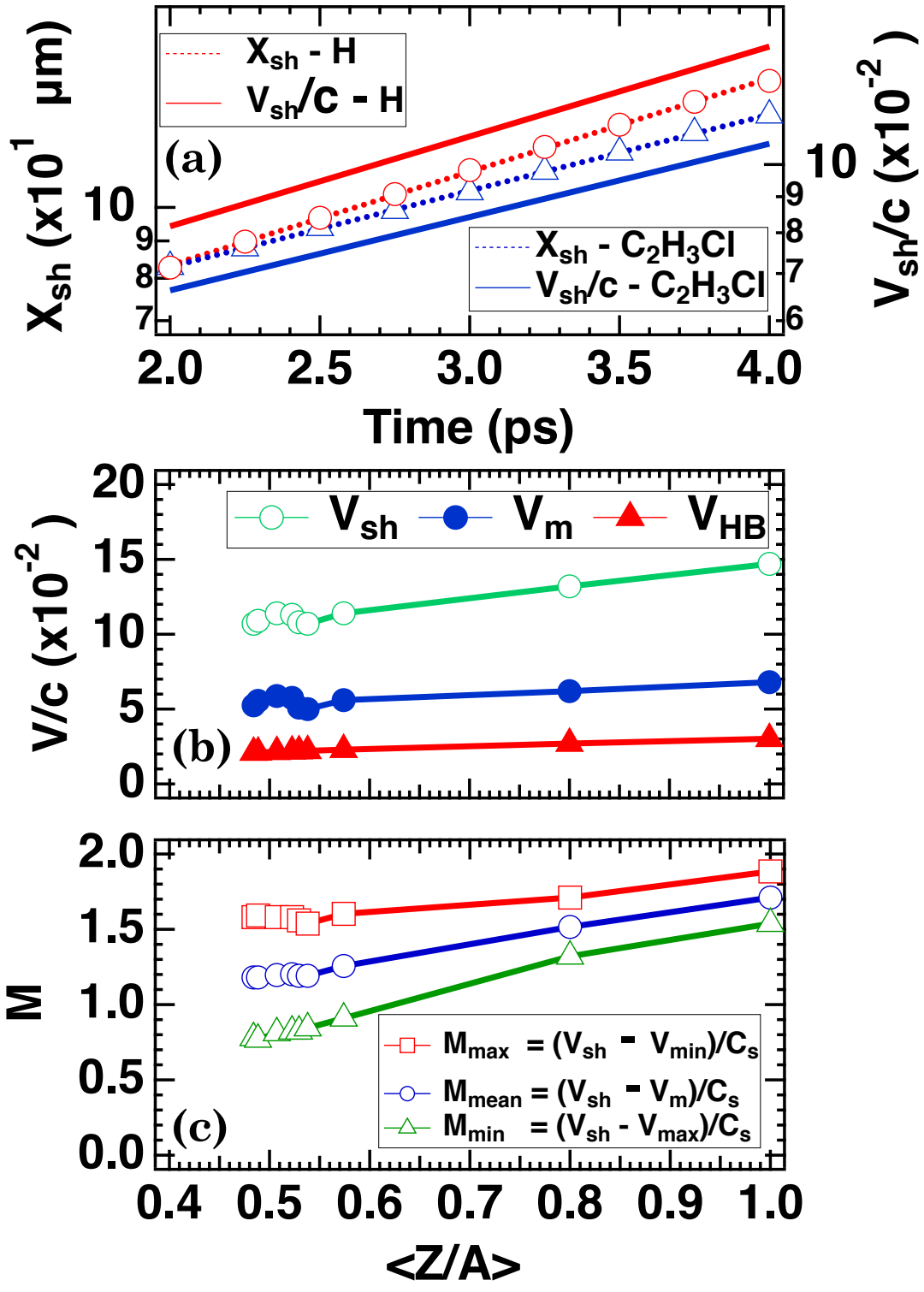


FIGURE 6.5: (a) The temporal evolution of shock positions in H and C_2H_3Cl plasmas. The derivative of the shock position with respect to time gives the shock velocity V_{sh}. (b) <Z/A> dependence of mean velocity (V_{mean}) of the expanding protons velocity (V_0), shock velocity V_{sh}, and the velocity of shock reflected protons $2V_{sh} - V_L$ at $t =$ 4.0 ps. (c) <Z/A> dependence of Mach numbers calculated for different upstream expanding ion velocities at $t = 4.0$ ps.

7, we will discuss about the broadening of expanding protons]. This broad velocity distribution (V_0) of upstream expanding proton results in a variation in the Mach number (M). We describe it as

$$M = \frac{V_{sh} - V_m}{C_s}, \tag{6.8}$$

where V_m is the mean value of V_0 as shown in Fig. 6.5(b). As inferred from Fig. 6.5(c), the estimated Mach number, M = 1.2−1.7, which increases as a function of <Z/A>. This is because the V_{sh} - V_m increases with <Z/A>, and the ion-acoustic velocity, C_s is same for all the target materials used. As predicted by Forslund & Friedsburg et al. [153], the collisionless shock can reflect the upstream protons for any values of M>1, when the potential energy at the shock front is larger than the kinetic energy of the upstream expanding protons in the shock-rest frame. As a result, the shock dissipation happens by proton reflection at the shock front. However, as the Mach number approaches the lower critical Mach number (M_{cr} = 1.6 for an isothermal electron gas), non-steady solitary-wave solutions are possible with the peak potential too small to reflect the ions. Therefore, there is no lower critical Mach number exists for ion reflection. As long as the peak potential at the shock front is high enough for any M>1, the reflected ions will be present.

6.3.2 TNSA Electrostatic Field Scaling

The exponentially decreasing density profile on the rear-side of target leads to the small amplitude TNSA field, E_{TNSA} [see Eq. (6.2)]. This E_{TNSA} field is relatively uniform and accelerates the upstream expanding ions to a uniform velocity. The amplitude of this E_{TNSA} field can be approximated by measuring the temporal progression of the expanding ion velocity in the upstream region. The velocity of the Cl-ions (V_{Cl}) is measured at the peak of the velocity distribution of expanding Cl-ions taken at $\Delta x = 3$ μm in the upstream region of C_2H_3Cl plasma. Figure 6.6(a) shows the time evolvement of V_{Cl} in C_2H_3Cl plasma. The change in V_{Cl} with time can be characterized as

$$V_{Cl} = \begin{cases} \propto t^2 & \text{for 1.0 ps} < t < \text{2.75 ps}, \\ \propto \ln(t) & \text{for 2.25 ps} < t < \text{4.0 ps}. \end{cases} \tag{6.9}$$

It is clear that the later in time, t^2 dependence of V_{Cl} changes to the logarithmic dependence on time. As a result, a 2nd order polynomial (at t = 1.0 ps to t = 2.75 ps) and a logarithmic curve (at t = 2.25 ps to t = 4.0 ps) is used to fit the V_{Cl}. The non-oscillating component of E_{TNSA} can be estimated by comparing the electrostatic forces (ZeE_{TNSA}) with the Lorentz force ($Am_p dV/dt$) in the upstream region. On that account,

$$E_{TNSA} = \frac{A}{Z}\frac{m_p}{e}\left(\frac{dV}{dt}\right), \tag{6.10}$$

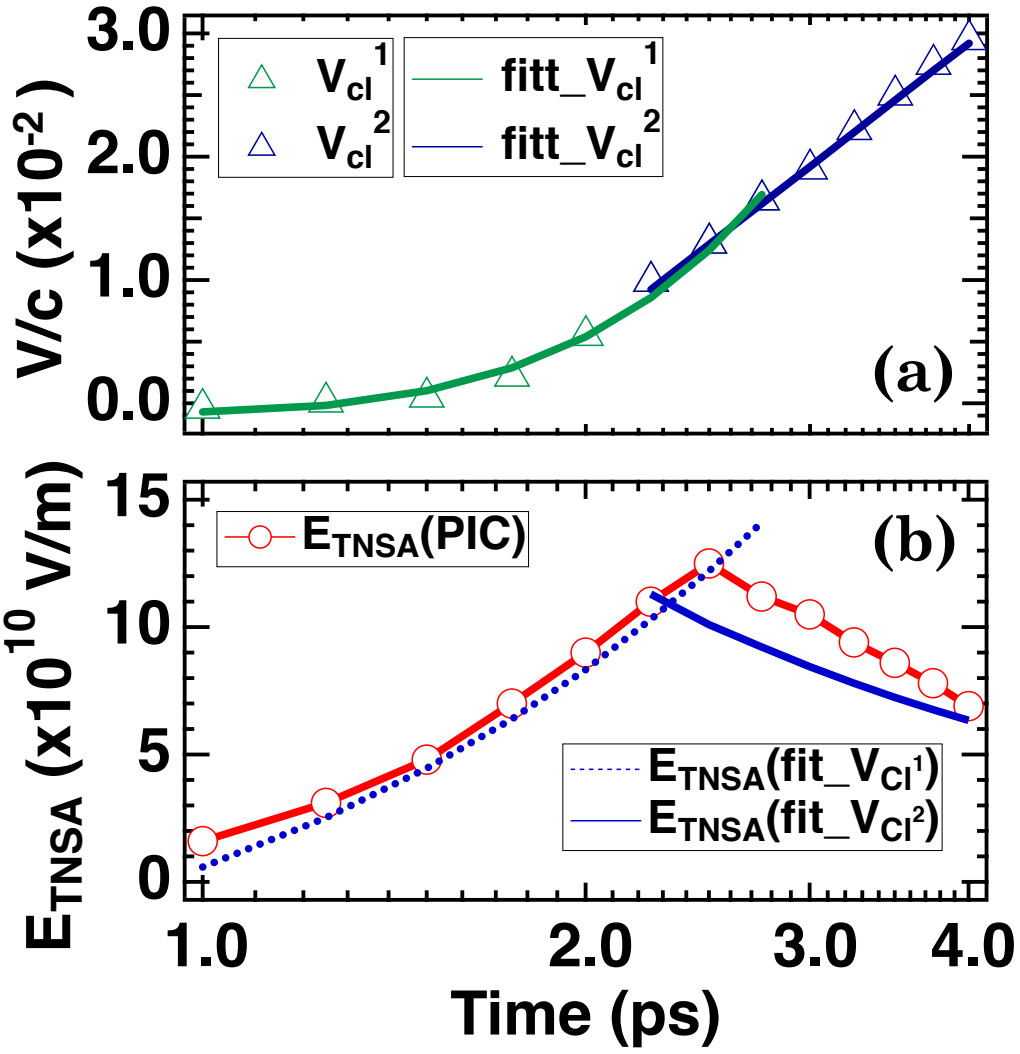


FIGURE 6.6: (a) The velocity of Cl-ions V_{Cl} derived from the peak of velocity spectrum dN/dV_{Cl} taken at $\Delta x = 3$ μm in the upstream region. The V_{Cl} is fitted to the 2nd order polynomial from $t = 1.0$ ps to 2.75 ps, and a logarithmic curve from $t = 2.25$ ps to 4.0 ps. (b) The E_{TNSA} is derived from the V_{Cl}, which follows a $\propto t$ from $t = 1.0$ ps to 2.75 ps and a $1/t$ dependences from $t = 2.25$ ps to 4.0 ps.

where Z is charge state, and A is the mass number of the ion, m_p is the mass of the proton, e is the electron charge, and dV/dt is the rate of change of the velocity. A derivative of the fitted V_{Cl} with <Z/A> = 0.429 for Cl-ions point out that the relationship of TNSA field on time can be given by

$$\mathrm{E_{TNSA}} = \begin{cases} \propto t & \text{for 1.0 ps} < t < \text{2.75 ps}, \\ \propto 1/t & \text{for 2.25 ps} < t < \text{4.0 ps}, \end{cases} \tag{6.11}$$

as illustrated in Fig. 6.6(b). Mora anticipates the logarithmic dependence of V_{Cl} and $1/t$ dependence of E_{TNSA} [110]. The non-oscillating component of E_{TNSA} approximated by the time evolvement of V_{Cl} and measured in the PIC simulations demonstrate a similar trend and agree relatively well with each

other. The non-oscillating component of this temporally changing E_{TNSA} field accelerates the upstream ions to a uniform velocity V_0 over time.

6.3.3 Proton Acceleration via CSA

As the ES collisionless shock propagates within the upstream expanding plasma, it accelerates a fraction of upstream ions to the twice of the shock velocity in the shock rest frame. To accelerate the ions via CSA mechanism, the potential energy at the shock front must be larger than the kinetic energy of the upstream expanding ions. In other words, the electrostatic potential at the shock front must satisfy the following conditions [41]

$$Ze\phi \geq \frac{1}{2}Am_p(V_{sh}^i - V_0^i)^2. \tag{6.12}$$

Here superscript i symbolizes the different ion species depending on their Z/A. The lower threshold velocity (V_L^i) in V_0^i for ion reflection via CSA mechanism can be given by

$$V_L^i = V_{sh}^i - \sqrt{\frac{Z}{A}\frac{2e\phi}{m_p}}. \tag{6.13}$$

Consequently,

$$V_L^i \leq V_0^i \leq V_{sh}^i. \tag{6.14}$$

Equation (6.14) implies the lower V_L^i and upper V_{sh}^i threshold velocities in V_0^i for ion reflection. As a result, all ions with a velocity component in between V_L^i and V_{sh}^i are reflected by the shock potential. Since the upstream expanding protons are propagating in the same direction with different velocities. The upstream expanding protons are reflected from shock front and gain a velocity which is twice of the shock velocity V_{sh}^i minus lower threshold velocity V_L^i, i.e., $V_r = 2(V_{sh}^i - V_L^i) + V_L^i = 2V_{sh}^i - V_L^i$. If the upstream expanding velocity is zero, the ions will be reflected to the twice of the shock velocity only, i.e., $V_r^i = 2V_{sh}^i$.

For protons $Z = A = 1$ and neglecting the superscript i, therefore, $V_L = V_{sh} - \sqrt{2e\phi/m_p}$. Figure 6.7 illustrates the temporal evolution of the proton phase-space and their respective velocity distribution taken in the upstream region ahead of the shock front in C_2H_3Cl plasma. The velocity distribution is integrated from the velocities within the vertical box in the phase-space plots, which spans across a range of $\Delta x = 3$ μm. The populations of the shock reflected protons are visible from the phase-space plane. By $t = 1.5$ ps (laser intensity peak), the potential at the shock front starts growing, and some of the expanding protons satisfy the lower threshold for the ions reflection, i.e., Eq. (6.14). The potential jump at the shock front becomes maximum by $t = 2.5$ ps, and begin reflecting the upstream expanding protons more actively. Thus, a significantly large number of expanding protons start to satisfy Eq. (6.14) at all time, and results in a large fraction of protons to be accelerated via CSA mechanism.

Figure 6.8 indicates the proton phase-space and their corresponding velocity spectrum in different material plasmas at $t = 4.0$ ps. Here, the 1st, 2nd, and 3rd

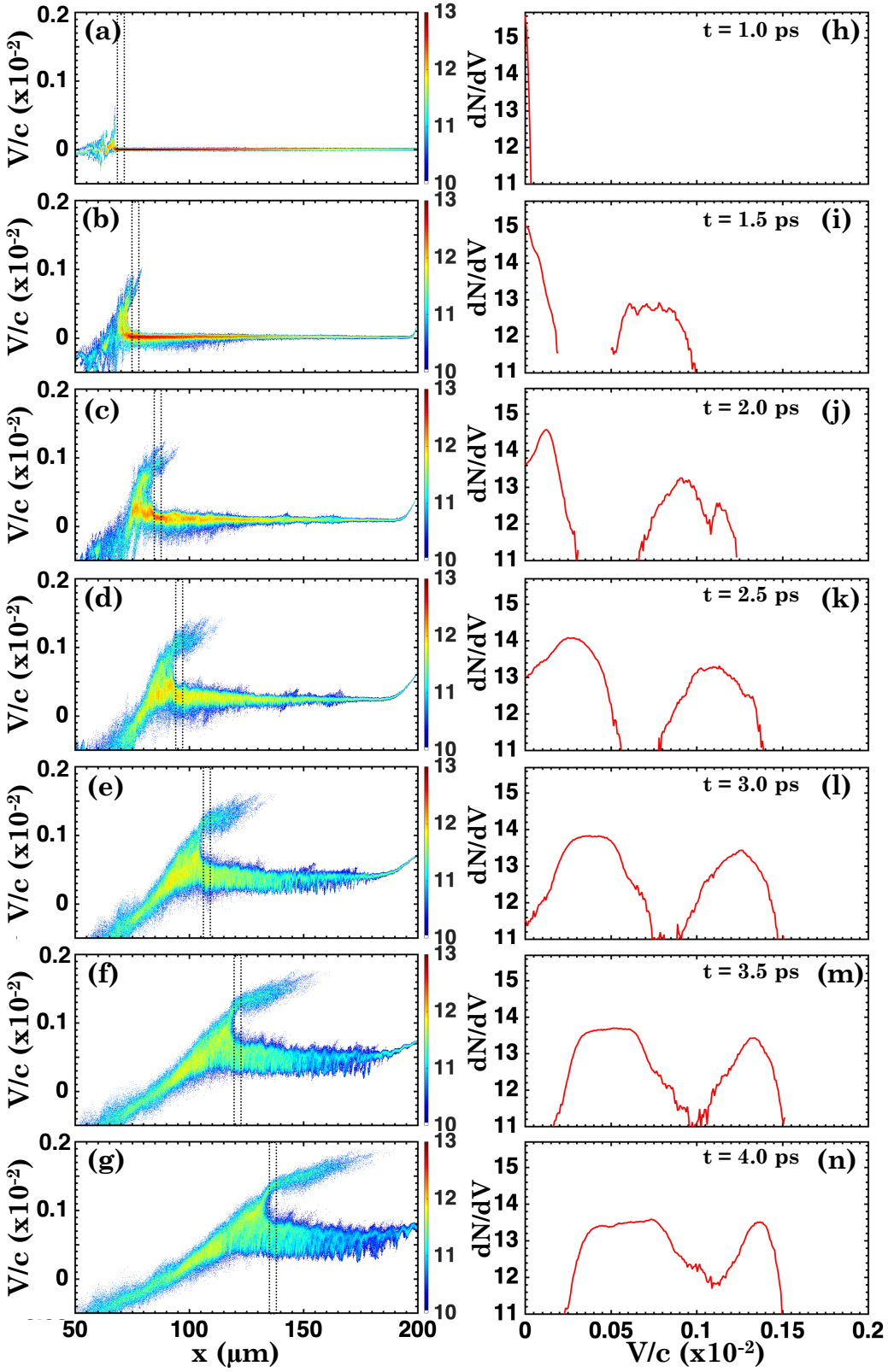


FIGURE 6.7: The temporal evolution of (a)-(g) proton phase-space and (h)-(n) their corresponding velocity spectrum taken at $\Delta x = 3$ μm in the upstream region (shown by vertical dotted lines in phase-space) in C_2H_3Cl plasma.

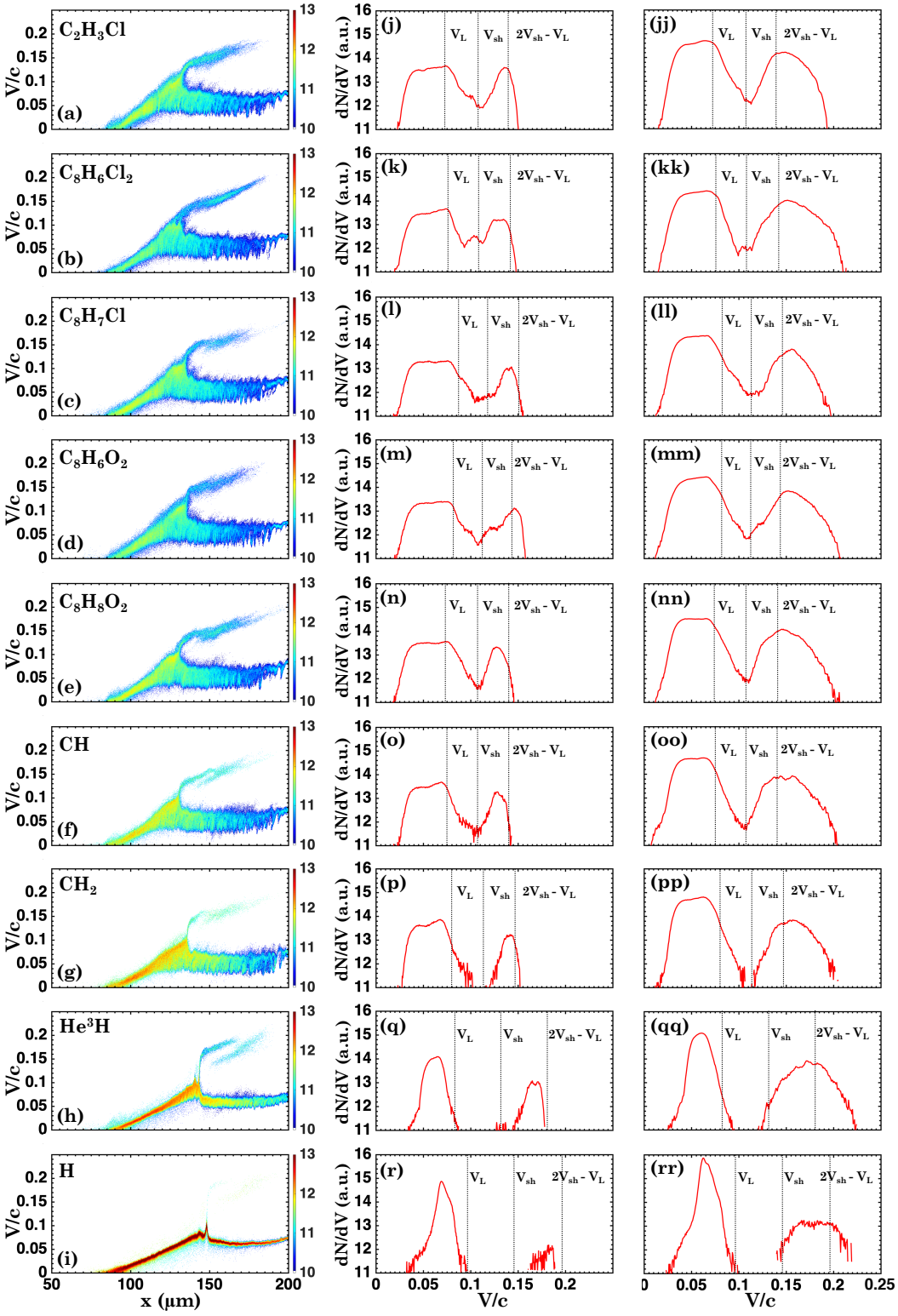


FIGURE 6.8: (a)-(i) The proton phase-space in different target materials at $t = 4.0$ ps. The velocity spectrum of the reflected protons taken (j)-(r) at $\Delta x = 3$ μm in the upstream region and (jj)-(rr) in the whole upstream region at $t = 4.0$ ps.

columns correspond to the proton phase-space, the velocity spectrum taken at $\Delta x = 3$ μm region ahead of the shock front, and the velocity spectrum taken in

the whole upstream region, respectively. As we stated previously, all the protons that satisfy Eq. (6.14) are reflected to a velocity $2V_{sh}$-V_L by the electrostatic potential, ϕ at the shock front. For the target with the lowest <Z/A> (C_2H_3Cl), a considerably large number of protons satisfy Eq. (6.14) when compared to the highest <Z/A> target (pure H). As a result, a large number of protons are accelerated in C_2H_3Cl as compared to the pure H. This can be inferred by comparing Figs. 6.8(a), 6.8(j) and 6.8(jj) with Figs. 6.8(i), 6.8(r) and 6.8(rr) at $t = 4.0$ ps. The maximum velocity of the reflected protons from the shock front is expressed as $2V_{sh}$-V_L. The velocity $2V_{sh}$-V_L increases with <Z/A>, this is directly correlated to the large V_{sh} in high <Z/A> plasmas. The $2V_{sh}$-V_L agrees relatively well with the velocity of the reflected protons. Therefore, the protons are accelerated via the CSA mechanism.

The number of the reflected protons are increased considerably in lower <Z/A> plasma in comparison to the higher <Z/A> as shown in Fig. 6.9(a). This dependence can be clarified by considering the number of protons present in the upstream expanding plasma (dN/dV_{exp}) with a velocity component, V_L.

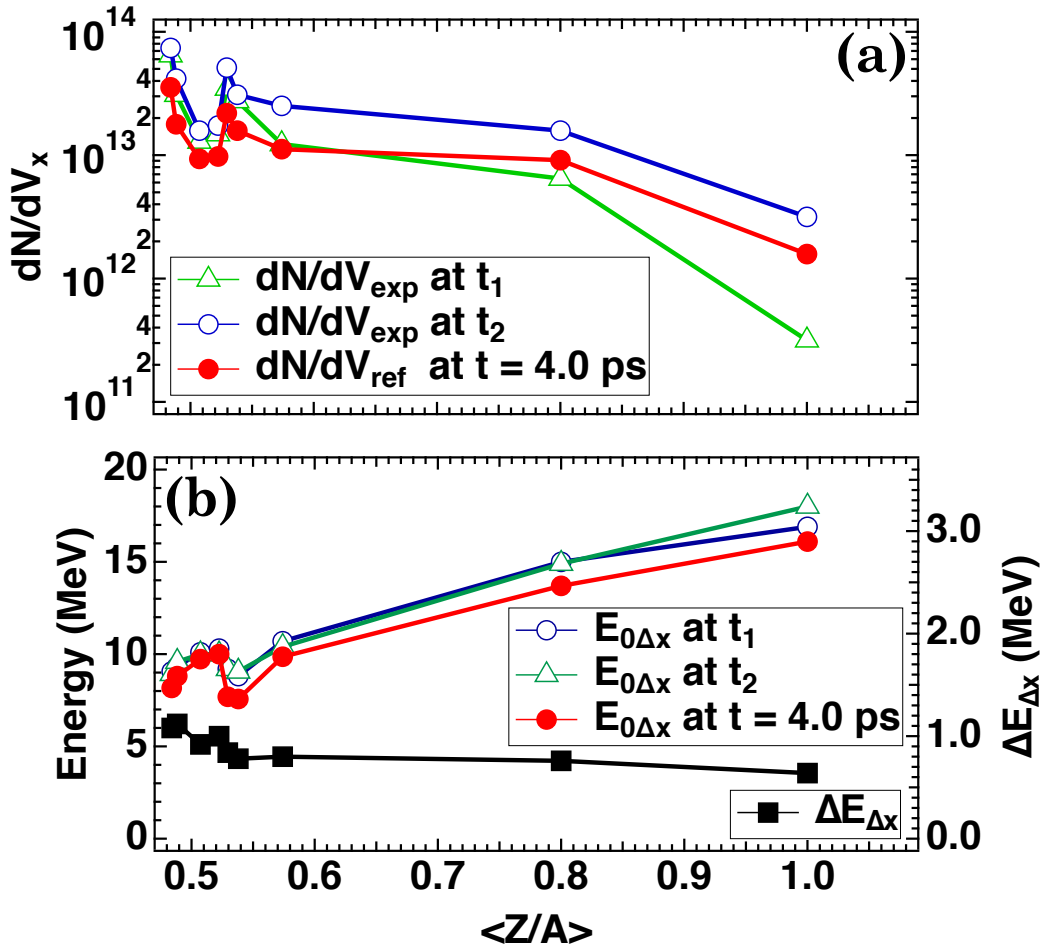


FIGURE 6.9: (a) The dN/dV_{ref} at $t = 4.0$ ps and dN/dV_{exp} at t_1 and t_2 taken at $\Delta x = 3$ μm in the upstream region. (b)The peak energy of the reflected protons $E_{0\Delta x}$ measured at $\Delta x = 3$ μm in upstream of the shock front (as shown by vertical dotted lines in Fig. 6.7) as function of <Z/A> at $t = 4.0$ ps.

When protons are reflected by a shock front-associated electric field E_{sh}, the change in the velocity dV in time Δt is expressed as

$$dV = 2(V_{sh} - V_L) = \left(\frac{eE_{sh}}{m_p}\right)\Delta t. \tag{6.15}$$

Now let's consider the case of C_2H_3Cl plasma, at $t_1 = 3.25$ ps, dV = 0.0708c and $E_{sh} = 8.4\times10^{11}$ Vm^{-1}. By using all these values in Eq. (6.15) gives the time taken $\Delta t = 0.68$ ps ($t_1 + \Delta t = 3.93$ ps) by the upstream expanding protons to gain a velocity $dV = 2(V_{sh}-V_L)$. Similarly, at $t_2 = 3.5$ ps, $\Delta t = 0.66$ ps ($t_2 + \Delta t = 4.16$ ps) is obtained. Therefore, the optimum timing to observe the reflected protons at $t = 4.0$ ps is between 3.25 ps (t_1) and 3.5 ps (t_2). Figure 6.9(a) indicates the dN/dV_{exp} at the t_1 and t_2 and dN/dV_{ref} at $t = 4.0$ ps as function of <Z/A>. The dN/dV_{exp} and dN/dV_{ref} agree very well with each other.

The velocity of the reflected protons at $t = 4.0$ ps is $2V_{sh}-V_L+\delta V_0$, where

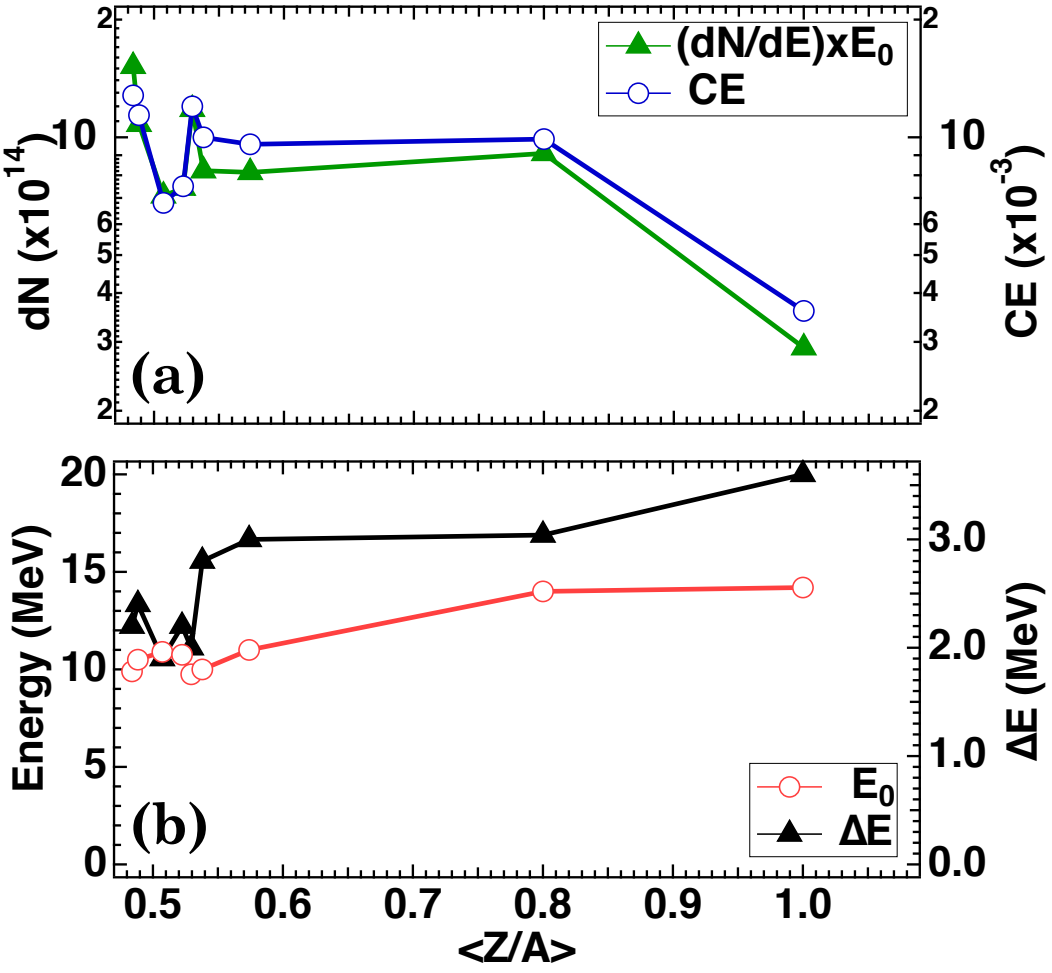


FIGURE 6.10: <Z/A> dependence of (a) $(dN/dE)E_0$, and the laser to reflected protons conversion efficiency (CE), (b) the peak energy of the reflected protons E_0 and their energy spread ΔE_0 taken in the whole upstream region at $t = 4.0$ ps.

δV_0 is the change in the expanding protons velocity caused by the non-oscillating component of E_{TNSA} in time Δt. The energy of the shock-reflected protons is determined from V_{sh} and V_L as

$$E = \frac{1}{2} m_p (2V_{sh} - V_L + \delta V_0)^2. \tag{6.16}$$

As we explained previously, the protons reflected from the shock at t_1 and t_2 gain a velocity $2(V_{sh} - V_0)$ at $t = 4.0$ ps. The energy (E_0) at the peak of the reflected protons distribution and their energy-spread (ΔE_0) are estimated by fitting a Gaussian distribution of form

$$f(E) \propto \exp\left\{ - \frac{(E - E_0)^2}{(\Delta E)^2} \right\}. \tag{6.17}$$

The energy calculated at t_1 and t_2 by using Eq. (6.16) agrees relatively well with $E_{0\Delta x}$ at $t = 4.0$ ps as shown in Fig. 6.9(b), where subscript Δx indicates that the energy spectrum of the reflected proton is taken at $\Delta x = 3$ μm region ahead of the shock front. The energy-spread of these reflected protons, $\Delta E_{0\Delta x}$ decreases with increasing <Z/A>. This is because a very narrow spectrum of the dN/dV_{exp} proton satisfy the V_L in the large <Z/A> material plasmas as compared to the lower <Z/A> plasmas. This can be seen in Fig. 6.8.

The energy distribution of the shock-reflected protons multiplied by E_0, i.e., $(dN/dE)E_0$ is presented as a function of <Z/A> in Fig. 6.10(a). This distribution is compared to the laser-to-reflected proton conversion efficiency (CE) in the same figure. Material with lowest <Z/A> (C_2H_3Cl) shows that the number of reflected protons and CE increased by order of magnitude higher in comparison to a pure proton target with highest <Z/A>. It can be seen in Fig. 6.10(a), both the number of reflected protons and CE are in qualitative agreement with each other, and the number of reflected protons are believed to play an essential role for higher CE in lower <Z/A> material plasmas.

Figure 6.10(b) represents the reflected proton energy E_0 and their energy-spread ΔE_0 taken in the whole upstream region. The E_0 and ΔE_0 are calculated by fitting Eq. (6.17) to the reflected proton distribution. E_0 and ΔE_0 are slightly larger than $E_{0\Delta x}$ and $\Delta E_{0\Delta x}$ as shown in Figs. 6.9(b) and 6.10(b) respectively. Simulations show that the some of protons are accelerated from the front side of the target by hole-boring process. These protons have a different velocity distribution and lower energies compared to the shock-reflected protons, which results in the larger energy spread. Evidence of this seen in Figs. 6.8(f)-6.8(i).

The Material dependence of the number of the shock-reflected protons (dN/dV_x) could be determined with the help of the shock velocity (V_{sh}/c), lower threshold (V_L/c) velocity, and by the difference in these velocities (V'_{df}/c). This dependency is shown in Fig. 6.11. In other words, the larger the number of protons satisfying Eq. (6.14) results in a larger number of protons accelerated via CSA mechanism. Thus, the dN/dV_x depends on the V_{sh}/c, ϕ, and V_L/c. As can be seen from Figs. 6.11(a) and 6.11(b), the decrease in V_{sh}/c and V_L/c results in the increase in the dN/dV_x. The difference between the velocities as in $(V_{sh} - V_L)/c$ is expressed as $V'_{df} = \sqrt{2e\phi/m_p}$. Even for the larger value of

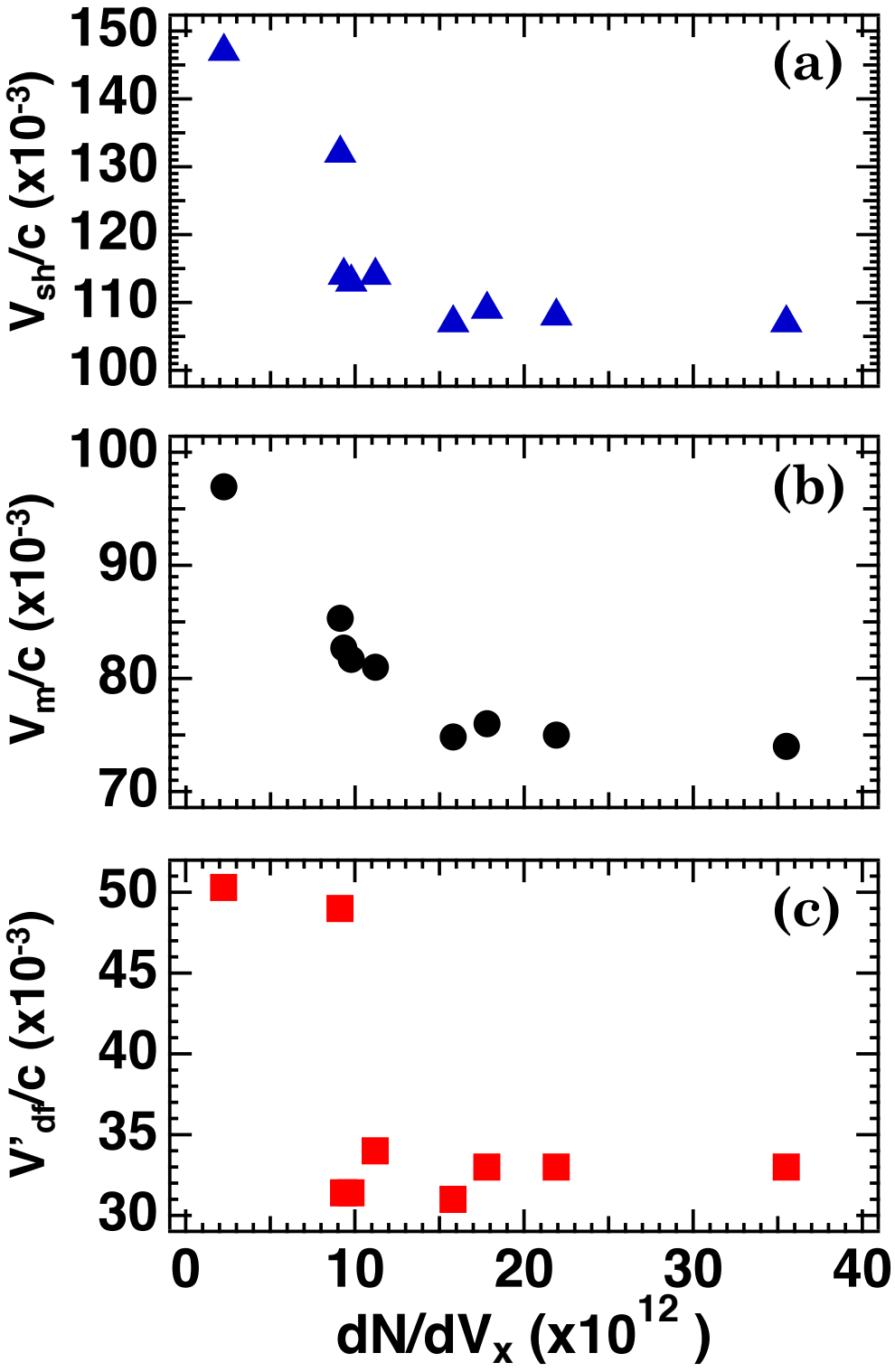


FIGURE 6.11: The variation of (a) shock velocity (V_{sh}/c), (b) lower threshold (V_L/c), and (c) V'_{df}/c = (V_{sh} - V_L)/c as function of the number of the reflected protons (dN/dV_x) in different target materials.

V'_{df}, the dN/dV_x are smaller, as shown in Fig. 6.11(c). The number of reflected protons in different material plasmas depends on the V_L and V_{sh}. As a

result, the most important parameter for the number of the accelerated protons via CSA mechanism is the number of the upstream expanding protons with a velocity equal and larger than V_L. This shows the ability of CSA mechanism to efficiently accelerate high flux and narrower energy distribution proton beams using the lower <Z/A> material compared to the pure H.

6.4 Summary

The electrostatic collisionless shock is driven by the interaction of the high-intensity laser with relativistic near-critical density plasma. A charge imbalance electrostatic field results in a sharp electrostatic potential at the shock front, which reflects the upstream expanding protons. The electron temperature is the same for all target material plasmas. The temporal evolution of electron temperature can be very well fitted with a sigmoid function with a derivative peaking at $t = 1.75$ ps. The number of reflected protons in different material plasmas depends on the lower bound velocities (V_L) for proton reflection and shock velocities. Lower values of V_L always result in the high proton flux. Protons with high flux and narrower energy spread can be produced using the lower <Z/A> materials.

Chapter 7

Electrostatic Ion Two-stream Instability

7.1 Introduction

In the field of plasma, depending on the interactions with medium and driving mechanism, either wave can grow or damp. Plasmas are rare and highly unstable in thermodynamic equilibrium. In other words, a source of free energy comes into picture from a non-Maxwellian velocity distribution which needs to be dissipated [154]. In order to turn over a non-Maxwellian velocity distribution into a Maxwellian's distribution, plasma must allow this free energy to transform into some other energies. This is the place where the instabilities in plasmas play an essential role.

The normal modes of Instability can be explained with the help of relationships between the angular frequency (ω) and wavenumber (k) [154]. Similar to a medium which has its own dispersive properties, every mode of the wave excited by the free energy has its own dispersive properties. The stable mode of the system is coupled with the temporal and spatial growth of the instability. In other words, instability goes through the radiations to dissipate the source of free energy in the system. Thus one of the essential transfer mechanism to dissipate the source of free energy is the instabilities in the plasma. Owing to the fact that the instability influenced by both ω and k, one can expect that there are going to be different scale or range depending on the system. This means, depending on the size of wave number (k), the instability can described as 'microinstabiltiy', i.e. large k (small wavelength), and 'macroinstability', i.e. small k (large wavelength). There are many instabilities exists in the plasma. In this chapter, we will discuss one of the essential instability, known as the electrostatic ion two-stream instability (EITI).

Plasma microinstabilities play an essential role in the dynamics of collisionless shocks [155–157]. The linear theory of electrostatic ion two-stream instability (EITI) in unmagnetized plasmas are examined by several authors [158–161], and also EITI is known by several other names such as 'ion-ion acoustic instability' or 'ion-ion streaming instability.' It has been shown that, when the two ion populations drift with a relative velocity with respect to each other, it results in the excitation of electrostatic ion two-stream instability [162–165]. Garry and Omidi [166] have carried out the numerical solution for the electrostatic

dispersion equation and detailed discussion of the properties of ion-ion acoustic instability. An instability excited by the relative drift between the two ion populations has been also observed in the upstream of different shocks such as bow shock [167], interplanetary shock [168], Earth magnetotail [169], and in the space plasmas such as solar wind [167, 170], Earth's magnetosheath [171] etc. The ion two stream instability can be excited in the foreshock of SNRs shocks [172, 173]. In case of electrostatic collisionless shock, since the reflected ions are present ahead of the shock front, the electrostatic ion two-stream instability can develop. The wave vector of the instability propagates obliquely to the propagation direction or even perpendicular to it [162, 163] thus, a multi-dimensional analysis is needed. Two-dimensional study of electrostatic ion two-stream instability ahead of the shock front showed that the structure of electrostatic shock is significantly affected by this instability [174]. Numerical simulation for EITI has demonstrated that, the electric field generated by this instability results in the strong fluctuation in the ion densities and affects the shock dynamics; destroy the shock itself [175]. Numerical investigation and linear analysis for EITI in the foot region of collisionless shock show that the fastest growing mode is not the ion acoustic instability, but the highly oblique ion two-stream instability, and protons are heated preferentially perpendicular to the shock normal direction [176]. The experimental demonstration for ion-ion two-stream instability has shown that the growth rate of the instability is significantly affected by the relative charge-to-mass ratio of the species [177]. The experimental investigation done by Ross et al. [178] has shown that the ion two-stream instability is responsible for the collisionless ion heating. To our best knowledge, most of the previous work has focused on shock formation [179–181] and ion heating [175, 176, 178]. This is the first investigation on the material dependence of EITI on CSA [152].

First and the foremost, it is crucial to understand what leads to the excitation of EITI in plasmas. The EITI occurs within the plasma when the two ion populations with different charge-to-mass ratios, <Z/A> drift with respect to one another under the action of non-oscillating electrostatic field (E_{TNSA}). This points to the non-uniform charge density perturbation that grows exponentially in the amplitude; identified as the unstable mode of the instability. When unstable mode occurs, the modulation in the charge density or electric field perturbation can be characterized by the wave number, k, and has an angular frequency, ω, which has the real and imaginary parts such as

$$\omega(k) = \omega_r(k) + i\omega_i(k), \tag{7.1}$$

where ω_r indicates the real part of the angular frequency of the perturbation, while the ω_i represents the growth rate or imaginary part of the angular frequency, which is the function of k. Depending on the value of ω_i such as $\omega_i > 0 (< 0)$ the amplitudes of the perturbations grow (decay) exponentially with time. Although, it should be noted that, to trigger the instabilities in plasma, the solutions to the dispersion relation with $\omega_i > 0$ is not sufficient. The system of plasma needs a source of free energy; otherwise, the growth of instability convey the hypothesis that the system is an unphysical interpretation.

Based on the local plasma parameters and source of free energy, several different instabilities are allowed in the intrinsic unstable nature of the plasma. For instance the source of free energy for the excitation of ion acoustic waves in plasmas: electron heat flux [182], cross-field currents [183], the streaming of cold ion beam through a magnetized warm electron background [184], etc. The other instability is the electrostatic ion two-stream instability, where the stream of two ion populations drifts with respect to one another with a finite velocity under the action of electrostatic field. In this chapter, we will discuss the numerical study of EITI in multi-ion species plasma and how EITI has affected ion acceleration via the CSA process [152].

7.1.1 EITI in C_2H_3Cl Plasma

To examine the development of EITI in multi-ion species plasma, we use the same simulation results as we presented in the previous chapter 6. For the sake of simplicity, we restrict our investigation on the development of EITI in C_2H_3Cl plasma only. Figs. 7.1(a) and 7.1(b) represent the spatial distribution of electrostatic field, E_x in the upstream region of C_2H_3Cl plasma. The electrostatic field represented in these figures is averaged over two laser cycles, to avoid the influence of sinusoidal laser fields. The simulation box size is $y = 6$ and 20 μm, respectively. Both cases display a wave-like structure or modulations propagating in the x-direction. It is clear from Figs. 7.1(a) and 7.1(b) the wavelength of these modulations increases in the x-direction. The E_x profile along the x-axis is averaged along the y-axis and overlaid on the phase-space of the corresponding proton velocity distribution in the upstream shown in Fig 7.1(c). The modulation in E_x shows comparative correlation with the proton phase-space distributions. As we explained earlier, the small perturbations/modulations in charge density or electric field are excited by electrostatic ion two-stream instability in plasmas. These modulations are excited by the relative drift velocity (V_d) between the two ion populations in plasmas with multi-ion species. Our simulations show that this relative drift is driven by the E_{TNSA} in the upstream plasma which results in slower moving heavier ions with low <Z/A> and faster-moving protons with high <Z/A>.

7.1.2 Velocity Distribution of Expanding Ions

Temporal evolution of the velocity distribution of the upstream expanding ions, dN/dV_x in the C_2H_3Cl plasma are displayed in Figs. 7.2(a) and 7.2(b). These plots were taken at $\Delta x = 3$ μm region just ahead of the shock at $t = 2.0$ ps, and 4.0 ps respectively. Initially, V_d is small, and the instability has not established. As time evolves, V_d increases, which leads to a growth in the instability. This results, as shown in Fig. 7.2(b), in a high-velocity tail in the C-ion and a low-velocity component to the proton distributions. We note that the chlorine distribution does not broaden in time. This observation suggests that the broadening of proton distributions discussed in relation to Fig. 6.8 results from the EITI.

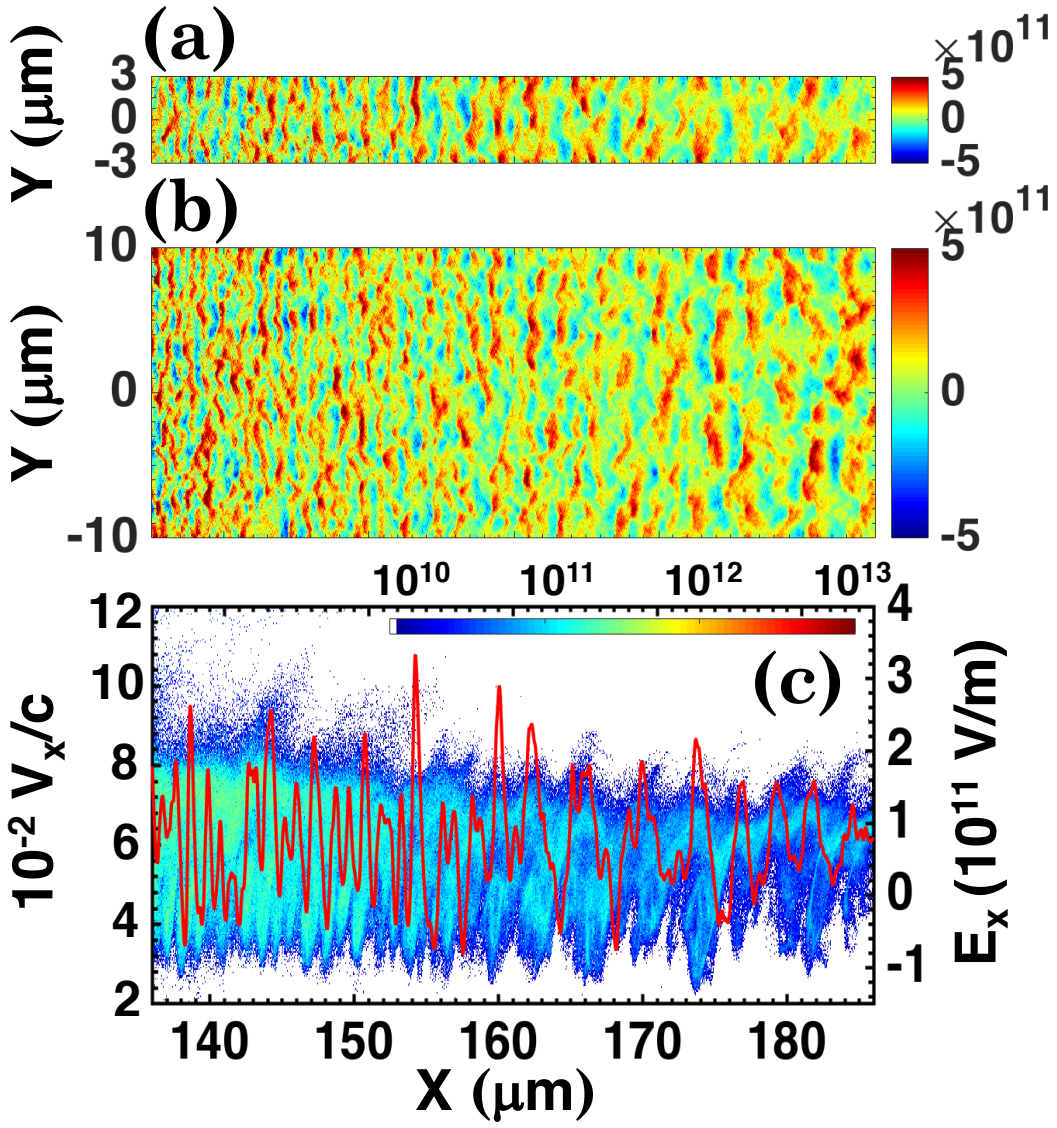


FIGURE 7.1: 2D electrostatic field (E_x) distribution averaged over two laser-cycles in the upstream region at t = 4.0 ps in C_2H_3Cl for the simulations box size of (a) y = 6 μm and (b) y = 20 μm. (c) Phase-space of the upstream expanding protons and 1D profile of E_x [taken from [152]].

The shape of the proton velocity distribution is characterized by using the sum of three 1D shifted Maxwellian's velocity distribution of form

$$f(\mathrm{E}) \propto \exp\left\{-\frac{\mathrm{m}_p(\mathrm{V}-\mathrm{V}_m)^2}{\mathrm{T}_i}\right\}, \tag{7.2}$$

throughout all time. Here, m_p is the mass of the proton, V is the expanding ion velocity, V_m is the mean of the expanding ion velocity, V_0, and T_i is the ion temperature. Therefore, a sum of multiple 1D shifted relativistic Maxwellian's is used to fit the upstream expanding velocity distribution of protons taken at Δx = 3 μm region ahead of the shock front in C_2H_3Cl plasma. The peak

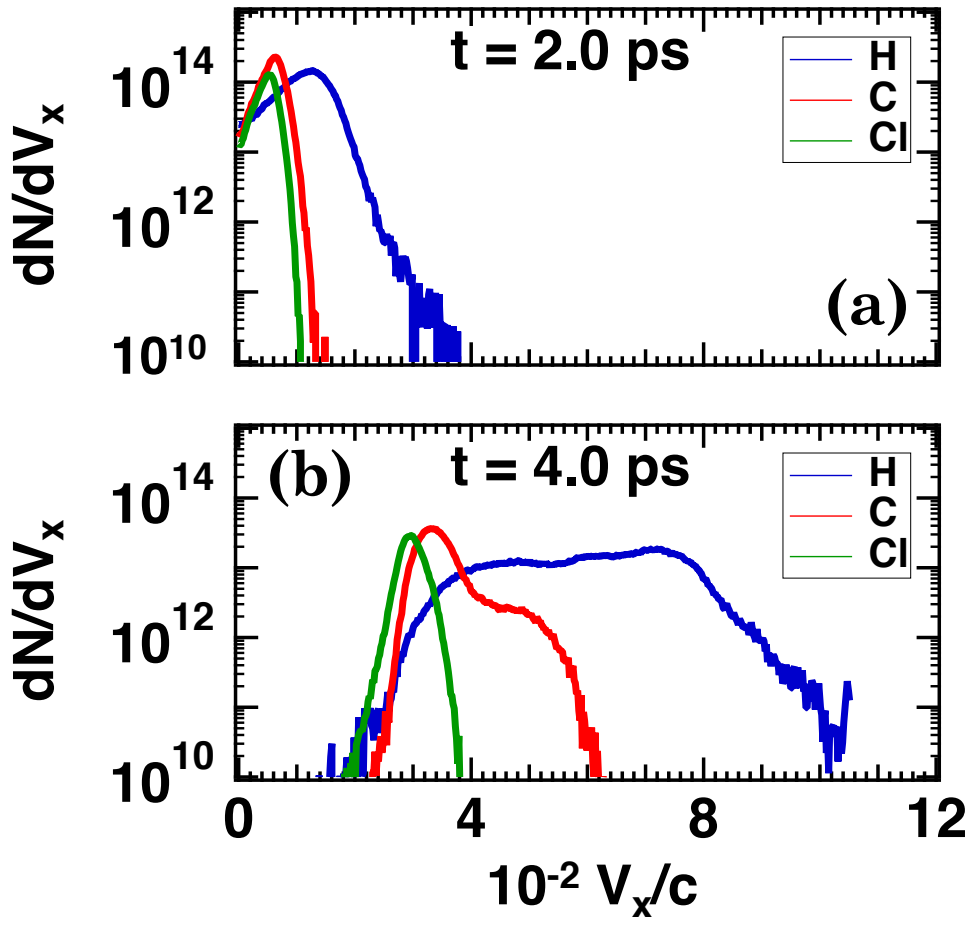


FIGURE 7.2: Velocity spectrum of the expanding ions taken at $\Delta x = 3$ μm in the upstream region at (a) t = 2.0 ps and (b) t = 4.0 ps in C_2H_3Cl [taken from [152]].

number density, velocity, and temperature of the three fitted Maxwellian's are represented in Figs. 7.3(a)-(c). In Fig. 7.3(a), the dN/dV_L, dN/dV_H, and dN/dV_M denotes the number density at the peak of the fitted Maxwellian's for lower, higher, and mean values of the velocity distribution in the upstream region. It is clear from Fig. 7.3, at $t = 1.50$ ps, the velocity of the upstream expanding protons is small, and a large number of protons correspond to the lower velocity component, and a small number of upstream protons corresponds to the maximum velocity component, and their temperature is nearly same. After the laser peak is gone, a few protons in the upstream region are accelerated by the TNSA field, which leads to the broadening of the velocity distribution. At $t = 1.75$ ps, a secondary Maxwellian distribution with very low number density and low temperature is fitted at V_M. By $t = 2.75$ ps the number at the peak of dN/dV_L, dN/dV_H, and dN/dV_M become equal, although the velocity and temperature of each fitted Maxwellian keep increasing. With the increase in time, the number density of each Maxwellian remains nearly constant, as shown in Fig. 7.3(a). The velocities of the all fitted Maxwellian's keep increasing with time. The temperature of V_L and V_H remains the same after $t = 2.75$ ps, but

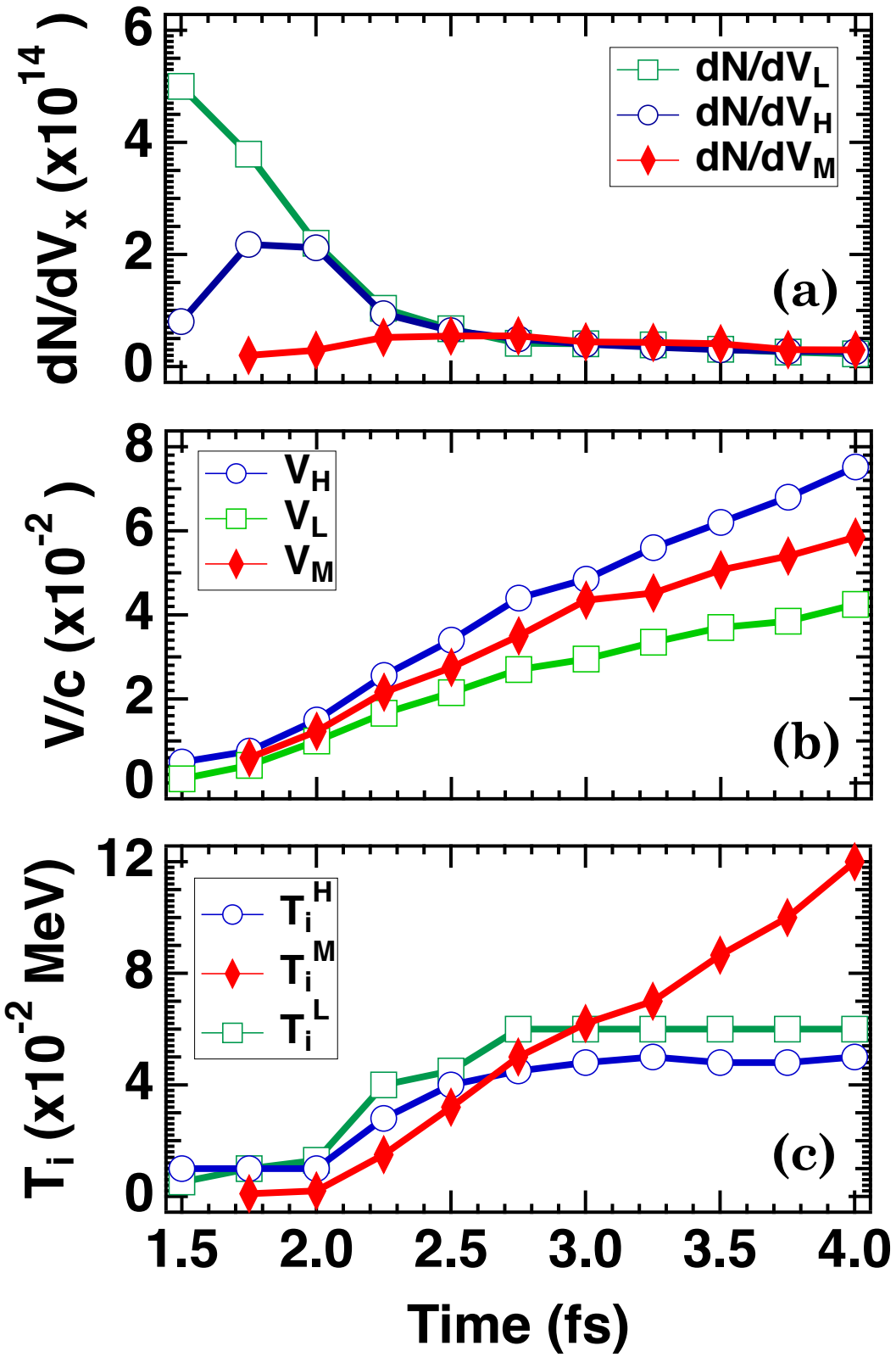


FIGURE 7.3: The time evolution of (a) peak number density, (b) velocities, and (c) ion temperature of the 1st (L), 2nd (M), and 3rd (H) fitted 1D shifted Maxwellian in C_2H_3Cl plasma at $t = 4.0$ ps.

the temperature of the central Maxwellian keep increasing, as shown in Fig. 7.3(c). The shape of the upstream expanding protons and rise in temperature of the central Maxwellian distribution remains an open question.

Temporal evolution of the velocity at the peak of the dN/dV_x distribution for Cl-ions, V_{Cl} (from the C_2H_3Cl target) is plotted in Fig. 7.4. V_{Cl} shows a logarithmic dependence with time, indicating that V_{Cl} is determined by the upstream E_{TNSA} as discussed in subsection 6.3.2. By taking a derivative of a fit to the V_{Cl} distribution with $<Z/A> = 0.429$, we infer that the time-dependent E_{TNSA} evolves with a $1/t$ dependence as shown in Fig. 7.4. The temporal variations for V_{Cl} and E_{TNSA} relationship described by Mora [110]. The time dependence of the C-ion velocity (V_C) at the peak of dN/dV_x agrees well with calculations of V_C based on the concluded E_{TNSA} and $<Z/A> = 0.5$ (V_{C-TNSA} [see Fig. 7.4]). At $t = 2.5$ ps, a high-velocity tail (V_C^H) appears in V_C. This results from acceleration by an electric field associated with the EITI. The calculated velocity for H-ions from E_{TNSA} (V_{H-TNSA}) with $<Z/A>=1$, which gives the maximum possible velocity for H-ions caused by E_{TNSA}, is included for the comparison in Fig. 7.4. We approximate the simulated velocity distributions for protons as a sum of the three 1D-shifted Maxwellian's as described

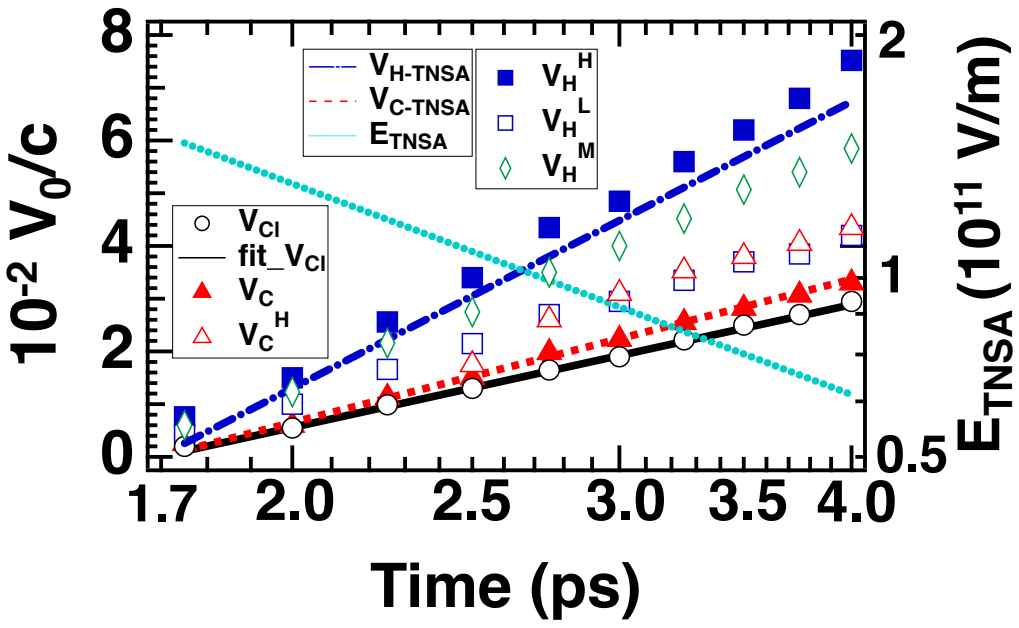


FIGURE 7.4: Time evolution of the expanding ion velocities in C_2H_3Cl. The velocity of Cl-ions V_{Cl} (open circles) is derived from the peak of the velocity spectrum (dN/dV_{Cl}) taken at $\Delta x = 3$ μm in the upstream region and fitted to logarithmic curve V_{Cl} (solid line). E_{TNSA} (dotted line) is derived from V_{Cl} and follows a 1/t dependence. Temporal variation of V_C (filled triangles) agrees well with the calculated V_C (V_{C-TNSA}, dashed line) from V_{Cl}. V_{C^H} (open triangles) shows the high-velocity tail of C-ions, which appears at $t = 2.5$ ps, and overlaps with the lower-velocity (V_{H^L}) (open rectangles) component of H-ions. V_{H^H} (filled rectangles) represents the higher-velocity component of H-ions, which is larger than the velocity calculated from E_{TNSA} (V_{H-TNSA}, dot-dashed line) [taken from [152]].

earlier. These velocities, the lower (V_H^L), mean (V_H^M), and higher (V_H^H) velocity Maxwellian distributions are shown in Fig. 7.4 [also see Fig. 7.3]. We note that V_C^H and V_H^L represent the EITI accelerated and decelerated C-ion and proton populations, respectively, and these populations have similar velocities. This occurs as an additional EITI develops due to the relative drift between the shock reflected proton population moving at approximately $2V_{sh}$ - V_0, through the upstream expanding proton population moving at V_0. This further increases the number of protons satisfying the condition for CSA.

7.2 EITI in multi-ion species plasma

In cold plasma approximation, the dispersion relation of EITI is given by [176]

$$1 + \frac{1}{k_x^2 \lambda_{De}^2} = \frac{\omega_{p1}^2}{\omega^2} + \frac{\omega_{p2}^2}{(\omega - k_x V_d)^2}. \tag{7.3}$$

Here k_x is the wave number in the x-direction, λ_{De} is the electron Debye length, ω_{p1} and ω_{p2} are the proton and heavy ion plasma frequencies, respectively, and V_d is the relative drift velocity between the two ion populations.

In multi-ion species plasma, ω_{p1} is the proton plasma frequency, ω_{pp} and ω_{p2} is the heavy-ion plasma frequency, as ω_{p2} is the carbon plasma frequency ω_{pc} for C_2H_3Cl and CH.

7.2.1 Analytical Solution

For C_2H_3Cl at t = 4.0 ps, the maximum amplitude of the modulation in E_x in the region of x = 135 - 145 μm occurs at $k_x = 4.7\times10^6$ m^{-1} as shown by dashed line in Fig. 7.5(a). In the upstream region of plasma at $x = 140$ μm, the electron temperature and densities are $T_e = 2.0$ MeV and $N_e = 6.5\times10^{20}$ cm^{-3}, respectively, which gives $\lambda_{De} = 0.4$ μm. This results in $k_x\lambda_{De} > 1$, enabling us to neglect the second term on the left-hand side of Eq. (7.3).

Equation (7.3) has an unstable solution with the maximum growth rate of

$$\gamma_{\max} = \frac{\omega_{pc}}{2} \qquad at \qquad k_x = \frac{\sqrt{3}\omega_{pc}}{V_d}. \tag{7.4}$$

At $x = 140$ μm, the carbon ion and proton number densities are $N_C = 4\times10^{19}$ cm^{-3} and $N_p = 1.3\times10^{20}$ cm^{-3}. This gives the equal frequencies for carbon and protons, i.e. $\omega_{pc} = \omega_{pp} = 1.5\times10^{13}$ sec^{-1}, respectively. A relative drift between the upstream expanding protons and C-ions is, $V_d = V_H^H - V_C = 0.042$c at t = 4.0 ps as shown in Fig. 7.4. The value of k_x can be calculated by using all these values in Eq. (7.4), i.e. $k_x \sim 2.1\times10^6$ m^{-1}, which agrees relatively well with the value of $k_x = 4.7\times10^6$ m^{-1} extracted from power spectrum taken in region $x = 135-145$ μm as shown in Fig. 7.5(a). As this instability exists between the upstream expanding heavy-ions (C-ions) and protons, thus we refer to this instability as 'heavy-ion' EITI.

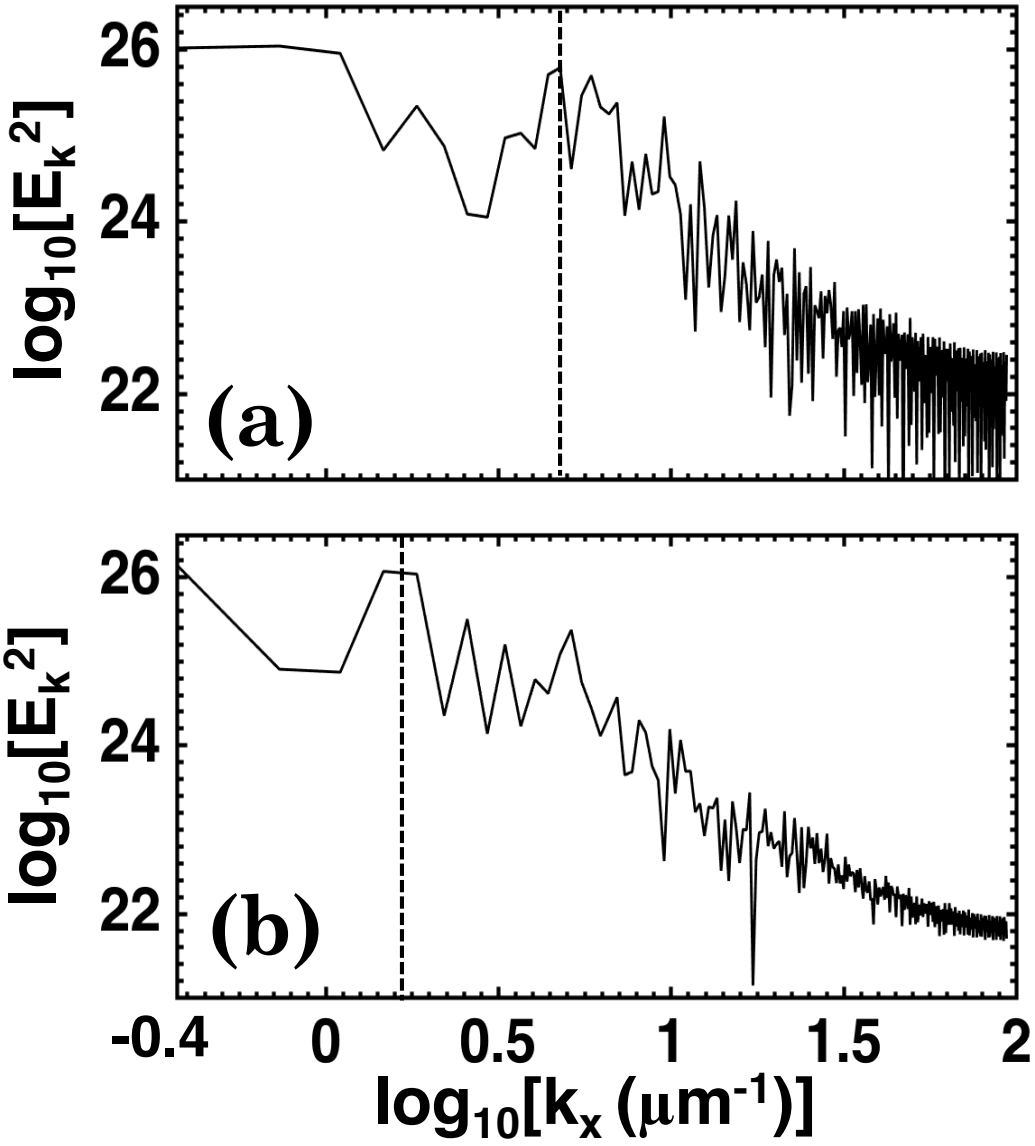


FIGURE 7.5: Derived power spectrum of electrostatic field, E_x at t = 4.0 ps taken in the region of (d) x = 135 - 145 μm and (e) x = 165 - 175 μm in C_2H_3Cl plasma [taken from [152]].

At $x = 160$ μm, the carbon number density, $N_C = 1\times10^{19}$ cm^{-3}. This gives heavy ion plasma frequency, $\omega_{pc} = 7.2\times10^{12}$ sec^{-1}, and $V_d = 0.040$c at $t = 4.0$ ps. Similarly, by using all these values in Eq. (7.4), $k_x \sim 1.0\times10^6$ m^{-1}, which is comparable to $k_x \sim 1.6\times10^6$ m^{-1} as shown in simulation in Fig. 7.5(b). As a result, it is clear from Figs. 7.5(a) and 7.5(b), the value of k_x decreases as x increases. This is because the value of maximum growth rate (γ_{max}) depends on the heavy-ion or proton plasma frequency (refer Eq. 7.4), which is a function of plasma density. The plasma density on the rear-side of the target decreases exponentially with increasing x as shown in Fig. 6.1(b).

At t > 2.5 ps, the number of protons reflected by the shock front increases, which contributes to the excitation of the EITI between the expanding and the

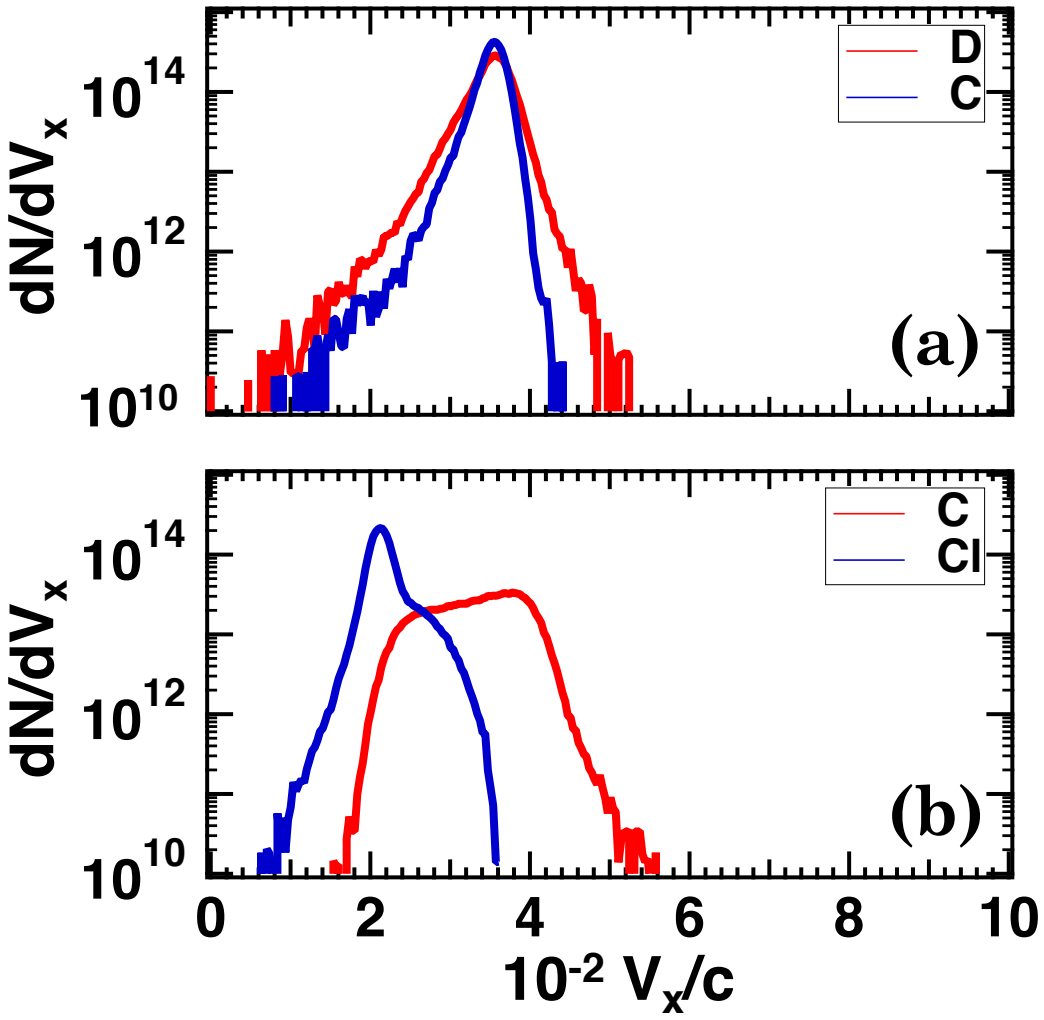


FIGURE 7.6: Velocity spectrum of the expanding ions in (a) CD and (b) CCl_2 targets taken at $\Delta x = 3$ μm in the upstream region at t = 4.0 ps [taken from [152]].

reflected protons. This is referred to as reflected-proton EITI. This leads to the generation of a high-velocity tail in V_H^H in the upstream plasma. In the case of reflected-proton EITI, $\omega_{p1} = \omega_{pp}$ and ω_{p2} is the reflected proton plasma frequency ω_{pref}. As shown in Fig. 6.8, the number of reflected protons is smaller than that of the expanding protons even at $t = 4.0$ ps. Hence, $\omega_{pref} < \omega_{pp}$. The maximum growth rate of reflected-proton EITI [176] is given by

$$\gamma_{max} = \left(\frac{3\sqrt{3}}{16}\frac{N_{ref}}{N_{exp}}\right)^{\frac{1}{3}} \omega_{pp} \qquad at \qquad k_x = \frac{\sqrt{3}\omega_{pp}}{V_d^r}. \tag{7.5}$$

Here, N stands for density and subscripts 'exp' and 'ref' denotes the expanding and reflected proton populations, respectively. The relative drift between the reflected and expanding protons is $V_d^r = 0.064$c at t = 4.0 ps. Therefore, $k_x \sim 6.8\times10^5$ m^{-1}, which is comparable to the k_x value for the maximum growth rate of heavy-ion EITI by a factor of 0.68. As a result, this suggests both that

heavy-ion and reflected-proton EITIs occur with similar growth rates and wave numbers. Thus, it is difficult to distinguish between heavy-ion and reflected-proton EITI, i.e., HI- and RP-EITI.

V_{H-TNSA} or the maximum possible velocity of H-ions accelerated by E_{TNSA} in C_2H_3Cl is shown in Fig. 7.4. We infer that a large number of protons is accelerated by the wave electric field of reflected-proton EITI and obtain the expansion velocity V_0 larger than V_{H-TNSA}. This acceleration generates a significant number of expanding protons with the velocities larger than V_L and results in the enhancement of the shock-accelerated protons. Simulation studies done by Grassi et al. [185], have shown that the development of ion turbulence in H plasma leads to the heating of upstream ions, which allows a fraction of ions to exceed the threshold for ion reflection from the shock front.

To confirm the effect of <Z/A> on EITI, PIC-simulations with the same laser and density properties used throughout are compared to fully ionized carbon deuterium (CD) plasma. As shown in Fig. 7.6(a), since both C and D-ions have the same <Z/A> = 0.5, both ions are accelerated by E_{TNSA} in the upstream plasma, and there is no relative drift between them, as in, $V_d = 0$. Therefore, no instability is excited, and no broadening of the upstream ions occurs. In multi-ion plasmas, a high-velocity tail and a low-velocity component appear in the smaller and larger <Z/A> ions, respectively. Figure 7.6(b) represents upstream ion velocity distribution for CCl_2 plasma with fully ionized C and $Z_{Cl} = 10$. A high-velocity tail in Cl-ions and a low-velocity component of C-ions appear because of heavy-ion EITI.

7.2.2 Exact Solution

In order to properly explore the EITI between the two ion populations in upstream plasma, a MATLAB program is used to solve the dispersion relation for the roots numerically. Equation (7.3) was rewritten to the 4th order non-linear polynomial and set equal to zero. After finding the roots via MATHEMATICA equation solver, the other variables/constant are used from the PIC simulation results.

Figure 7.7 represents the roots of the dispersion relations for heavy-ion (HI-) EITI calculated from Eq. (7.3) in C_2H_3Cl plasma. Here the second term on the left side is neglected ($1/k_x\lambda_{De} << 0$); at $t = 4.0$ ps, the proton plasma frequency, $\omega_{p1} = \omega_{pp} = 1.51\times10^{13}\ s^{-1}$, the heavy (C) ion frequency $\omega_{p2} = \omega_{pc} = 1.52\times10^{13}\ s^{-1}$, and the relative drift, $V_d = 0.042c$. These values are similar to the ones used for the analytical calculations [152]. For each k_x, there are four roots, two of them are complex numbers. In the figure ω_r and ω_i are plotted as a function of k_x. From these plots, we can find the value of k_x where the growth rate of the instability becomes maximized, ω_i^{max}. In Fig. 7.7(a) the horizontal and inclined dotted lines represent plasma and beam modes. The interaction of the fast plasma mode and the slow beam mode leads to the excitation of the instability, and there are no real solutions in the interaction region. The ω_i becomes maximum at the interaction point as shown in Fig. 7.7(b).

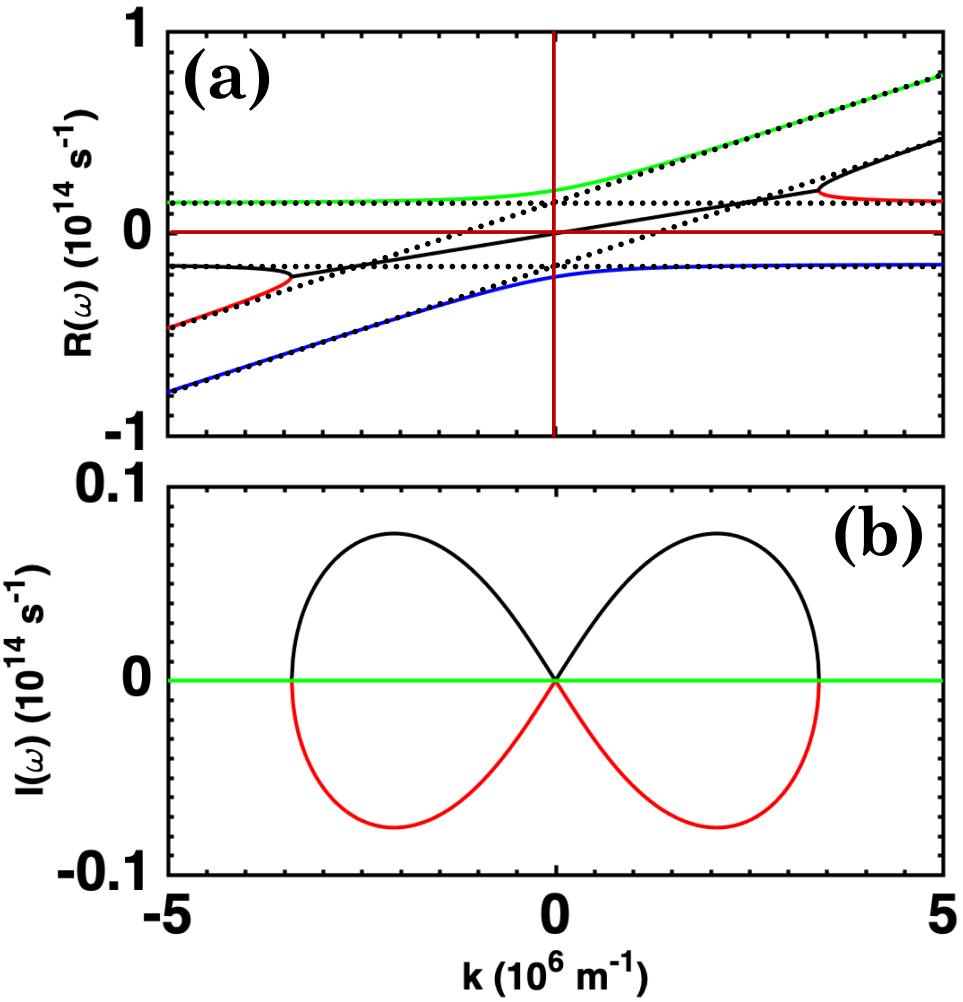


FIGURE 7.7: Electrostatic ion two-stream instability by assuming $1/k_x\lambda_{De} = 0$ in C_2H_3Cl plasma at $t = 4.0$ ps. The positive values of ω represent the unstable mode of the instability. The horizontal and vertical dotted lines indicate the plasma and beam mode respectively. (a) The real (R(ω)) and (b) imaginary (I(ω)) parts of ω as a function of wave number k_x.

We further generalize our calculations by including the effect of $k_x\lambda_{De}$ in Eq. (7.3). This results in the dispersion relation

$$1 = \frac{(N_{i1}/N_e)C_{s1}^2k_x^2}{\omega^2(1+k_x^2\lambda_{De}^2)} + \frac{(N_{i2}/N_e)C_{s2}^2k_x^2}{(\omega - k_xV_d)^2(1+k_x^2\lambda_{De}^2)}. \tag{7.6}$$

Here, C_s is the ion-acoustic velocity and N_i is the ion density. Subscript 1 and 2 denote the two different ion species. The roots of the dispersion relation, ω_r and ω_i with respect to k_x are shown in Figs. 7.8(a) and 7.8(b), respectively. Equation (7.6) shows the excitation of ion acoustic mode for two ion populations. The interaction between the fast plasma mode and slow beam mode occurs at a similar k_x with smaller $\omega_i^{\max}$ as shown in Fig. 7.8(b).

As we interpreted in previous section 7.2.1, two types of EITI exist in the multi-ion species plasma, i.e., heavy-ion EITI (HI-EITI), caused by the relative drift between the heavy and light ions, and reflected-proton EITI (RP-EITI),

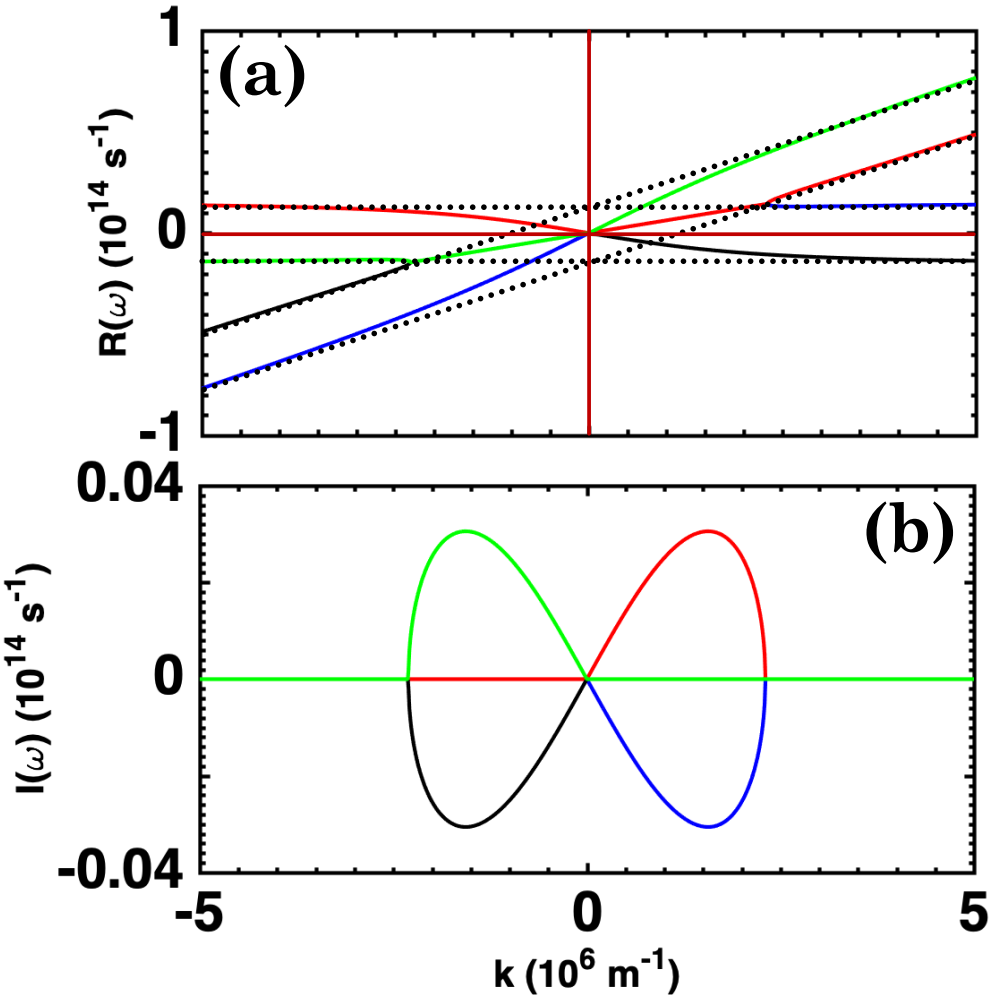


FIGURE 7.8: Electrostatic ion two-stream instability by assuming $1/k_x\lambda_{De} \neq 0$ in C_2H_3Cl plasma at $t = 4.0$ ps. The positive values of ω represent the unstable mode of the instability. The horizontal and vertical dotted lines indicate the plasma and beam mode respectively. (a) The real (R(ω)) and (b) imaginary (I(ω)) parts of ω as a function of wave number k_x.

caused by the relative drift between the reflected and expanding protons. The RP-EITI emerges at $t > 2.50$ ps when the number of the reflected protons increases. This leads to the generation of the high-velocity component in the upstream expanding protons [152]. Since the number of reflected protons are smaller than the expanding protons in the upstream region. The scaling for maximum growth rate for RP-EITI is different from the one for HI-EITI [176]. Figure 7.9 shows the temporal evolution of the $\omega_i^{\max}$ at k_x measured in PIC simulations, calculated analytically, and the solution of Eq. (7.3) in C_2H_3Cl plasma. In order to obtain the analytical results, the unstable solutions for HI-EITI and RP-EITI are used as illustrated by Eq. (7.4) and Eq. (7.5), respectively. To find the exact solutions, a MATLAB code is used to solve the roots of Eq. (7.3). The analytical and exact solutions show that the k_x is maximum earlier and keep decreasing with time for HI-EITI as shown in Fig. 7.9(a). As the shock front propagates in the exponentially decreasing density with time, the value of the k_x always depends on the ion plasma frequency

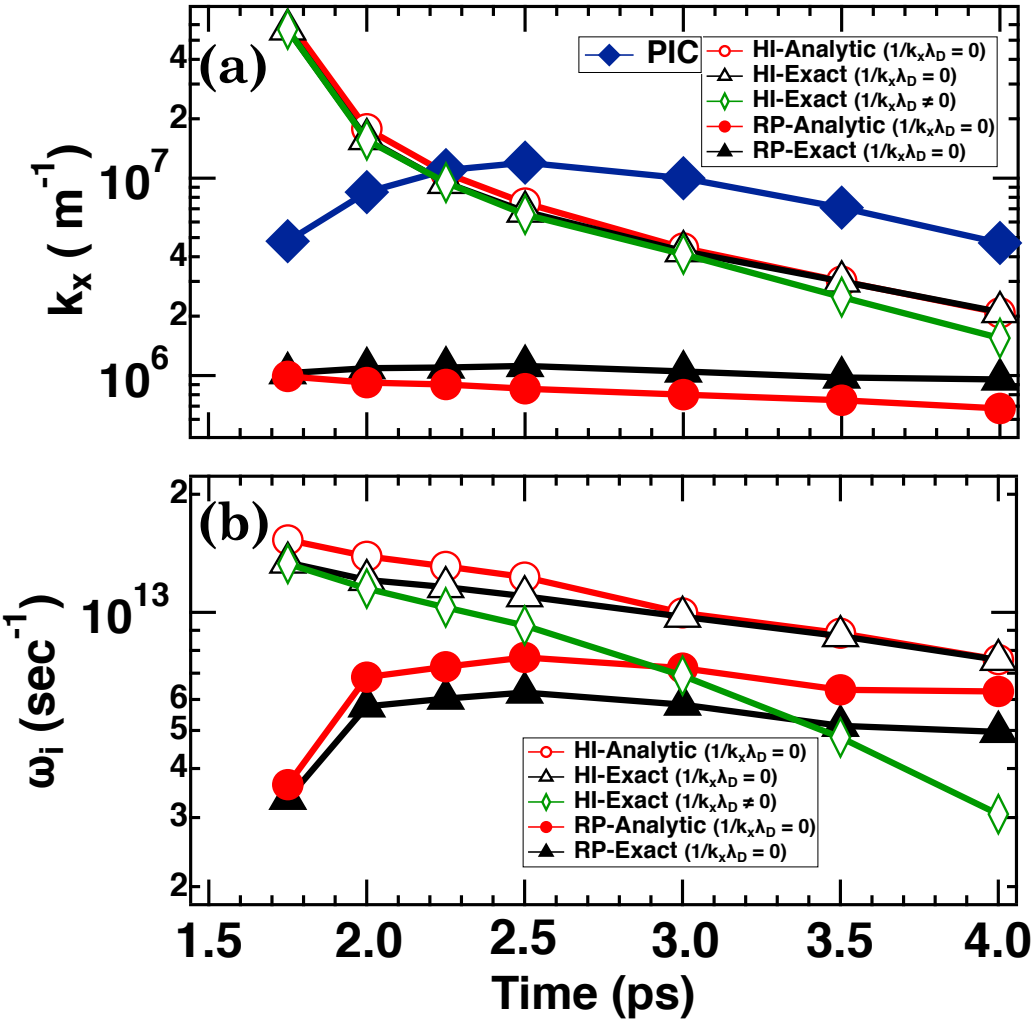


FIGURE 7.9: The temporal evolution of (a) wave number (k_x) (b) growth rate (ω_i) for HI- and RP-EITI, and from the PIC simulations in C_2H_3Cl plasma.

and always calculated ahead of the shock front. As a result, k_x decreases with time. The value of k_x for RP-EITI is nearly the same for analytical and exact solutions. However, the value of k_x measured in PIC simulations, first increases with time (t = 2.5 ps) and later in time it decreases. This is measured by taking the power spectrum of the electrostatic field in the upstream region of the shock front, as shown in Figs. 7.5(a) and 7.5(b). The analytic and exact solutions ($k_x = 0$) for the growth rate for both instabilities, i.e., HI-EITI and RP-EITI are nearly the same. However, the growth rate for the exact solution ($1/k_x\lambda_{De} \neq 0$) decreases faster compared to the exact ($k_x = 0$) and analytical solutions for HI-EITI. This is because the ion-acoustic velocity of proton and C ion populations plays an important role in the EITI, which arises because of the Debye length, λ_{De}. The growth rates for both HI- and RP-EITI are nearly the same at t= 4.0 ps. Therefore, it is difficult to distinguish which instability is dominant. Analytical and exact solutions roughly agree with PIC simulations value of k_x. As we explained in Ref. [35], HI-EITI leads to the broadening of

upstream expanding protons towards the lower velocity, and RP-EITI further broadened their velocity distribution towards the large velocity.

7.3 Summary

In multi-ion species plasmas, a relative drift between two ion populations triggers the electrostatic ion two-stream instability. The excitation of EITI results in the modulations in the electrostatic field, which shows a correlation with the proton phase-space distribution. Simulations done by Zhang [180] have shown that in the transverse size-reduced simulation EITI propagates in the x-direction, whereas in the large transverse size simulation it propagates obliquely. In our case, since the propagation directions of EITI are in the x-direction both for the small and the large transverse-size simulations (Figs. 7.1(a) and 7.1(b)), the instability is not oblique but longitudinal. The wavelength of these modulations increases in x-direction. The excitation of heavy-ion EITI leads to a large velocity spread in the upstream region of protons in multi-ion materials. The velocity distribution of the upstream expanding protons is further broadened toward the higher velocity by the EITI between reflected protons. As a result, a larger number of protons are driven by collisionless shock acceleration mechanism. A MATLAB program is used to solve the 4th order non-linear polynomial, which has positive imaginary roots. This indicates that the unstable mode of the instability can give rise to an exponential growth in a non-uniform charge density perturbation associated with multi-ion species plasmas. It is found that the inclusion of the $1/k_x\lambda_{De}$ term in Eq. (7.3) shows that the maximum growth rate occurs at the similar k_x. The HI-EITI decelerates few protons to the lower velocity and accelerates some of heavy-ion (C-ions) to higher velocity component. This leads to the broadening of the upstream expanding protons.

Chapter 8

Heavy-Ion Acceleration

8.1 Introduction

In Chapter 6 we have shown that, the number of reflected protons and their laser-to-reflected proton conversion efficiency can be enhanced by an order of magnitude in lowest <Z/A> (C_2H_3Cl) plasma compared to pure H. The importance of EITI instability in multi-ion species plasma is discussed in the previous Chapter 7. We have shown that the instability between the expanding C-ions and protons accelerate some of the C-ions towards higher-velocity component and decelerates some of the protons toward lower-velocity component. This results in the broadening of upstream expanding protons. The velocity distribution of the expanding protons is further broadened toward the higher-velocity component by the EITI between the expanding and reflected protons, known as the reflected-proton EITI. This leads to the more protons to satisfy the ion reflection condition described by Eq. (6.14). In this chapter, we will extend our simulation outcomes by adding the discussion on the acceleration of heavy-ion via CSA mechanism.

The acceleration of heavy-ions in laser-plasma interaction is still an open question because of the certain physical parameter limits [186]. As a consequence of low <Z/A>, the heavy-ions cannot be accelerated as efficiently as protons. As compared to the protons, a large potential at the shock front (ϕ) is required to accelerate heavy ions via CSA mechanism.

In this chapter, we further generalize our results by considering the acceleration of heavy-ions (C-ions) via CSA mechanism in multi-ion species plasma. The formation of collisionless shock and their respective ion (proton and heavy-ion) acceleration becomes more interesting when we consider a multi-ion species plasma. However, one should note that the ion acceleration via CSA mechanism in multi-ion species plasma is observed experimentally [51]. The author have showed that the same shock front accelerates both protons and heavy ions. But in our simulations, we will show that two laser-driven collisionless shocks accelerate the protons and C-ions separately.

To accelerate the ions via CSA mechanism, the potential at the shock front must be larger than the kinetic energy of the upstream expanding ions in the shock-rest frame. All ions that satisfy Eq. (6.14) are accelerated by CSA mechanism. Since <Z/A> for heavy-ions is always smaller than protons, V_L^i for heavy-ion reflection is always larger than that for the protons. For C-ions, superscript i = C.

Figures 8.1(a) and 8.1(b) represent the phase-space of C-ions in C_2H_3Cl and CH plasmas, respectively, at $t = 4.0$ ps for $a_0 = 3.35$. Owing to fact and the previous experimental studies of CSA [51], here, we assumed that the shock is propagating with the same velocity V_{sh} in protons and C-ions as in $V_{sh} = V_{sh}^C$. Thus, V_L^C is larger for C-ions compared to protons, i.e., $V_L^C > V_L$. In addition to this, because of their larger mass, the upstream expanding C-ions are accelerated to a lower velocity of V_0^C by the sheath electrostatic field E_{TNSA}. The upstream expanding velocities of the C-ions are smaller compared to the V_L, as shown in Fig. 8.1. Consequently, no C-ions are accelerated via CSA mechanism. However, Fig. 8.1(a) indicates very few ions are accelerated. These ions are either accelerated from the front surface by the hole-boring process early in time or by CSA. If these ions are accelerated through CSA, this suggests the assumption of the similar shock velocity V_{sh} in protons and C-ions is not correct. Furthermore, it is practically impossible to find the shock front in carbon density or phase-space for $a_0 = 3.35$.

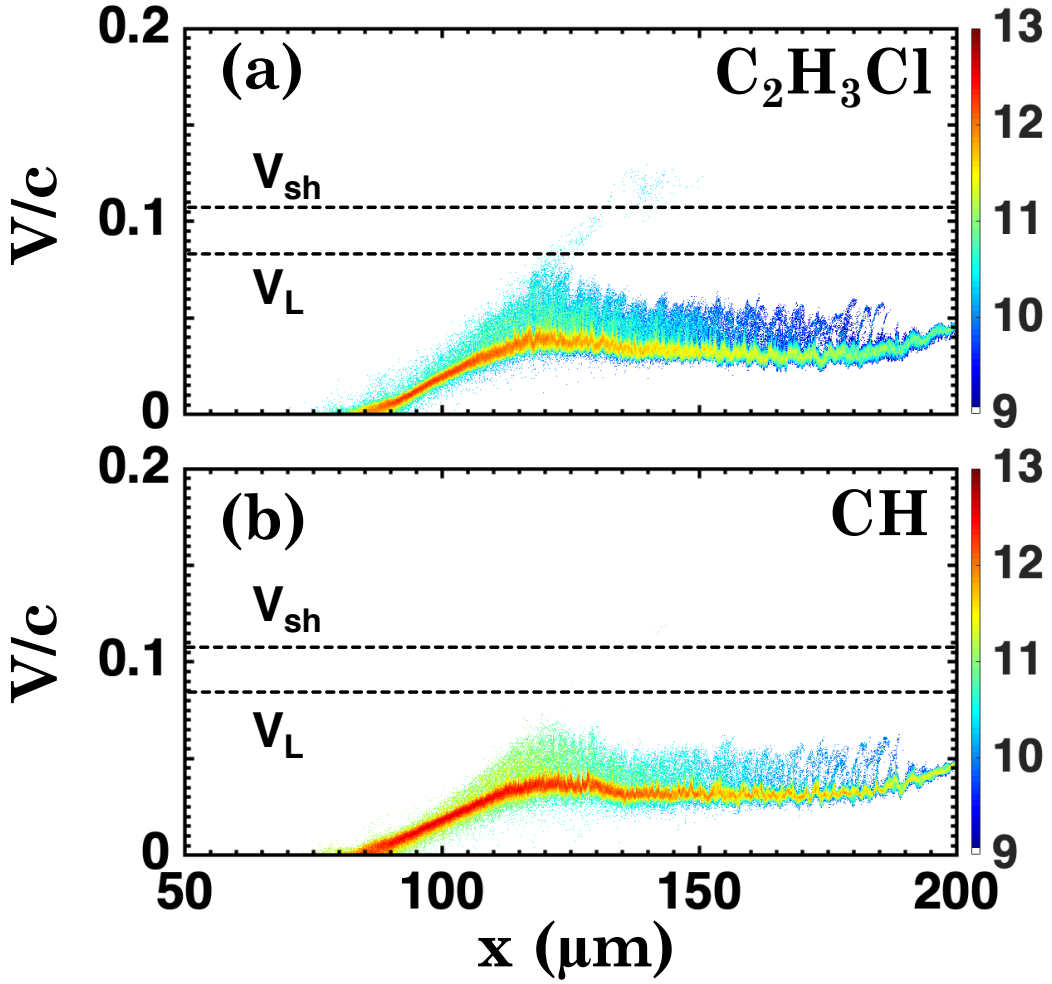


FIGURE 8.1: Phase-space of C-ions at $t = 4.0$ ps in (a) C_2H_3Cl and (b) CH plasmas. The horizontal lines represent the lower threshold V_L for ion reflection and the shock velocity in proton density (V_{sh}.)

8.2 Simulation Result for $a_0 = 10$

In order to confirm the C-ion acceleration via CSA mechanism in the multi-ion species plasma, we carried out PIC simulations for higher laser intensity corresponding to $a_0 = 10$ and a C_2H_3Cl plasma. The peak electron density is maintained at $a_0 N_{cr}$ to prevent laser-induced relativistic transparency. The interaction of laser with plasmas leads to uniform electron heating via J×B mechanism [44] and shock formation in the ion densities in a similar manner as described in Chapter 6. Figure 8.2(a) represents the normalized electron density profile (N_e/N_{cr}) at $t = 3.0$ ps and $t = 4.0$ ps in C_2H_3Cl plasma. The decrease in the electron density indicates that the thermal expansion of the plasma. Figure 8.2(b) shows the 1D electrostatic field (E_x, averaged over y-axis and two laser-cycles) and spatial profile of electrostatic potential (ϕ) at $t = 3.0$ ps. The potential profile is estimated by using Eq. (6.3). Vertical lines (dotted and solid) show that large amplitude E_x and ϕ are present at two different positions, which correspond to the two different shock fronts in proton (solid line) and C-ion (dotted line) densities. These shocks can be clearly seen in the normalized proton and C-ion densities indicated by the solid and dotted vertical lines, respectively, in Fig. 8.2(c) at $t = 3.0$ ps [Fig. 8.2(d) at $t = 4.0$ ps]. It is clear that shock positions in protons and C-ion densities are different. In other words the shock is propagating faster in protons compared to C-ions.

Ion acceleration by CSA mechanism depends on the ion reflection requirements, as explained in Chapter 6. The ions in the upstream region with a velocity larger than V_L^i are accelerated via CSA. Depending on the shock velocities, V_L^C is lower for C-ions compared to protons. Figure 8.3 represents the phase-space and velocity spectrum for protons and C-ions at $t = 4.0$ ps in pure H, C, and C_2H_3Cl plasmas. The horizontal lines on phase-space and vertical lines on velocity spectrum indicate the lower threshold velocity (V_L^i), shock velocity (V_{sh}^i), and the velocity of the reflected ions ($2V_{sh}^i$-V_L^i). Vertical lines on phase-space represent the position of the shock front. It can be seen in Fig. 8.3, a large number of protons and some of the C-ions have a velocity larger than V_L^i and are accelerated to a velocity $2V_{sh}^i$-V_L^i by CSA mechanism. Figures 8.3(f) and 8.3(i) indicate the velocity spectrum of the shock accelerated protons and C-ions, respectively, in the whole upstream region ahead of the shock front at $t = 4.0$ ps in C_2H_3Cl plasma. The protons and C-ions are accelerated to different velocities. As seen in Fig 8.3(d), the velocity distribution of the upstream expanding protons is broad in C_2H_3Cl. As we explained in Chapter 7, the broadening of the velocity distribution is caused by the development of HI-EITI and RP-EITI. The RP-EITI broadens the velocity distribution towards the higher velocity, which causes more protons to be accelerated via CSA mechanism. On the other hand, the HI-EITI decelerates some of the protons to lower velocities and accelerates C-ions to higher velocities [see Fig. 7.4] [152]. Most of the C-ions with higher velocity component satisfy the V_L^C and accelerated by CSA mechanism. In multi-ion species plasmas, the HI-EITI plays an essential role in accelerating the lower <Z/A> ions by CSA mechanism.

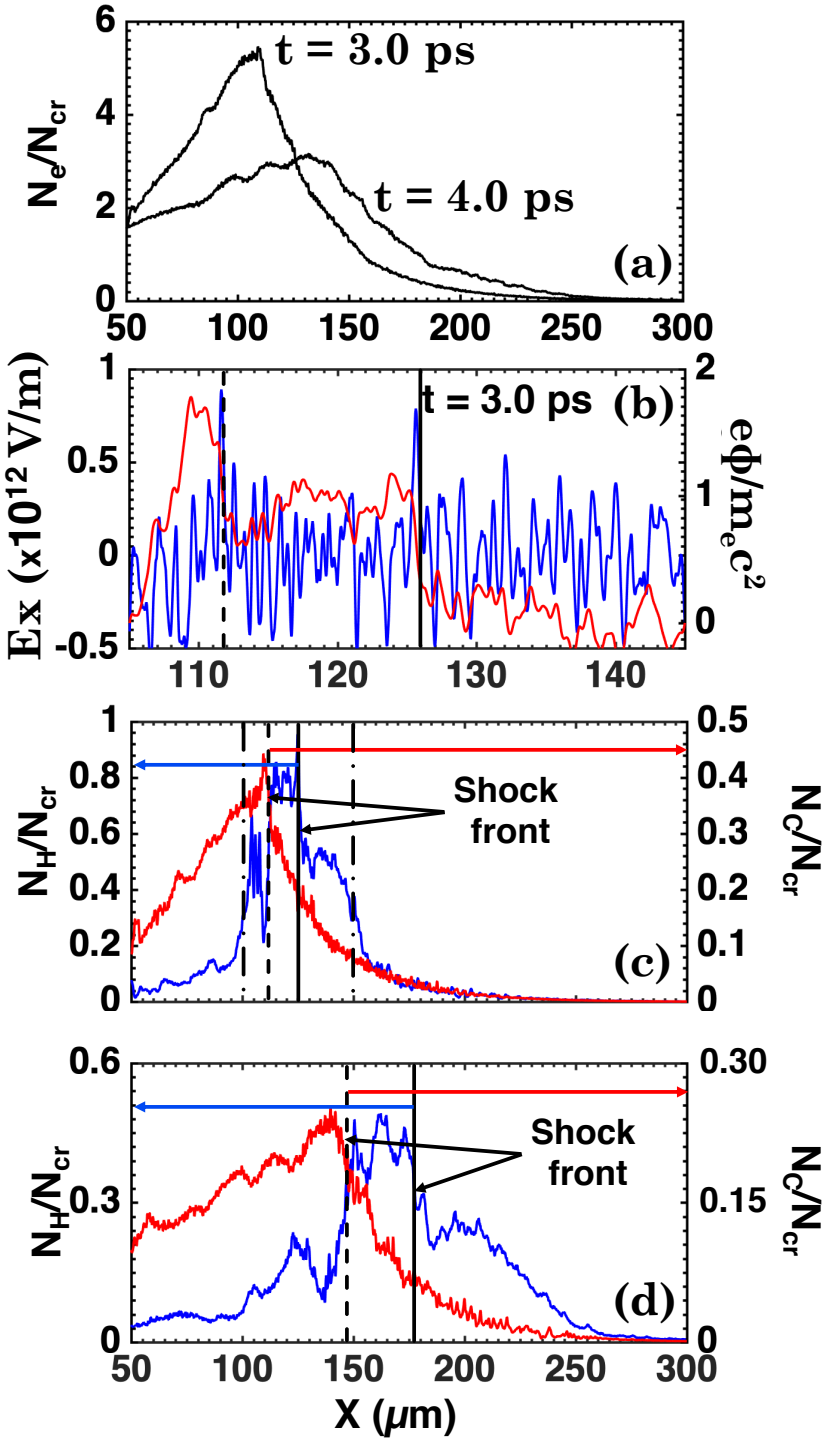


FIGURE 8.2: (a) The normalized electron density (N_e/N_{cr}) at $t = 3.0$ ps and $t = 4.0$ ps. (b) The electrostatic field (E_x) (y1) and the electrostatic potential (ϕ) (y2) at $t = 3.0$ ps. The normalized proton (N_H/N_{cr}) (y1) and carbon (N_C/N_{cr}) (y2) densities at (c) $t = 3.0$ ps and (d) $t = 4.0$ ps in C_2H_3Cl plasma for $a_0 = 10$.

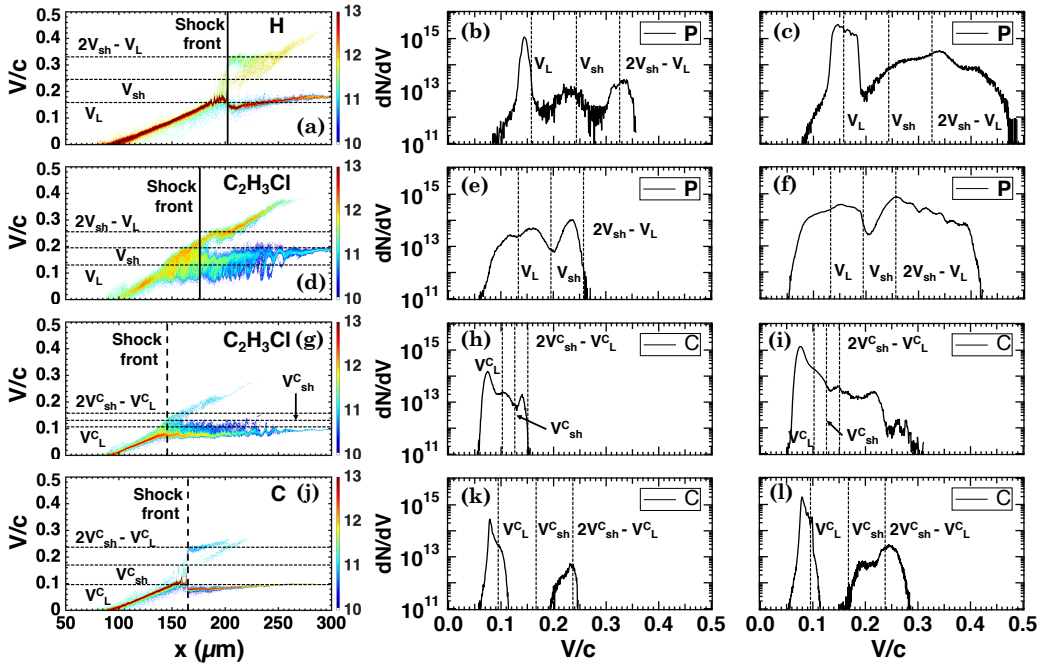


FIGURE 8.3: The 1st, 2nd, and 3rd columns indicate the ion phase-space, the velocity spectrum taken at $\Delta x = 3$ μm region, and taken in the whole upstream at $t = 4.0$ ps for $a_0 = 10$, respectively. (a) - (c) protons in pure H, (d)-(f) protons and (g)-(i) C -ions in C_2H_3Cl, and (j) - (l) C-ions in pure C plasmas.

8.3 Effect of Laser Intensity on CSA

A question arises; why are no C-ions accelerated for lower laser intensity corresponding to $a_0 = 3.35$, yet there are significant numbers of C-ions accelerated via CSA mechanism for $a_0 = 10$?

To answer this question we further extend our numerical investigation of CSA to $a_0 = 20$ and $a_0 = 33$. The electron density is maintained at $a_0 N_{cr}$ again to prevent relativistic transparency.

The energy distribution of the electrons taken in the upstream region of the shock front and the electron temperature scaling for different laser intensities are shown in Fig. 8.4. A sum of two (bulk+tail) 2D-relativistic Maxwellian's given by Eq. (6.4) are used to fit to the electron energy distribution for $a_0 = 10$, 20, and 33. The two Maxwellian's, the bulk and tail components, for $a_0 = 33$ are shown by the dotted and dashed lines, respectively, and their sum is represented by the solid lines in Fig. 8.4(a). Both the bulk and tail electron temperatures scale with a power-law dependence on a_0 as indicated in Fig. 8.4(b).

Figures 8.5(a) and 8.5(b) indicate the shock velocity (V_{sh}) and the mean velocity (V_m) of the expanding ions for protons and C-ions as a function of a_0 in pure H, C and C_2H_3Cl plasmas. The V^i_{sh} and V^i_m in protons and C-ions are always larger for pure H and C plasmas compared to the multi-ion species C_2H_3Cl plasma. In other words, both velocities (V_{sh} and V_m) follow a trend,

$$V^P_H > V^P_{C_2H_3Cl} > V^C_C > V^C_{C_2H_3Cl}, \tag{8.1}$$

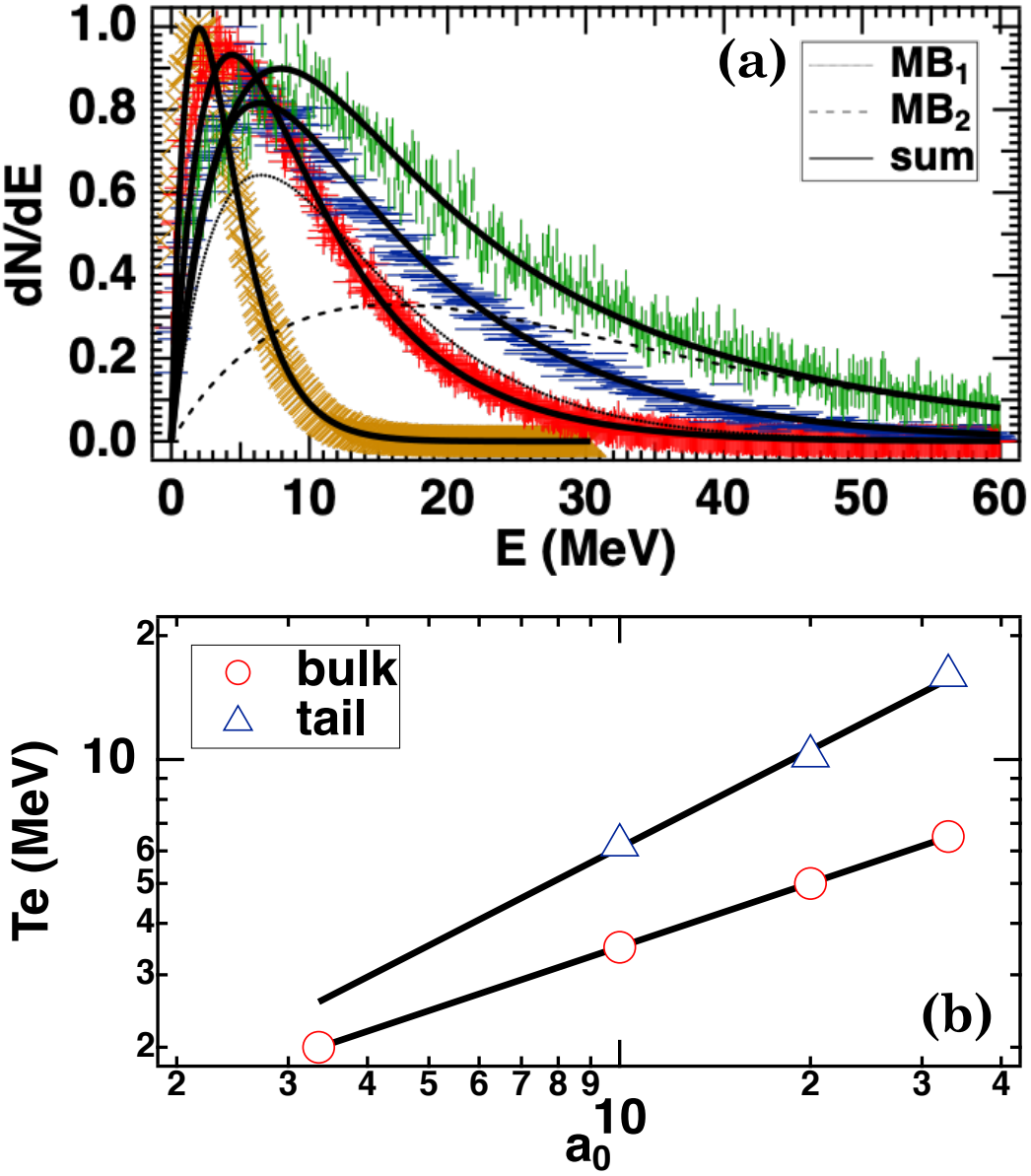


FIGURE 8.4: (a) The electron energy distribution taken in the upstream region of the shock front for different laser intensities corresponding to a_0 = 3.35 (×), 10 (+), 20 (|), and 33 (|). A sum of two (bulk [dotted]+tail [dashed]) 2D relativistic Maxwellian is used to fit to the electron energy distribution shown by the solid lines. (b) The electron temperature as a function of a_0.

for all laser intensities, here P and C denote the protons and C-ions in different plasmas indicated by the subscripts. This is because the hole-boring velocity depends on the average <Z/A> in multi-ion species plasma. This leads to the larger proton (C-ion) shock velocity in pure H (pure C) compared to that in C_2H_3Cl. Similarly, the presence of the HI-EITI in the upstream region of the C_2H_3Cl plasma results in the lower value of V_m^i compared to that in the pure H and C plasmas. Both V_{sh}^i and V_m increase with a_0 for all plasmas. The ion-acoustic velocities for proton and C-ions are calculated using Eq. (6.6), and the bulk temperature of the electrons. The bulk temperatures in the upstream region of shock fronts in pure H, C, and C_2H_3Cl plasmas are the same. Thus,

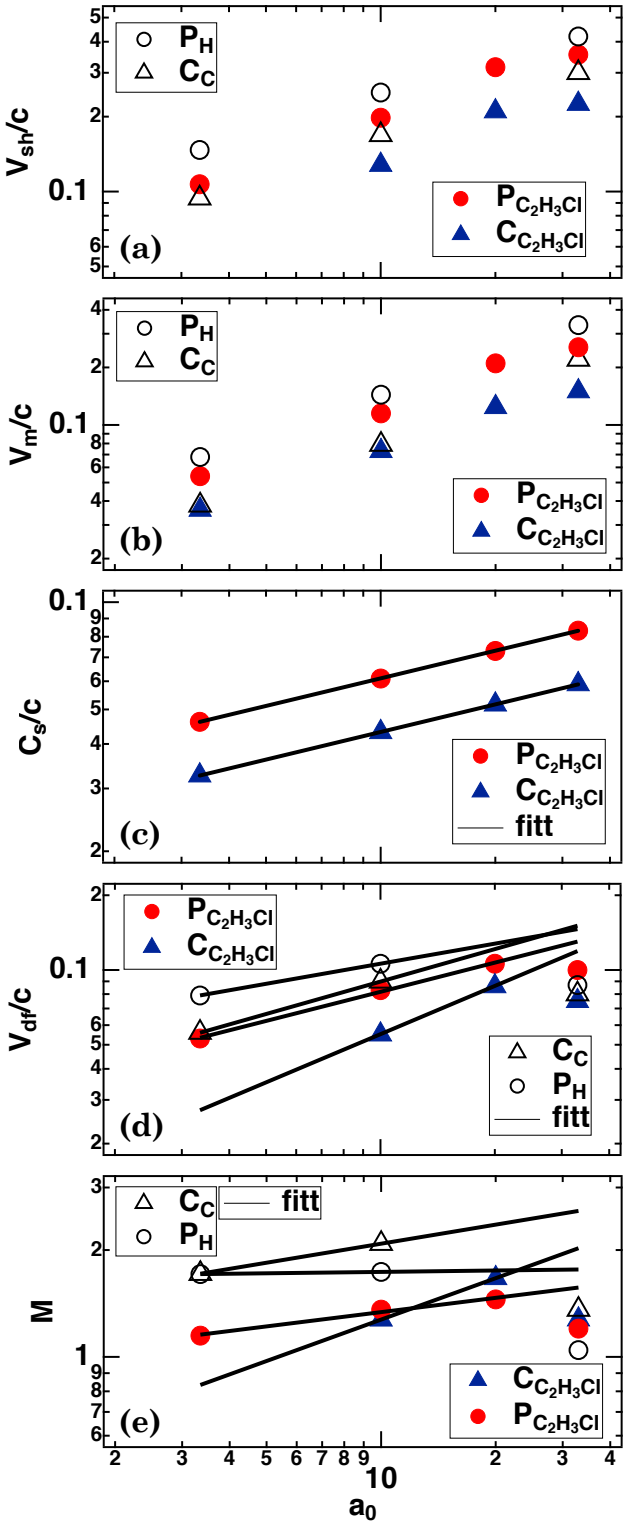


FIGURE 8.5: a_0 dependence of (a) shock velocities (V^i_{sh}), (b) mean velocity of the expanding ion velocities (V^i_m), (c) ion acoustic velocities (C^i_s), (d) difference between the shock velocity and mean of the expanding ion velocity ($V_{df} = V_{sh}$-V_m), and (e) the corresponding Mach number, $M_i = V_{df}/C^i_s$ for pure H (open circles), C (open triangles) plasmas, and protons (filled circles), and C-ions in C_2H_3Cl.

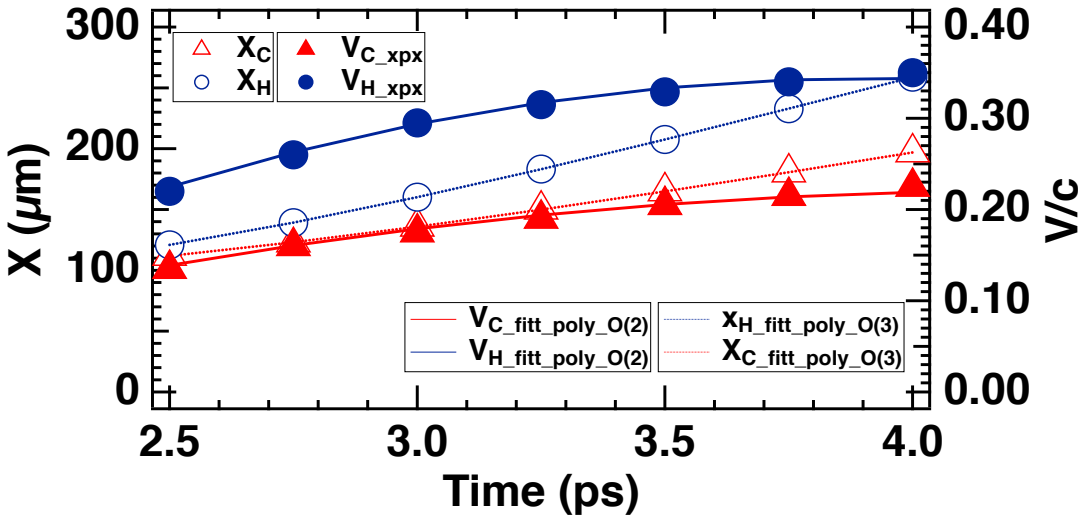


FIGURE 8.6: The temporal evolution of shock position and velocity for protons and C-ions in C_2H_3Cl plasma for $a_0 = 33$.

the ion-acoustic velocity solely depends on the square root of Z/A, as shown in Fig. 8.5(c). The ion-acoustic velocity follows a power-law dependence (solid lines) with a_0, which is determined by the bulk electron temperature scaling. The difference between the shock velocity and mean velocity of the expanding ion, i.e., $V^i_{df} = V^i_{sh}$ - V^i_m is shown in Fig. 8.5(d). The V^i_{df} increases with a_0 and shows a power-law dependence with a_0 except for $a_0 = 33$. The ratio between the V^i_{df} and C^i_s provides the Mach number, i.e. $M_i = V^i_{df}/C^i_s$ as shown in Fig. 8.5(e). It is clear that the Mach number for C-ions (M_C) is a stronger function of a_0 compared to that of protons (M_P) in C_2H_3Cl, and M_C become less than one (M_C <1) for $a_0 = 3.35$, therefore no shock exist in C-ions. Both M_P and M_C are stronger functions of a_0 in C_2H_3Cl compared to the pure H and C plasmas. When M_i >1 the shock dissipation is compensated for by ion reflection from the shock front. For $a_0 = 33$ the shock dissipation via ion reflection becomes more pronounced which results in the reduction of the shock velocity (Fig. 8.5(a)) and Mach number (Fig. 8.5(e)) from the scaling obtained using $a_0 = 3.35$, 10 and 20.

Figure 8.6 indicates the temporal evolution of the shock position and velocity for protons and C-ions in C_2H_3Cl plasma for $a_0 = 33$. A 3rd order polynomial can very well fit the temporal evolution of shock position. And a derivative of the shock position with respect to time gives the shock velocity which is scaled as a 2nd order polynomial. The exponential scaling of the shock position and velocity with respect to time for $a_0 = 3.35$ (Fig. 6.5(a)), 10, and 20 is changed to the 3rd and 2nd order polynomial functions, respectively, for $a_0 = 33$. This is because the shock dissipation through ion reflection becomes stronger, and slow-down of shock velocity occurs for $a_0 = 33$.

Figure 8.7 indicates the energy (E) and the number (dN/dE at E) at the peak of the energy distribution of reflected ions for $a_0 = 3.35$, 10, 20, and 33 in pure H, C, and C_2H_3Cl plasmas. The E and dN/dE of the shock reflected C-ions and protons increase with increasing the laser intensity, as shown in

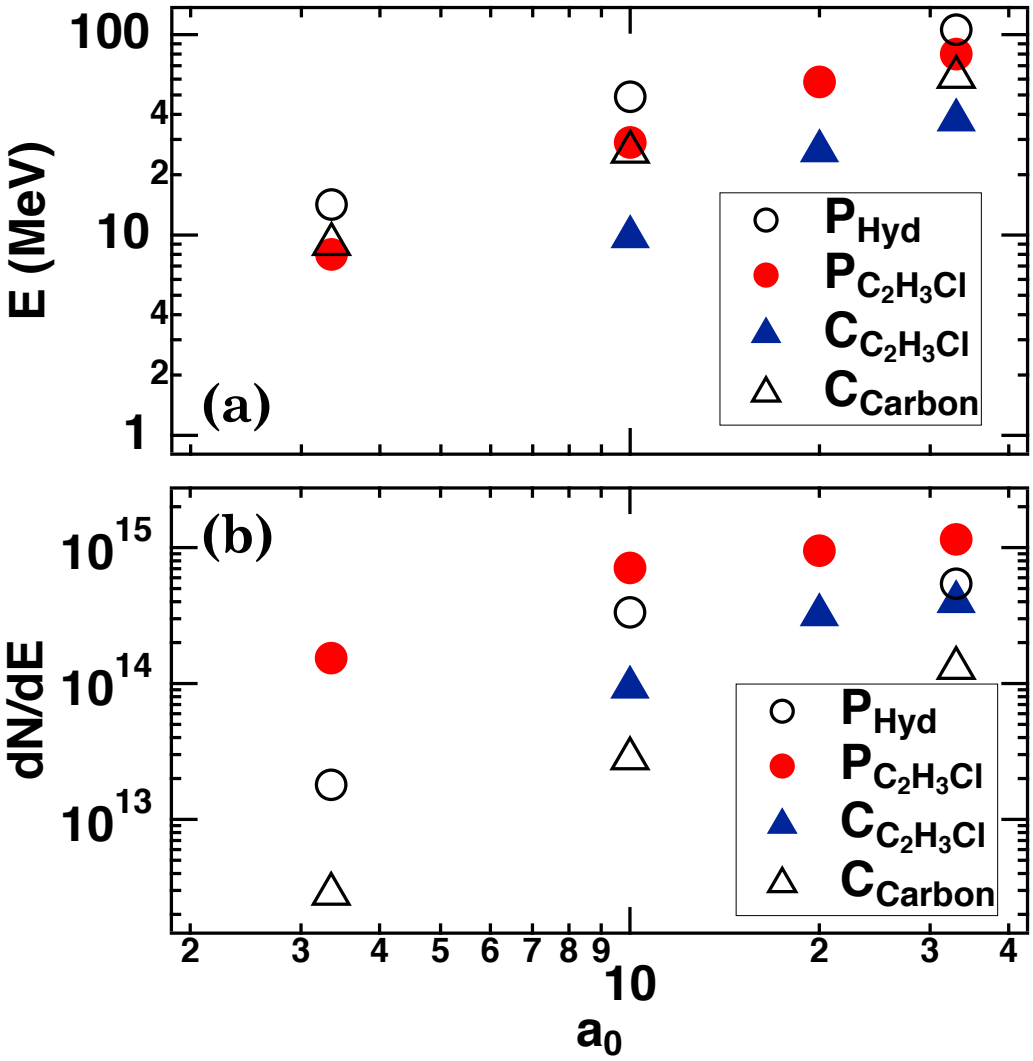


FIGURE 8.7: a_0 dependence of (a) energy (E) and (b) the number (dN/dE at E) of reflected protons and C-ions at the peak of the energy distribution at $t = 4.0$ ps for pure H (open circles) and C (open triangles) plasmas, and protons (filled circles) and C-ions in C_2H_3Cl.

Figs. 8.7(a) and 8.7(b), respectively. As the Mach number scaling shows that there are no shocks in C-ions for $a_0 = 3.35$ (M<1), thus no C-ion acceleration observed in C_2H_3Cl plasma. The energy (E) of the reflected protons and C-ions is always larger in pure H and C plasmas compared to that in C_2H_3Cl, as shown in Fig. 8.7(a). This is because the proton (C-ion) shock velocity is larger in pure H (pure C) compared to the C_2H_3Cl plasma. The flux of the reflected protons and C-ions is always larger in C_2H_3Cl compared to the pure H, and C plasmas. As we explained in the previous article [152], the instability between the reflected and expanding protons (RP-EITI) broadens the velocity distribution of the upstream expanding protons towards the higher velocity. This causes more protons to satisfy the ion reflection condition Eq. (6.14). This leads to higher protons flux in C_2H_3Cl plasma compared to pure H. Similarly, presence of the HI-EITI broadens the velocity distribution of the

expanding ions towards the higher velocity, which results in more C-ions to be accelerated via CSA mechanism in C_2H_3Cl compared to pure C plasmas.

8.4 Summary

The interaction of laser intensities corresponding to $a_0 \geq 10$ with multi-ion species (C_2H_3Cl) plasma leads to the formation of two shock fronts in proton and carbon density, respectively. The shock fronts propagate slower in C-ions compared to protons. Thus both C-ions and protons are accelerated by different shocks via CSA mechanism. The shock velocity and Mach number of C-ions and protons can be scaled as the power-law dependence on a_0. In case of C-ions, the Mach number is a stronger function of a_0 compared to that of protons in the multi-ion species plasma with the lowest $<Z/A>$, i.e. (C_2H_3Cl). The number of shocks accelerated protons and C-ions is more significant in multi-ion species plasma compared to the pure H and C plasmas.

Chapter 9

CSA LFEX-GXII Experiment

9.1 Introduction

In this chapter, we experimentally explore the suitable initial plasma profile for Collisionless Electrostatic Shock Acceleration (CSA) of protons by using sub-μm CH foil targets. The rear-surface of CH foil target is irradiated by a pre-ionization laser beam to produce a suitable density profile for CSA. After the target expansion, a shock-driving beam ($a_0 \simeq 1.6$) is irradiated from the front side of the target to derive a collisionless shock wave. The necessary density profile is optimized by varying the time delay, $\Delta t = 0-1.5$ ns, between the two laser beams. Furthermore, we used 1D hydrodynamics and 2D particle-in-cell (PIC) simulations and compared the experimental results with the numerical ones. It is shown that the trend of accelerated proton energy and electron temperature on the initial plasma profile observed in the experiment agrees with the one obtained by simulations.

9.2 Experimental Setup

The CSA experiment is conducted by using a combination of GXII (pre-ionization beam) and LFEX (shock-driving beam) laser beam facilities at the Institute of Laser Engineering, Osaka University. Both lasers have a similar wavelength of 1.053 μm. Initially, a pre-ionization GXII laser corresponding to an intensity $\sim 10^{12}$ Wcm^{-2} with 1.3 ns pulse-duration irradiates a 0.7 μm CH foil target to produce the necessary density profile for CSA mechanism. After the target expansion, a high-intensity shock driving LFEX laser beam corresponding to an intensity $\sim 3.5\times 10^{18}$ Wcm^{-2} with a pulse duration $\sim$1.0 ps is used to derive the collisionless shock wave. The necessary density profile for CSA process has been optimized by varying the time delay, $\Delta t = 0-1.5$ ns, between the pre-ionization (GXII) and shock-driving (LFEX) laser beams. The simple schematic for the experimental setup is displayed in Fig. 9.1.

The energy of the accelerated protons along the laser pulse direction is measured by using passive stacks of radiochromic films (RCF) which are located at a distance of $\sim$ 60$-$70 cm on the rear-side of the target. A CR39 detector is attached to the back of the RCF stack to measure the ion traces. The half area of the CR39 detector plate is overlaid with the RCF stack, and half of it is exposed to the accelerated ions. Both of the passive ion detectors, i.e., RCF and CR39 detectors, are wrapped into thick aluminum foil to protect them from

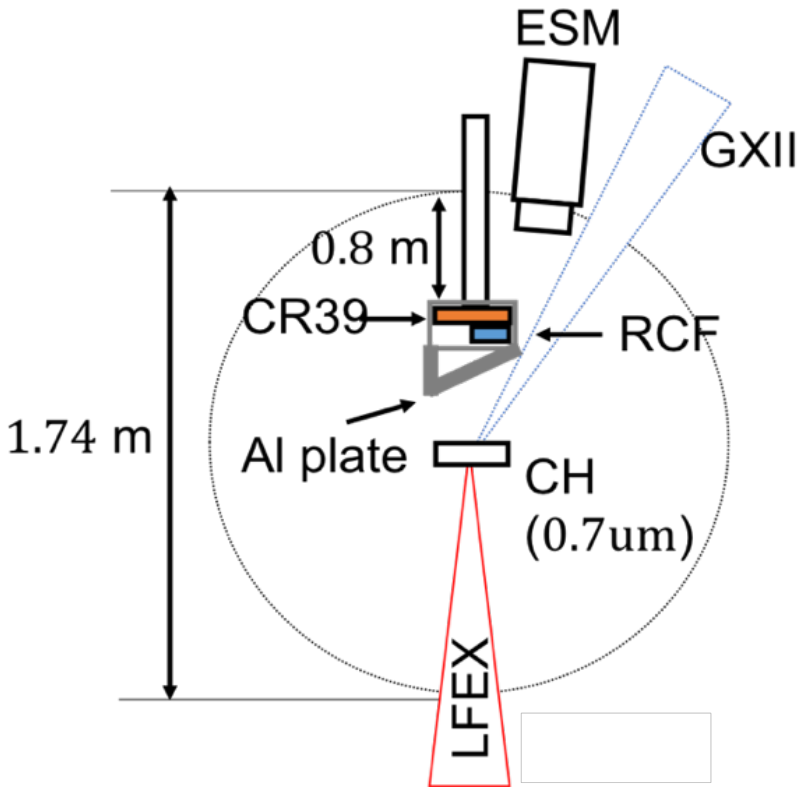


FIGURE 9.1: A schematic of the experimental setup (top view). A pre-ionization (GXII) laser beam interacts with the 0.7 μm CH target to produce the near-critical density plasma. After a few ns, a high-intensity shock-driving (LFEX) laser pulse is focused on the exploded target to generate the collisionless shock. A stack of RCF (HD-V2 & EBT3) and CR39 plate are used to detect the accelerated ions along the shock-driving laser direction. A 52.4 μm thick Aluminum foil is used to protect the ion diagnostics from the scattered laser light and thermal emission from the rear surface of the target. An electron spectrometer is mounted at a 20.6° to derive the hot electron temperature [taken from [187]].

the damage induced by the transmitted laser pulse and block all the plasma thermal emission expected from the back of the target. Thus, the accelerated ions will first pass through the Al foil, then RCF (HD-V2 & EBT3), and finally hit the half of CR39. The rest of the CR39 detector is directly exposed to the accelerated ion after passing through the Al foil. HD-V2 is put ahead of the EBT3. This is because HD-V2 has a wide dynamic range and ability to absorb the X-rays. Also, an electron spectrometer detector is used to obtain the electron temperature and produce the electron energy spectrum.

9.3 Experimental Results

The interaction of the pre-ionization beam with a solid target results in the plasma density expansion, which is suitable to generate the collisionless shock waves. Depending on the time delay, Δt the shock driving laser interacts with a particular plasma density, which might be suitable for CSA. Therefore, we

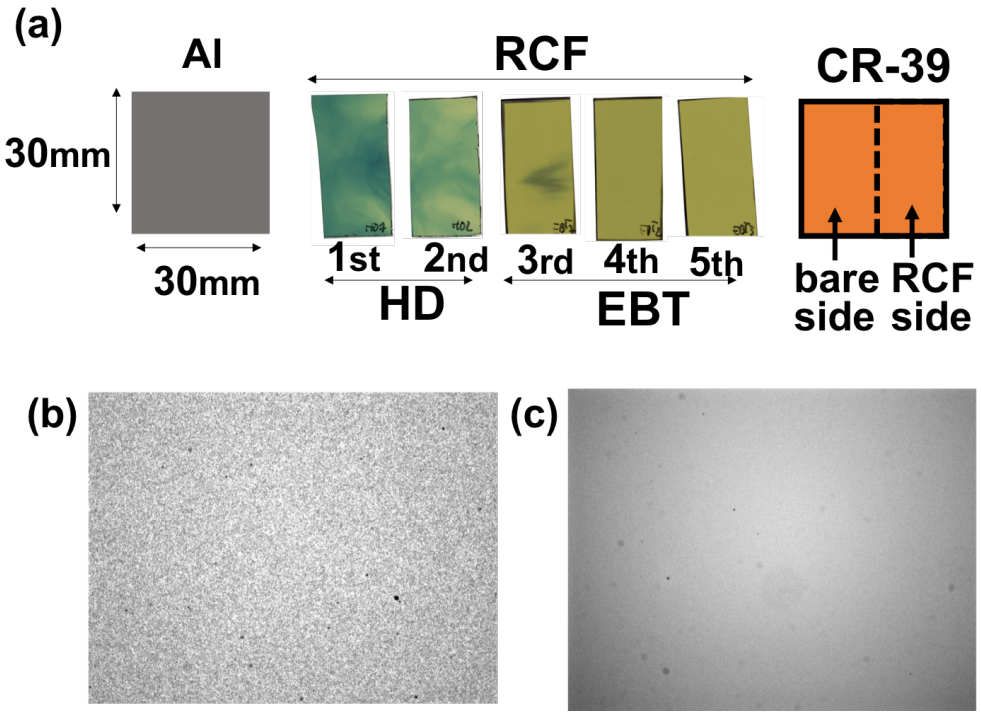


FIGURE 9.2: (a) A sequence of the RCF films exposed to the accelerated ions produced by the shock-driving laser pulse at a time delay, $\Delta t = 0.2$ ns. A change in the color from the 1st to 3rd RCF film suggest that the energy of accelerated ions is in the range of 7.03 MeV to 9.03 MeV. (b) The front surface, where pits of the accelerated ions are present and (c) rear-surface of the CR39 plate. The CR39 plate shown here is directly exposed (not behind the RCF stacks) to the accelerated ions, and both images are 50× magnified [taken from [187]].

vary the time delay to find the most suitable plasma density to generate the collisionless shock and their subsequent ion acceleration. Figure 9.2 represents the experimental data for $\Delta t = 0.2$ ns. Interestingly, for $\Delta t = 0.2$ ns, the 1st, 2nd and 3rd layers of RCF stack in the shock-driving laser direction exhibits the signal as shown in Fig. 9.2(a). There is no signal observed on the 4th layer of RCF stack. This indicates the energetic ions passed through the 1st, 2nd layers and stopped at the 3rd layer of RCF stacks with the maximum energy ranging from 7.03 MeV to 9.03 MeV. This estimation of energy is made by considering a 52.5 μm aluminum shielding (filter) in front of the RCF stacks, which is used to block the transmitted laser pulse. The RCF stacks provide only the ion signal density and estimation of accelerated ion energies. It does not provide any information about the feature of the ions. Thus, to distinguish the accelerated protons and C^{6+} ions, further characterization of the CR39 detector plate is needed.

Figures 9.2(b) and 9.2(c) indicate the front and back surfaces of CR39 detector, respectively. The CR39 images displayed here are 50× magnified by using a microscope. The accelerated ions interact with the front surface of the CR39 plate through the collision cascade process, which destroys the molecular structure and damages the plate [188]. Through the etching process, the area

damaged by the impact of accelerated ions etches faster compared to the undamaged area of the plate. Consequently, the impact of the accelerated ions generates a track on CR39 plates, which is commonly referred to as a pit. The characterization of these pits is essential to identify the accelerated ions species (either protons or C^{6+} in our case) and their energies. In our case, a single ∼30 min KOH solution etching is applied to the CR39 plate [see Fig. 9.2(b)]. The analysis of the size and diameter of these pits through the microscope implies that the accelerated ions are protons, not C^{6+}. The accelerated protons 2.25 MeV of energy when they pass through a 52.4 μm aluminum foil before interacting with the CR39 plate. The impact of the accelerated protons cannot be seen on the rear surface of the CR39 detector plate, as shown in Fig. 9.2(c). The characterization of these pits suggests that the energy of the accelerated proton is within ∼2.25 MeV to 10 MeV. Unfortunately, further etching of the plate results in the overlapping of etch pits. Thus we have to bound our measurements to the single etching process. To overcome this problem, the distance between the target (CH) and CR39 has to be increased. This will lead to the small solid angle between the target and CR39 plate, which results in less proton interaction with the plate.

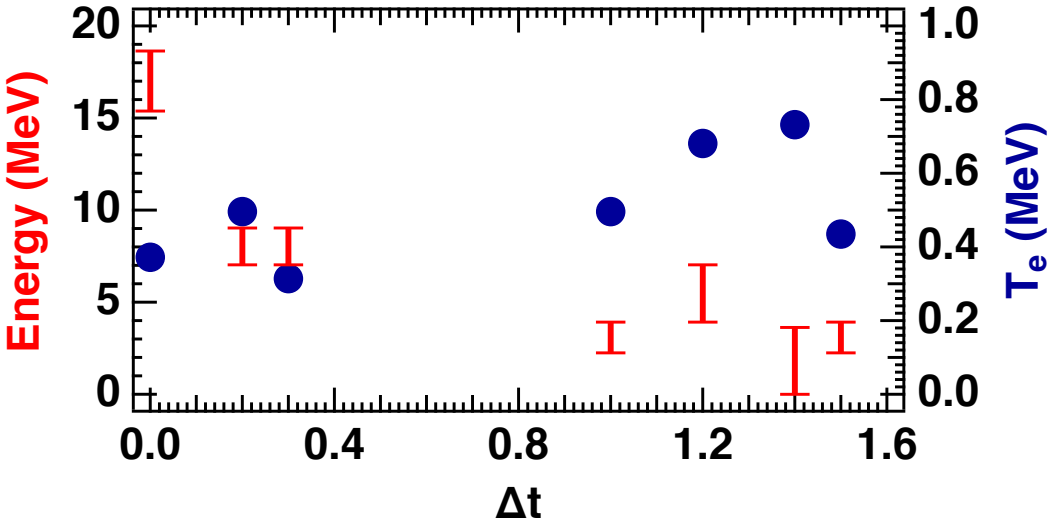


FIGURE 9.3: The time delay, Δt dependance of accelerated proton energy (horizontal bars) and electron temperature (filled circles). The error bars in the proton energy represent the uncertainty in the estimation of proton energy from RCF stacks. The time, $\Delta t = 0$ indicates that, no pre-ionization laser pulse is used in experiment [187]].

Correspondence between the proton energy and electron temperature is accomplished by varying the time delay, Δt between the pre-ionization (GXII) and shock driving (LFEX) laser pulses as shown in Fig. 9.3. Because of the time-constrained for experiment, only 7 laser shots are taken for a time delay, $\Delta t = 0$, 0.2, 0.3, 1.0, 1.2, 1.4, and 1.5 ns. The time delay, $\Delta t = 0$, indicates that the experimental data is obtained without a pre-ionization (GXII) laser beam. The proton energy is determined by utilizing the RCF stacks. An electron spectrometer is mounted at an angle 20.6° along the laser propagation direction to measure the corresponding electron temperature. For $\Delta t = 0$ (no pre-ionization

laser), the proton energy and electron temperature are the characteristics of TNSA mechanism. The interaction of pre-ionization laser with the rear-surface of CH target ($\Delta t > 0$) results in the thermal expansion of plasma density. The plasma density on the rear-side of the target expands faster compared to the front-side of the target. Thus the suppression of TNSA sheath field occurs and leads to the smaller proton energy and higher electron temperature. This is because, as Δt increases, it results in the expansion of the plasma density on the front side of the target, which enhances the laser absorption. The hydrodynamic calculation carried out by using ILESTA code suggests that the interaction of pre-ionization laser with the solid target results in an exponentially decreasing density profile on the front- and back-sides of the target. Thus for $\Delta t > 0$, the peak density decreases and scale-length of the plasma increases on both sides of the target. An exponentially decreasing density profile on the rear-side of the target results in the suppression of sheath TNSA field [137]. This supervises to lower proton energy for $\Delta t > 0$, as shown in Fig. 9.3. The exponentially decreasing density profile on the front-side of the target enhances the laser absorption and various kind of laser plasma instabilities. This results in a higher electron temperature for $\Delta t > 0$. At $\Delta t = 1.2$ ns, an increase in the proton energy is observed, which might be the result of CSA mechanism. This is because by $\Delta t = 1.2$ ns proton acceleration via TNSA is almost suppressed by the exponential density profile. And the peak density of the plasma decreased to the near-critical density with an exponentially decreasing scale-length on the rear-side of the target. These are the optimum requirements for CSA mechanism to occur [46]. As a result, protons are accelerated via CSA mechanism.

9.4 Simulation Results

We carried out 1D hydrodynamic and 2D particle-in-cell (PIC) simulations to demonstrate the experimental investigation of plasma density expansion and proton acceleration. 1D ILESTA [189] hydrodynamic code is adopted to simulate the interaction of GXII laser beam with a 0.7 μm CH foil target. These simulations suggest that the peak density of the plasma decays with an exponential scale-length on the front- and rear-sides of the target with time. Consequently, we utilize the output density profile of ILESTA to perform the EPOCH PIC [103] simulation.

The simulation box is 300 μm $\times$ 6 μm in size and composed of 9000 $\times$ 180 grid points along the x- and y-axis, respectively. Each cell contains 16 particles composed of electrons, protons (H^+), and fully ionized carbon (C^{6+}) ions. The boundary conditions are open in x and periodic in y for both field and particles. The linearly p-polarized laser pulse is utilized in the simulations, which propagates along the x-axis. The laser pulse has a Gaussian temporal profile with 1.5 ps full-width at half-maximum corresponds to a peak intensity of 3.5×10^{18} Wcm^{-2} ($a_0 = 1.6$). The simulated target composed of a special density profile with an exponentially increasing 10 μm front scale-length and an exponentially decreasing with 20 μ scale-length on the rear-side of the target. This density profile is approximately similar to the output profile of ILESTA

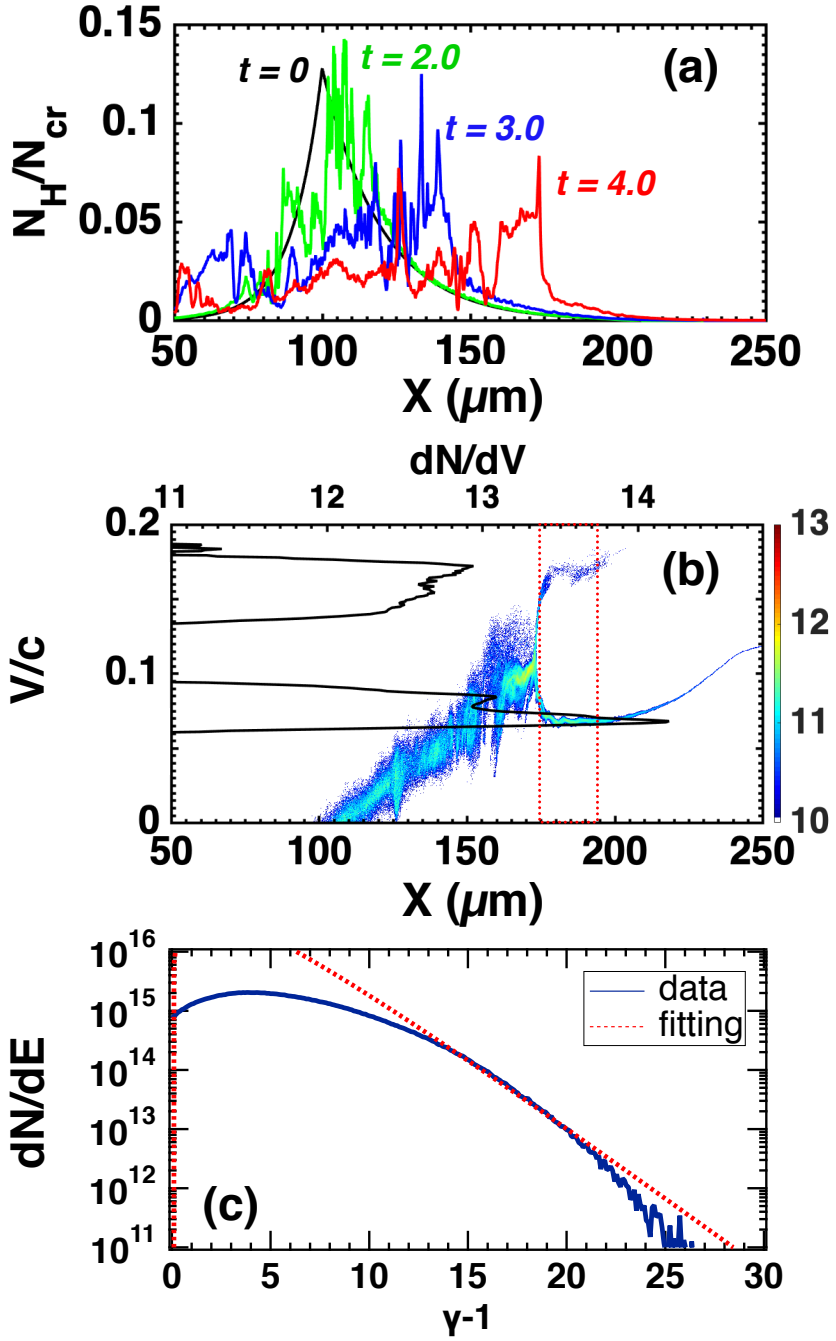


FIGURE 9.4: (a) Time evolution of proton density profile (averaged along the y-axis) at t = 0, 2.0, 3.0, and 4.0 ps. (b) A phase-space and velocity distribution of the protons taken in 20 μm (vertical dotted lines) ahead of the shock front at t = 4.0 ps. (c) Electron energy spectrum at 4.0 ps and its fitting curve by 2-D relativistic Maxwellian [187]].

simulations. The density profile is fixed, and the peak electron density is varied from (0.1- 2.0)N_{cr} for several simulations. Here, $N_{cr} = 1.12\times10^{21}$ cm^{-3} is the critical plasma density for a laser wavelength 1.053 μm.

Simulation outcomes for the interaction of high-intensity laser with the critical density (N_{cr}) plasma are shown in Fig. 9.4. The temporal progression of

the normalized proton density (N_H/N_{cr}) is illustrated in Fig. 9.4(a). At t = 0 the density describes the initial density profile, which is determined by the output of ILESTA hydrodynamic simulations. The interaction of high-intensity laser with critical-density plasma ends in the uniform electron heating via J×B mechanism [44] and accumulation of plasma density into the high-density region via the hole-boring process. By t = 2.0 ps, the laser peak is gone, and thermal expansion of the plasma on the rear-side of the target directs to the shock formation. As time evolves further, the shock front propagates in the forward direction, as shown in Fig. 9.4(a).

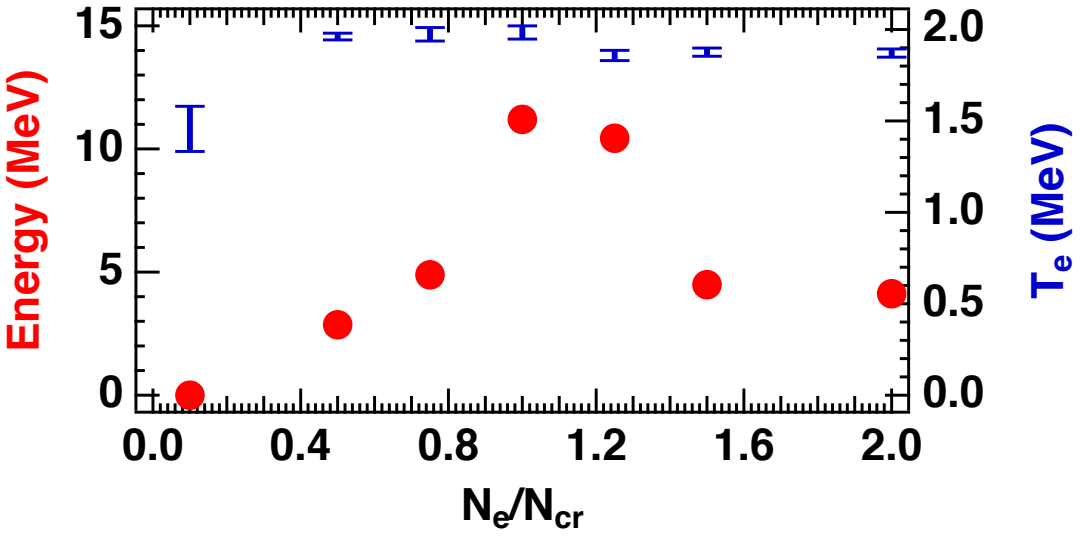


FIGURE 9.5: The PIC results of the accelerated proton energy and electron temperature as a function of initial normalized electron density at t = 4.0 ps [187].

The proton phase-space taken at t = 4.0 ps is illustrated in Fig. 9.4(b). The black line overlaid on the proton phase-space corresponds to the proton velocity spectrum taken at Δx = 20 μm (shown by vertical dotted lines in Fig. 9.4(b)) ahead of the shock front. The shock front reflects some of the upstream expanding protons to the twice of the shock velocity in the shock rest frame. The corresponding velocity spectrum in the upstream region indicates that a monoenergetic proton is accelerated via CSA mechanism. Although no clear shock exit in the carbon phase-space. Figure 9.4(c) represents the electron energy spectrum taken at t = 4.0 ps. To obtain the electron temperature, a 2D relativistic Maxwellian is used to fit the electron energy spectrum.

The energy of shock accelerated protons and electron temperature as a function of initial normalized electron density (N_e/N_{cr}) is shown in Fig. 9.5. The energy of the accelerated proton increases with increase in N_e/N_{cr}. And energy become maximum for an initial density N_e/N_{cr} = 1.0, which is roughly similar to the density profile obtained from hydrodynamic simulations for Δt = 1.2 ns. Similarly, electron temperature shows a maximum for initial density, N_e/N_{cr} = 1.0.

The proton energy and electron temperature estimated through PIC simulations are higher than the experimental measurements. There are several reasons behind it, such as the PIC simulations are done under the ideal conditions, and

the effect of the LFEX pre-pulse is not considered on the plasma density profile. Also, we don't have any information about the initial plasma density profile produced by GXII during the experiment. Initial density profile used in PIC simulations relies on the 1D hydrodynamic simulations in which the front- and rear-side plasma scale-lengths are underestimated. PIC simulations performed by Fiuza [46] have confirmed that a larger scale-length on the rear-side of the plasma results in the smaller energy of the accelerated protons. In addition to that, the electron temperature obtained in PIC simulation is very high compared to the experimental data. Since the PIC simulations are done in 2D, it leads to the overestimation of electron temperature compared to the 3D case. Although, the energy of accelerated protons determined via PIC simulations [see Fig. 9.5] is in rough agreement with the experimental data [see Fig. 9.3] for $\Delta t = 1.0{-}1.5$ ns.

9.5 Summary

In summary, we report on the experimental demonstration of CSA by using a combination of GXII (pre-ionization beam) and LFEX (shock-driving beam) laser facilities at the Institute of Laser Engineering, Osaka University (Japan). The interaction of pre-ionization laser with rear-surface of CH target ($\Delta t > 0$) results in the thermal expansion of the plasma. After the target expansion, a shock-driving beam is irradiated from the front side of the target to derive a collisionless shock wave. The necessary density profile is optimized by varying the time delay, $\Delta t = 0{-}1.5$ ns between the two laser beams. The passive ion diagnostics, i.e., RCF stacks and CR39 detector plates confirm that the maximum energy of the accelerated protons is in the range of 7.03 MeV - 9.03 MeV for $\Delta t = 1.2$ ns. the energy of accelerated protons determined via PIC simulations is in rough agreement with the experimental data for $\Delta t = 1.0{-}1.5$ ns.

Chapter 10

Summary & Future Work

10.1 Summary

In summary, the EPOCH PIC open source code is used to study the laser-driven collisionless shock ion acceleration in different materials. The different materials used are hydrogen, carbon, oxygen, and chlorine to give a range of <Z/A> = 0.48-1 [see Table 6.1]. The density profile and laser parameters are the same for all target materials. The electrostatic collisionless shocks are driven by the interaction of high-intensity laser with near-critical density plasma. A charge imbalance electrostatic field results in a sharp electrostatic potential at the shock front, which reflects the upstream expanding ions. The electron temperature is the same for all target material plasmas. The temporal evolution of electron temperature can be very well fitted with a sigmoid function with a derivative peaking at $t = 1.75$ ps. It is shown that the laser to reflected proton conversion efficiency and number of reflected protons are significantly enhanced in the lowest <Z/A> material compared to the pure H. The number of the reflected protons depends on the lower threshold velocities (V_L) for proton reflection and shock velocities (V_{sh}). Lower values of V_L always result in high proton flux. The protons with high-flux and narrower energy-spread can be produced using lower <Z/A> materials.

In the upstream region of the shock, ions expand with different velocities depending on their <Z/A> under the non-oscillating component of the sheath electrostatic field. In multi-ion species plasmas, the excitation of electrostatic ion two-stream instability (EITI) between the heavier and lighter ion populations occurs. This results in the deceleration of the expanding protons and appearance of a low-velocity component. An additional EITI between the reflected and expanding protons accelerates some of the expanding protons to the higher velocity, which results in more protons being accelerated by the shock. The excitation of EITI results in the modulations in the electrostatic field, which shows a correlation with the phase-space distribution. The analytic and exact solutions for the dispersion relation of EITI indicate that the unstable modes of the instability appear in multi-ion species plasmas.

Our results show that the interaction of high-intensity laser beam ($a_0 \geq 10$) with multi-ion species plasma (C_2H_3Cl) leads to the formation of two shock fronts in fully ionized carbon (C^{6+}) and proton, respectively. Both shocks propagate with different shock velocities and have different values of lower threshold velocities V_L^i for ion reflection. Therefore, both C-ions and protons are accelerated by different shocks via CSA mechanism. It is shown that the electron

temperature follows a power-law dependence on a_0. Similarly, shock velocities and Mach numbers for shocks in protons and C-ions increase with a_0 and follow a power-law dependence on a_0. In case of C-ions, the Mach number is a stronger function of a_0 compared to that of protons in the multi-ion species plasma with the lowest <Z/A>, i.e., (C_2H_3Cl). The flux of shock accelerated protons and C-ions is more significant in multi-ion species plasma compared to the pure H and C plasmas.

We further expand our results by including the experimental demonstration of CSA. The CSA experiment was performed by using a combination of GXII (pre-ionization beam) and LFEX (shock-driving beam) laser facilities at the Institute of Laser Engineering, Osaka University. The interaction of pre-ionization laser with rear-surface of CH target ($\Delta t > 0$) results in the thermal expansion of the plasma. After the target expansion, a shock-driving beam is irradiated from the front side of the target to derive a collisionless shock wave. The optimum density profile for CSA is obtained by varying the time delay, $\Delta t = 0-1.5$ ns between the two laser beams. The passive ion diagnostics, i.e., RCF stacks and CR39 detector plates confirm that the maximum energy of the accelerated protons is in the range of 7.03 MeV−9.03 MeV for $\Delta t = 1.2$ ns. The energy of accelerated protons determined via PIC simulations is in rough agreement with the experimental data for $\Delta t = 1.0-1.5$ ns.

10.2 Future Work

The simulation results presented in this thesis could provide meaningful guidance for the experimental study of laser-driven collisionless shock and their subsequent ion acceleration. A key issue for potential applications having a monoenergetic spectrum with a high laser-to-reflected ion conversion efficiency can be resolved by using lower <Z/A> materials compared with pure H. The different targets used throughout the simulations are readily available these days. The experimental demonstration can be carried out by using the combination of two laser pulses. The first beam preionizes the target and the second beam excites the collisionless shock and accelerates the upstream expanding ions as the shock propagates through the plasma. The desirable density profile can be achieved by changing the laser intensity, pulse-width of the primary laser, or the time delay between two laser pulses. Therefore, the relevant experiments can be conducted by using the GXII and LFEX laser beams on a combined experiment. Acceleration of heavy-ions is expected in multi-ion species plasmas when the laser intensities are further increased. The development of EITI in the upstream region of multi-ion species plasma can give rise to the charge density (electric field) modulations ahead of the shock front. This can be directly studied by using the ultrafast proton radiography diagnostics. The relevant experiment will require, the optical diagnostics (interferometry and shadowgraphy) for the optimization of the initial density profile for CSA. However, it is not an easy task to perform multi-laser beams experiments. It requires a careful examination of the initial density profile and time delay between the two laser beams. Therefore, we carried out simulations by using the fully ionized He^3H and CH_4 plasmas to provide direction to the single laser beam experiments.

The flux of the shock accelerated protons is enhanced in both plasmas (He^3H and CH_4) as compared to the pure H. The proton flux is always high in lower <Z/A> plasmas as compared to pure H. The relevant experiment can be done by using the interaction of a high-intensity laser with gas-jet or liquid CH_4 in place of pure H, which can provide the high-flux with narrower energy-spread proton beams.

Moreover, all 2D simulations throughout this thesis are conducted in plane wave approximation with infinite spot-size. An extended 2D simulation study with a finite laser spot-size will be needed to characterize collisionless shock formation and their subsequent ion acceleration in different materials. The physical mechanism responsible for two shock formation in multi-ion species plasmas needs to address.

Bibliography

1. Maiman, T. H., Hoskins, R., d'Haenens, I., Asawa, C. K. & Evtuhov, V. Stimulated optical emission in fluorescent solids. II. Spectroscopy and stimulated emission in ruby. *Physical Review* **123,** 1151 (1961).
2. Nuckolls, J., Wood, L., Thiessen, A. & Zimmerman, G. Laser compression of matter to super-high densities: Thermonuclear (CTR) applications. *Nature* **239,** 139 (1972).
3. McClung, F. & Hellwarth, R. Giant optical pulsations from ruby. *Journal of Applied Physics* **33,** 828–829 (1962).
4. Hargrove, L., Fork, R. L. & Pollack, M. Locking of He–Ne laser modes induced by synchronous intracavity modulation. *Applied Physics Letters* **5,** 4–5 (1964).
5. DiDomenico Jr, M. Small-signal analysis of internal (coupling-type) modulation of lasers. *Journal of Applied Physics* **35,** 2870–2876 (1964).
6. Strickland, D. & Mourou, G. Compression of amplified chirped optical pulses. *Optics Communications* **55,** 447–449 (1985).
7. Yanovsky, V *et al.* Ultra-high intensity-300-TW laser at 0.1 Hz repetition rate. *Optics Express* **16,** 2109–2114 (2008).
8. Danson, C., Hillier, D., Hopps, N. & Neely, D. Petawatt class lasers worldwide. *High Power Laser Science and Engineering* **3,** e3 (2015).
9. Mourou, G. A., Tajima, T. & Bulanov, S. V. Optics in the relativistic regime. *Reviews of Modern Physics* **78,** 309 (2006).
10. Hatchett, S. P. *et al.* Electron, photon, and ion beams from the relativistic interaction of Petawatt laser pulses with solid targets. *Physics of Plasmas* **7,** 2076–2082 (2000).
11. Ganeev, R. High-order harmonic generation in laser plasma: Recent achievements. *Laser Physics* **22,** 1177–1188 (2012).
12. Teubner, U & Gibbon, P. High-order harmonics from laser-irradiated plasma surfaces. *Reviews of Modern Physics* **81,** 445 (2009).
13. Nakamura, K. *et al.* Diagnostics, control and performance parameters for the BELLA high repetition rate petawatt class laser. *IEEE Journal of Quantum Electronics* **53,** 1–21 (2017).
14. Kostyukov, I. Y., Nerush, E. & Bashmakov, V. *QED effects and radiation generation in relativistic laser plasma* in *Harnessing Relativistic Plasma Waves as Novel Radiation Sources from Terahertz to X-Rays and Beyond II* **8075** (2011), 807504.

15. Tajima, T. & Dawson, J. M. Laser electron accelerator. *Physical Review Letters* **43,** 267 (1979).

16. Modena, A *et al.* Electron acceleration from the breaking of relativistic plasma waves. *Nature* **377,** 606 (1995).

17. Esarey, E., Sprangle, P., Krall, J. & Ting, A. Overview of plasma-based accelerator concepts. *IEEE Transactions on Plasma Science* **24,** 252–288 (1996).

18. Mangles, S. P. *et al.* Monoenergetic beams of relativistic electrons from intense laser–plasma interactions. *Nature* **431,** 535 (2004).

19. Leemans, W. P. *et al.* GeV electron beams from a centimetre-scale accelerator. *Nature Physics* **2,** 696 (2006).

20. Malka, V. *et al.* Principles and applications of compact laser–plasma accelerators. *Nature Physics* **4,** 447 (2008).

21. Wang, X. *et al.* Quasi-monoenergetic laser-plasma acceleration of electrons to 2 GeV. *Nature Communications* **4,** 1988 (2013).

22. Fazel, N. B. *et al. Quasi-monoenergetic laser-plasma acceleration of electrons beyond 1 GeV at the Texas Petawatt Laser,* PhD thesis (2015).

23. Assmann, R. in *Challenges and Goals for Accelerators in the XXI Century,* 723–740 (World Scientific, 2016).

24. Macchi, A., Borghesi, M. & Passoni, M. Ion acceleration by superintense laser-plasma interaction. *Reviews of Modern Physics* **85,** 751 (2013).

25. Linlor, W. I. Ion energies produced by laser giant pulse. *Applied Physics Letters* **3,** 210–211 (1963).

26. Gitomer, S. *et al.* Fast ions and hot electrons in the laser–plasma interaction. *The Physics of Fluids* **29,** 2679–2688 (1986).

27. Fews, A. *et al.* Plasma ion emission from high intensity picosecond laser pulse interactions with solid targets. *Physical Review Letters* **73,** 1801 (1994).

28. Beg, F. *et al.* A study of picosecond laser–solid interactions up to 1019 W cm- 2. *Physics of Plasmas* **4,** 447–457 (1997).

29. Krushelnick, K *et al.* Multi-MeV ion production from high-intensity laser interactions with underdense plasmas. *Physical Review Letters* **83,** 737 (1999).

30. Clark, E. *et al.* Measurements of energetic proton transport through magnetized plasma from intense laser interactions with solids. *Physical Review Letters* **84,** 670 (2000).

31. Snavely, R. *et al.* Intense high-energy proton beams from petawatt-laser irradiation of solids. *Physical Review Letters* **85,** 2945 (2000).

32. Maksimchuk, A., Gu, S., Flippo, K., Umstadter, D. & Bychenkov, V. Y. Forward ion acceleration in thin films driven by a high-intensity laser. *Physical Review Letters* **84,** 4108 (2000).

33. Wilks, S. *et al.* Energetic proton generation in ultra-intense laser–solid interactions. *Physics of Plasmas* **8,** 542–549 (2001).

34. Daido, H., Nishiuchi, M. & Pirozhkov, A. S. Review of laser-driven ion sources and their applications. *Reports on Progress in Physics* **75,** 056401 (2012).

35. Klimo, O, Psikal, J, Limpouch, J & Tikhonchuk, V. Monoenergetic ion beams from ultrathin foils irradiated by ultrahigh-contrast circularly polarized laser pulses. *Physical Review Special Topics-Accelerators and Beams* **11,** 031301 (2008).

36. Robinson, A. *et al.* Relativistically correct hole-boring and ion acceleration by circularly polarized laser pulses. *Plasma Physics and Controlled Fusion* **51,** 024004 (2009).

37. Yan, X. *et al.* Generating high-current monoenergetic proton beams by a circularlypolarized laser pulse in the phase-stableacceleration regime. *Physical Review Letters* **100,** 135003 (2008).

38. Macchi, A., Cattani, F., Liseykina, T. V. & Cornolti, F. Laser acceleration of ion bunches at the front surface of overdense plasmas. *Physical Review Letters* **94,** 165003 (2005).

39. Macchi, A., Veghini, S. & Pegoraro, F. "Light sail" acceleration reexamined. *Physical Review Letters* **103,** 085003 (2009).

40. Esirkepov, T, Borghesi, M, Bulanov, S., Mourou, G & Tajima, T. Highly efficient relativistic-ion generation in the laser-piston regime. *Physical Review Letters* **92,** 175003 (2004).

41. Tidman, D. A. & Krall, N. A. *Shock Waves in Collisionless Plasmas* (Wiley-Interscience, New York, 1971).

42. Denavit, J. Absorption of high-intensity subpicosecond lasers on solid density targets. *Physical Review Letters* **69,** 3052 (1992).

43. Silva, L. O. *et al.* Proton shock acceleration in laser-plasma interactions. *Physical Review Letters* **92,** 015002 (2004).

44. Kruer, W. & Estabrook, K. J× B heating by very intense laser light. *The Physics of Fluids* **28,** 430–432 (1985).

45. Fiuza, F *et al.* Laser-driven shock acceleration of monoenergetic ion beams. *Physical Review Letters* **109,** 215001 (2012).

46. Fiuza, F *et al.* Ion acceleration from laser-driven electrostatic shocks. *Physics of Plasmas* **20,** 056304 (2013).

47. Liu, M *et al.* Collisionless electrostatic shock formation and ion acceleration in intense laser interactions with near critical density plasmas. *Physics of Plasmas* **23,** 113103 (2016).

48. Zhang, W. *et al.* Quasi-monoenergetic ion beam acceleration by laser-driven shock and solitary waves in near-critical plasmas. *Physics of Plasmas* **23,** 073118 (2016).

49. Haberberger, D. *et al.* Collisionless shocks in laser-produced plasma generate monoenergetic high-energy proton beams. *Nature Physics* **8,** 95 (2012).

50. Antici, P *et al.* Acceleration of collimated 45 MeV protons by collisionless shocks driven in low-density, large-scale gradient plasmas by a 10^{20} W/cm^2, 1 μm laser. *Scientific Reports* **7,** 16463 (2017).

51. Pak, A *et al.* Collisionless shock acceleration of narrow energy spread ion beams from mixed species plasmas using 1 μ m lasers. *Physical Review Accelerators and Beams* **21,** 103401 (2018).

52. Zhang, H. *et al.* Collisionless shock acceleration of high-flux quasimonoenergetic proton beams driven by circularly polarized laser pulses. *Physical Review Letters* **119,** 164801 (2017).

53. Tresca, O *et al.* Spectral modification of shock accelerated ions using a hydrodynamically shaped gas target. *Physical Review Letters* **115,** 094802 (2015).

54. Zhang, H *et al.* Collisionless shocks driven by 800 nm laser pulses generate high-energy carbon ions. *Physics of Plasmas* **22,** 013113 (2015).

55. Cowan, T. E. *et al.* Ultralow Emittance, Multi-MeV Proton Beams from a Laser Virtual-Cathode Plasma Accelerator. *Physical Review Letters* **92,** 204801 (20 2004).

56. West, D & Sherwood, A. Radiography with 160 MeV protons. *Nature* **239,** 157 (1972).

57. Steward, V. & Koehler, A. Proton beam radiography in tumor detection. *Science* **179,** 913–914 (1973).

58. Borghesi, M *et al.* Proton imaging: a diagnostic for inertial confinement fusion/fast ignitor studies. *Plasma Physics and Controlled Fusion* **43,** A267 (2001).

59. Borghesi, M. *et al.* Electric field detection in laser-plasma interaction experiments via the proton imaging technique. *Physics of Plasmas* **9,** 2214–2220 (2002).

60. Romagnani, L. *et al.* Dynamics of electric fields driving the laser acceleration of multi-MeV protons. *Physical Review Letters* **95,** 195001 (2005).

61. Romagnani, L *et al.* Observation of collisionless shocks in laser-plasma experiments. *Physical Review Letters* **101,** 025004 (2008).

62. Li, C. *et al.* Measuring E and B fields in laser-produced plasmas with monoenergetic proton radiography. *Physical Review Letters* **97,** 135003 (2006).

63. Nilson, P. *et al.* Magnetic reconnection and plasma dynamics in two-beam laser-solid interactions. *Physical Review Letters* **97,** 255001 (2006).

64. Cecchetti, C. *et al.* Magnetic field measurements in laser-produced plasmas via proton deflectometry. *Physics of Plasmas* **16,** 043102 (2009).

65. Willingale, L. *et al.* High-power, kilojoule class laser channeling in millimeter-scale underdense plasma. *Physical Review Letters* **106,** 105002 (2011).

66. Wilson, R. R. Radiological use of fast protons. *Radiology* **47,** 487–491 (1946).

67. Amaldi, U. & Kraft, G. Radiotherapy with beams of carbon ions. *Reports on Progress in Physics* **68,** 1861 (2005).

68. Chu, W., Ludewigt, B. & Renner, T. Instrumentation for treatment of cancer using proton and light-ion beams. *Review of Scientific Instruments* **64,** 2055–2122 (1993).

69. Kraft, G. *et al.* Tumortherapy with ion beams. *Nuclear Instruments and Methods in Physics Research Section A: Accelerators, Spectrometers, Detectors and Associated Equipment* **454,** 1–10 (2000).

70. Bulanov, S. & Khoroshkov, V. Feasibility of using laser ion accelerators in proton therapy. *Plasma Physics Reports* **28,** 453–456 (2002).

71. Bulanov, S. *et al. Feasibility of using laser ion accelerators in proton therapy* in *AIP Conference Proceedings* **740** (2004), 414–429.

72. Malka, V. *et al.* Practicability of protontherapy using compact laser systems. *Medical Physics* **31,** 1587–1592 (2004).

73. Linz, U. & Alonso, J. What will it take for laser driven proton accelerators to be applied to tumor therapy? *Physical Review Special Topics-Accelerators and Beams* **10,** 094801 (2007).

74. Fritzler, S *et al.* Proton beams generated with high-intensity lasers: Applications to medical isotope production. *Applied Physics Letters* **83,** 3039–3041 (2003).

75. Lefebvre, E., d'Humières, E., Fritzler, S. & Malka, V. Numerical simulation of isotope production for positron emission tomography with laser-accelerated ions. *Journal of Applied Physics* **100,** 113308 (2006).

76. Wesson, J. Tokamaks, Clarendon Press, Oxford (1987).

77. Llewellyn-Smith, C. & Ward, D. Fusion power. *European Review* **13,** 337–359 (2005).

78. Nuckolls, J., Wood, L., Thiessen, A. & Zimmerman, G. Laser compression of matter to super-high densities: Thermonuclear (CTR) applications. *Nature* **239,** 139 (1972).

79. Muratov, V. P., Saksagansky, G. L. & Filatov, O. G. in *Fundamentals of Magnetic Thermonuclear Reactor Design* 39–67 (Elsevier, 2018).

80. Dolan, T. J. *Fusion Research, Volume III "Technology"* (Pergamon Press, 1982).

81. Braams, C. M. & Stott, P. E. *Nuclear fusion: half a century of magnetic confinement fusion research* (CRC Press, 2002).

82. Lehnert, B. Half a century of fusion research towards ITER. *Physica Scripta* **87,** 018201 (2012).

83. Kidder, R. Energy gain of laser-compressed pellets: a simple model calculation. *Nuclear Fusion* **16,** 405 (1976).
84. Meyer-ter Vehn, J. On energy gain of fusion targets: the model of Kidder and Bodner improved. *Nuclear Fusion* **22,** 561 (1982).
85. Atzeni, S. & Meyer-ter Vehn, J. *The physics of inertial fusion: beam plasma interaction, hydrodynamics, hot dense matter* (OUP Oxford, 2004).
86. Tabak, M. *et al.* Ignition and high gain with ultrapowerful lasers. *Physics of Plasmas* **1,** 1626–1634 (1994).
87. Chen, F. F. *Introduction to plasma physics and controlled fusion* (Springer, 1984).
88. Miyamoto, K. *Fundamentals of plasma physics and controlled fusion* (Iwanami Book Service Center Tokyo, 1997).
89. Debye, P & Huckel, E. The theory of the electrolyte II-The border law for electrical conductivity. *Phys. Z* **24,** 305–325 (1923).
90. Jackson, J. D. *Classical electrodynamics* (AAPT, 1999).
91. Wilks, S. C. & Kruer, W. L. Absorption of ultrashort, ultra-intense laser light by solids and overdense plasmas. *IEEE Journal of Quantum Electronics* **33,** 1954–1968 (1997).
92. Forslund, D., Kindel, J. & Lee, K. Theory of hot-electron spectra at high laser intensity. *Physical Review Letters* **39,** 284 (1977).
93. Estabrook, K. & Kruer, W. L. Properties of resonantly heated electron distributions. *Physical Review Letters* **40,** 42 (1978).
94. Gibbon, P. *Short pulse laser interactions with matter* (World Scientific Publishing Company Singapore, 2004).
95. Rozmus, W & Tikhonchuk, V. Skin effect and interaction of short laser pulses with dense plasmas. *Physical Review A* **42,** 7401 (1990).
96. Brunel, F. Not-so-resonant, resonant absorption. *Physical Review Letters* **59,** 52 (1987).
97. Wilks, S., Kruer, W., Tabak, M & Langdon, A. Absorption of ultra-intense laser pulses. *Physical Review Letters* **69,** 1383 (1992).
98. Malka, G & Miquel, J. Experimental confirmation of ponderomotive-force electrons produced by an ultrarelativistic laser pulse on a solid target. *Physical Review Letters* **77,** 75 (1996).
99. Birdsall, C. K. & Langdon, A. B. *Plasma physics via computer simulation* (CRC press, 2018).
100. Hockney, R. W. & Eastwood, J. W. *Computer simulation using particles* (crc Press, 1988).
101. Boris, J. P. *Relativistic plasma simulation-optimization of a hybrid code* in *Proc. 4th Conf. Num. Sim. Plasmas* (1970), 3–67.
102. Langdon, A. B. & Lasinski, B. F. Electromagnetic and relativistic plasma simulation models. *Methods in Computational Physics* **16,** 327–366 (1976).

103. Arber, T. *et al.* Contemporary particle-in-cell approach to laser-plasma modelling. *Plasma Physics and Controlled Fusion* **57,** 113001 (2015).

104. Henig, A. *Advanced approaches to high intensity laser-driven ion acceleration* PhD thesis (lmu, 2010).

105. Robson, L. *et al.* Scaling of proton acceleration driven by petawatt-laser–plasma interactions. *Nature Physics* **3,** 58 (2007).

106. Albright, B. *et al.* Theory of laser acceleration of light-ion beams from interaction of ultrahigh-intensity lasers with layered targets. *Physical Review Letters* **97,** 115002 (2006).

107. Robinson, A. L., Bell, A. & Kingham, R. Effect of target composition on proton energy spectra in ultraintense laser-solid interactions. *Physical Review Letters* **96,** 035005 (2006).

108. Passoni, M. & Lontano, M. One-dimensional model of the electrostatic ion acceleration in the ultraintense laser–solid interaction. *Laser and Particle Beams* **22,** 163–169 (2004).

109. Gurevich, A., Pariiskaya, L. & Pitaevskii, L. Self-similar motion of rarefied plasma. *Sov. Phys. JETP* **22,** 449–454 (1966).

110. Mora, P. Plasma expansion into a vacuum. *Physical Review Letters* **90,** 185002 (2003).

111. Crow, J., Auer, P. & Allen, J. The expansion of a plasma into a vacuum. *Journal of Plasma Physics* **14,** 65–76 (1975).

112. Lifshitz, E. & Landau, L. *Course of theoretical physics: fluid mechanics* (Butterworth-Heinemann, Oxford UK, 1987).

113. Passoni, M. & Lontano, M. Theory of light-ion acceleration driven by a strong charge separation. *Physical Review Letters* **101,** 115001 (2008).

114. Schwoerer, H *et al.* Laser-plasma acceleration of quasi-monoenergetic protons from microstructured targets. *Nature* **439,** 445 (2006).

115. Esirkepov, T. Z. *et al.* Proposed double-layer target for the generation of high-quality laser-accelerated ion beams. *Physical Review Letters* **89,** 175003 (2002).

116. Hegelich, B. M. *et al.* Laser acceleration of quasi-monoenergetic MeV ion beams. *Nature* **439,** 441 (2006).

117. Wagner, F *et al.* Maximum proton energy above 85 mev from the relativistic interaction of laser pulses with micrometer thick ch 2 targets. *Physical Review Letters* **116,** 205002 (2016).

118. Robinson, A., Zepf, M, Kar, S, Evans, R. & Bellei, C. Radiation pressure acceleration of thin foils with circularly polarized laser pulses. *New Journal of Physics* **10,** 013021 (2008).

119. Macchi, A., Veghini, S., Liseykina, T. V. & Pegoraro, F. Radiation pressure acceleration of ultrathin foils. *New Journal of Physics* **12,** 045013 (2010).

120. Marx, G. Interstellar vehicle propelled by terrestrial laser beam. *Nature* **211,** 22 (1966).

121. Sentoku, Y, Cowan, T., Kemp, A & Ruhl, H. High energy proton acceleration in interaction of short laser pulse with dense plasma target. *Physics of Plasmas* **10,** 2009–2015 (2003).

122. Fuchs, J *et al.* Comparison of laser ion acceleration from the front and rear surfaces of thin foils. *Physical Review Letters* **94,** 045004 (2005).

123. Palmer, C. A. *et al.* Monoenergetic proton beams accelerated by a radiation pressure driven shock. *Physical Review Letters* **106,** 014801 (2011).

124. Zepf, M. *et al.* Proton acceleration from high-intensity laser interactions with thin foil targets. *Physical Review Letters* **90,** 064801 (2003).

125. Habara, H *et al.* Ion acceleration from the shock front induced by hole boring in ultraintense laser-plasma interactions. *Physical Review E* **70,** 046414 (2004).

126. Liseikina, T. V., Prellino, D., Cornolti, F. & Macchi, A. Ponderomotive Acceleration of ions: Circular versus linear polarization. *IEEE Transactions on Plasma Science* **36,** 1866–1871 (2008).

127. Schlegel, T *et al.* Relativistic laser piston model: Ponderomotive ion acceleration in dense plasmas using ultraintense laser pulses. *Physics of Plasmas* **16,** 083103 (2009).

128. Pegoraro, F. & Bulanov, S. Photon bubbles and ion acceleration in a plasma dominated by the radiation pressure of an electromagnetic pulse. *Physical Review Letters* **99,** 065002 (2007).

129. Zhang, X. *et al.* Instabilities in interaction of circularly polarized laser pulse and overdense target. *Physics of Plasmas* **18,** 073101 (2011).

130. Blandford, R. & Eichler, D. Particle acceleration at astrophysical shocks: A theory of cosmic ray origin. *Physics Reports* **154,** 1–75 (1987).

131. Martins, S., Fonseca, R., Silva, L. & Mori, W. Ion dynamics and acceleration in relativistic shocks. *The Astrophysical Journal Letters* **695,** L189 (2009).

132. Wei, M. *et al.* Ion acceleration by collisionless shocks in high-intensity-laser–underdense-plasma interaction. *Physical Review Letters* **93,** 155003 (2004).

133. d'Humières, E., Lefebvre, E., Gremillet, L. & Malka, V. Proton acceleration mechanisms in high-intensity laser interaction with thin foils. *Physics of Plasmas* **12,** 062704 (2005).

134. Taylor, R., Baker, D. & Ikezi, H. Observation of collisionless electrostatic shocks. *Physical Review Letters* **24,** 206 (1970).

135. Sorasio, G, Marti, M, Fonseca, R & Silva, L. Very high Mach-number electrostatic shocks in collisionless plasmas. *Physical Review Letters* **96,** 045005 (2006).

136. Chen, M. *et al.* Collisionless electrostatic shock generation and ion acceleration by ultraintense laser pulses in overdense plasmas. *Physics of Plasmas* **14,** 053102 (2007).

137. Grismayer, T & Mora, P. Influence of a finite initial ion density gradient on plasma expansion into a vacuum. *Physics of Plasmas* **13,** 032103 (2006).

138. Boella, E., Fiúza, F., Novo, A. S., Fonseca, R. & Silva, L. Ion acceleration in electrostatic collisionless shock: on the optimal density profile for quasi-monoenergetic beams. *Plasma Physics and Controlled Fusion* **60,** 035010 (2018).

139. d'Humières, E *et al.* Investigation of laser ion acceleration in low-density targets using exploded foils. *Plasma Physics and Controlled Fusion* **55,** 124025 (2013).

140. Fuchs, J *et al.* Laser-driven proton scaling laws and new paths towards energy increase. *Nature Physics* **2,** 48 (2006).

141. Kim, I. J. *et al.* Radiation pressure acceleration of protons to 93 MeV with circularly polarized petawatt laser pulses. *Physics of Plasmas* **23,** 070701 (2016).

142. Dollar, F *et al.* Enhanced laser absorption from radiation pressure in intense laser plasma interactions. *New Journal of Physics* **19,** 063014 (2017).

143. Zel'Dovich, Y. B. & Raizer, Y. P. *Physics of shock waves and high-temperature hydrodynamic phenomena* (Courier Corporation, 2012).

144. Gary, S. P., Gosling, J. & Forslund, D. The electromagnetic ion beam instability upstream of the earth's bow shock. *Journal of Geophysical Research: Space Physics* **86,** 6691–6696 (1981).

145. Kirk, J. G. & Duffy, P. Particle acceleration and relativistic shocks. *Journal of Physics G: Nuclear and Particle Physics* **25,** R163 (1999).

146. Gurnett, D. A. & Bhattacharjee, A. *Introduction to plasma physics: with space and laboratory applications* (Cambridge University Press, 2005).

147. Viñas, A. F. & Scudder, J. D. Fast and optimal solution to the "Rankine-Hugoniot problem". *Journal of Geophysical Research: Space Physics* **91,** 39–58 (1986).

148. Mellott, M. The physical mechanisms of subcritical collisionless shock-wave formation. *Advances in Space Research* **4,** 245–253 (1984).

149. Kennel, C. F. Critical Mach numbers in classical magnetohydrodynamics. *Journal of Geophysical Research: Space Physics* **92,** 13427–13437 (1987).

150. Sagdeev, R. Review of Plasma Physics, vol. 4. *New York: Consultants Bureau,* 23–91 (1966).

151. Moiseev, S. & Sagdeev, R. *Shock waves in a rarefied plasma in a weak magnetic field* in *Soviet Physics Doklady* **7** (1963), 813.

152. Kumar, R., Sakawa, Y., Döhl, L. N., Woolsey, N. & Morace, A. Enhancement of collisionless shock ion acceleration by electrostatic ion two-stream instability in the upstream plasma. *Physical Review Accelerators and Beams* **22,** 043401 (2019).

153. Forslund, D. & Freidberg, J. Theory of laminar collisionless shocks. *Physical Review Letters* **27,** 1189 (1971).

154. Gary, S. P. *Theory of space plasma microinstabilities* (Cambridge university press, 2005).

155. Wu, C. Physical mechanisms for turbulent dissipation in collisionless shock waves. *Space Science Reviews* **32,** 83–97 (1982).

156. Wu, C. *et al.* Microinstabilities associated with a high Mach number, perpendicular bow shock. *Space Science Reviews* **37,** 63–109 (1984).

157. Marcowith, A. *et al.* The microphysics of collisionless shock waves. *Reports on Progress in Physics* **79,** 046901 (2016).

158. Stringer, T. Electrostatic instabilities in current-carrying and counter-streaming plasmas. *Journal of Nuclear Energy. Part C, Plasma Physics, Accelerators, Thermonuclear Research* **6,** 267 (1964).

159. Imre, K. & Özizmir, E. Comments on "Stability limits for longitudinal waves in ion beam-plasma interactions". *The Physics of Fluids* **17,** 1046–1047 (1974).

160. Fried, B. D. & Gould, R. W. Longitudinal ion oscillations in a hot plasma. *The Physics of Fluids* **4,** 139–147 (1961).

161. Fried, B. D. & Wong, A. Y. Stability limits for longitudinal waves in ion beam-plasma interaction. *The Physics of Fluids* **9,** 1084–1089 (1966).

162. Forslund, D. & Shonk, C. Numerical simulation of electrostatic counterstreaming instabilities in ion beams. *Physical Review Letters* **25,** 281 (1970).

163. Gresillon, D, Doveil, F & Buzzi, J. Space correlation in ion-beam—plasma turbulence. *Physical Review Letters* **34,** 197 (1975).

164. Ohnuma, T., Fujita, T. & Adachi, S. Observation of an Obliquely Growing Mode in an Ion-Beam—Plasma System. *Physical Review Letters* **36,** 471 (1976).

165. Fujita, T., Ohnuma, T. & Adachi, S. Self-oscillations excited by two stream ion-ion instability. *Plasma Physics* **19,** 875 (1977).

166. Gary, S. P. & Omidi, N. The ion-ion acoustic instability. *Journal of Plasma Physics* **37,** 45–61 (1987).

167. Gurnett, D. A., Neubauer, F. & Schwenn, R. Plasma wave turbulence associated with an interplanetary shock. *Journal of Geophysical Research: Space Physics* **84,** 541–552 (1979).

168. Kennel, C., Scarf, F., Coroniti, F., Smith, E. & Gurnett, D. Nonlocal plasma turbulence associated with interplanetary shocks. *Journal of Geophysical Research: Space Physics* **87,** 17–34 (1982).

169. Scarf, F. *et al.* ISEE-3 wave measurements in the distant geomagnetic tail and boundary layer. *Geophysical Research Letters* **11,** 335–338 (1984).

170. Gurnett, D., Marsch, E, Pilipp, W, Schwenn, R & Rosenbauer, H. Ion acoustic waves and related plasma observations in the solar wind. *Journal of Geophysical Research: Space Physics* **84,** 2029–2038 (1979).

171. Gallagher, D. L. Short-wavelength electrostatic waves in the Earth's magnetosheath. *Journal of Geophysical Research: Space Physics* **90,** 1435–1448 (1985).

172. Treumann, R. A. & Terasawa, T. Electron acceleration in the heliosphere. *Space Science Reviews* **99,** 135–150 (2001).

173. Galeev, A. Acceleration of electrons to ultrarelativistic energies by shock waves and synchrotron radiation of these electrons. *Sov. Phys. JETP* **59,** 965–971 (1984).

174. Karimabadi, H, Omidi, N & Quest, K. Two-dimensional simulations of the ion/ion acoustic instability and electrostatic shocks. *Geophysical Research Letters* **18,** 1813–1816 (1991).

175. Kato, T. N. & Takabe, H. Electrostatic and electromagnetic instabilities associated with electrostatic shocks: Two-dimensional particle-in-cell simulation. *Physics of Plasmas* **17,** 032114 (2010).

176. Ohira, Y. & Takahara, F. Oblique ion two-stream instability in the foot region of a collisionless shock. *The Astrophysical Journal* **688,** 320 (2008).

177. Sarraf, S. P., Williams, E. A. & Goldman, L. M. Ion-ion two-stream instability in multispecies laser-produced plasma. *Physical Review A* **27,** 2110 (1983).

178. Ross, J. *et al.* Collisionless coupling of ion and electron temperatures in counterstreaming plasma flows. *Physical Review Letters* **110,** 145005 (2013).

179. Rinderknecht, H. G. *et al.* Highly Resolved Measurements of a Developing Strong Collisional Plasma Shock. *Physical Review Letters* **120,** 095001 (2018).

180. Zhang, W.-s., Cai, H.-b. & Zhu, S.-p. The formation and dissipation of electrostatic shock waves: the role of ion–ion acoustic instabilities. *Plasma Physics and Controlled Fusion* **60,** 055001 (2018).

181. King, M, Gray, R., Powell, H., Capdessus, R & McKenna, P. Energy exchange via multi-species streaming in laser-driven ion acceleration. *Plasma Physics and Controlled Fusion* **59,** 014003 (2016).

182. Dum, C., Marsch, E & Pilipp, W. Determination of wave growth from measured distribution functions and transport theory. *Journal of Plasma Physics* **23,** 91–113 (1980).

183. Lemons, D. S. & Gary, S. P. Current-driven instabilities in a laminar perpendicular shock. *Journal of Geophysical Research: Space Physics* **83,** 1625–1632 (1978).

184. Moses, S., Coroniti, F., Kennel, C. & Scarf, F. Estimation and comparison of quasilinear electron heating in the shock foot at Jupiter and Earth. *Geophysical Research Letters* **12,** 609–612 (1985).

185. Grassi, A., Fedeli, L., Sgattoni, A. & Macchi, A. Vlasov simulation of laser-driven shock acceleration and ion turbulence. *Plasma Physics and Controlled Fusion* **58,** 034021 (2016).

186. Hegelich, M *et al.* MeV ion jets from short-pulse-laser interaction with thin foils. *Physical Review Letters* **89,** 085002 (2002).

187. Ota, M *et al.* Collisionless Electrostatic Shock Acceleration of Proton using High Intensity Laser. *High Energy Density Physics* **33,** 100697 (2019).

188. Nikezic, D & Yu, K. Formation and growth of tracks in nuclear track materials. *Materials Science and Engineering: R: Reports* **46,** 51–123 (2004).

189. Takabe, H. A historical perspective of developments in hydrodynamic instabilities, integrated codes and laboratory astrophysics. *Nuclear Fusion* **44,** S149 (2004).